Astronomy Letters, Vol. 27, No. 3, 2001, pp. 135–139. From Pis'ma v Astronomicheskiĭ Zhurnal, Vol. 27, No. 3, 2001, pp. 163–169.

A Scaling Relation between the SZ Decrement and the Thomson Depth in Clusters of Galaxies[1]

C. K. Cramphorn*

Max-Planck-Institut für Astrophysik, Karl-Schwarzschild-Str. 1, 85740 Garching bei Munchen, Germany

Received June 29, 2000

Abstract—In a recent study of dark matter *N*-body simulations, a scaling relation between the SZ decrement and the Thomson depth of a cluster of galaxies of the form $\Delta T_r \propto \tau_T^2$ has been found (Diaferio *et al.* 2000). In this paper, it will be shown that such a scaling relation arises if the intracluster gas is distributed similar to the dark matter density described by the NFW-profile and the finite spatial resolution of the numerical simulation is taken into account. It is furthermore investigated whether the $\Delta T_r \propto \tau_T^2$ relation holds for analytical models of an isothermal gas sphere in the gravitational potential of a dark matter halo distributed according to the NFW-profile, the available experimental data of SZE observations, and recent results from cosmological gas-dynamical simulations of clusters of galaxies. Combining such a relation with temperature estimates from X-ray observations would provide information about a dependence of T_e on τ_T. The Thomson depth might therefore emerge as another important scaling parameter in studies of clusters of galaxies. © *2001 MAIK "Nauka/Interperiodica".*

Key words: *clusters of galaxies, dark matter simulations*

1. SCALING RELATIONS FOR CLUSTERS OF GALAXIES

Through an interplay of X-ray observations and theoretical modeling, several scaling relations, which suggest the self-similarity of relaxed clusters of galaxies, have been discovered. Especially interesting is the tight relation between the virial mass of a cluster and the temperature of the intracluster medium (ICM), $M_{vir} \propto T_e^{3/2}$ (see, e.g., Evrard *et al.* 1996; Horner *et al.* 1999).

With the recent progress in observing the SZ decrement in about a dozen clusters of galaxies (Birkinshaw 1999; Carlstrom 1999), we obtain another observable parameter to constrain the physics of these objects. The strength of the SZ effect (SZE) is a measure for a different physical parameter than the X-ray surface brightness or the inferred X-ray luminosity. It primarily depends upon the Thomson depth and not on the virial mass, although they are certainly connected in some way.

By analogy with well-known scaling relations, it would be reasonable to expect a power law dependence between the SZ decrement and the Thomson depth of a cluster of the form $\Delta T_r \propto \tau_T^\alpha$. Combining this relation with temperature estimates of the ICM through X-ray observations provides direct information about the Thomson depth and about the dependence of T_e on τ_T. Therefore, the Thomson depth of a cluster might become an important scaling parameter for tests of the models of clusters of galaxies.

2. THE SZ DECREMENT

The scattering of Cosmic Microwave Background (CMB) photons by the thermal electrons of the ICM leads to a unique distortion of the CMB spectrum [Sunyaev and Zel'dovich 1972, 1980; see Rephaeli (1995) for a recent review].

In the Rayleigh–Jeans (RJ) limit, the thermal effect causes a temperature diminution given by

$$\frac{\Delta T_r}{T_r} = -2\int n_e \sigma_T \frac{kT_e}{m_e c^2} dl. \quad (1)$$

In an attempt to study the imprint of large-scale motions in superclusters on the CMB, Diaferio *et al.* (2000) have analyzed high-resolution *N*-body simulations of a representative volume of a Cold Dark Matter universe. Since the SZE depends upon the properties of the ICM, they made the following assumptions about the relation of dark matter to gas:

(i) The electron number density is simply proportional to the dark matter mass density $n_e = (\rho_{dm}/m_p)\Omega_b/\Omega_0$, where m_p is the proton mass, Ω_b is the baryonic density, and Ω_0 is the gravitating matter density in units of the critical density.

[1] This article was submitted by the author in English.

* E-mail address for contacts: conrad@mpa-garching.mpg.de

1063-7737/01/2703-0135$21.00 © 2001 MAIK "Nauka/Interperiodica"

(ii) At any point within the cluster, the plasma is thermalized, i.e., $kT_e = \sigma_{dm}^{\parallel 2} m_p/2$, where $\sigma_{dm}^{\parallel}$ is the projected velocity dispersion of the dark matter particles.

Note that, since $\beta = (\mu m_p \sigma^{\parallel 2}/kT_e)$, the second assumption implies $\beta = 1.2$ for an abundance with $\mu = 0.6$, as inferred for clusters of galaxies, if the projected velocity dispersions of dark matter particles and galaxies are equivalent. DSN computed the Thomson depth along a given line of sight through the simulated volume as

$$\tau_T = \sigma_T \int n_e dl = \sigma_T \frac{\Omega_b}{\Omega_0} \int_0^L \frac{\rho_{dm}(l)}{m_p} dl, \qquad (2)$$

where L is the linear dimension of the computational box. With their assumptions, the thermal SZE in the Rayleigh–Jeans limit can be expressed as

$$\frac{\Delta T_r}{T_r} = -2\sigma_T \frac{m_p}{m_e} \frac{\Omega_b}{\Omega_0} \int_0^L \frac{\sigma_{dm}^{\parallel 2}(l)}{2c^2} \frac{\rho_{dm}(l)}{m_p} dl. \qquad (3)$$

These two quantities were computed for a large number of clusters and it was found that the strength of the SZE scales quadratically with the Thomson depth:

$$\Delta T_r \approx -\tau_T^2 \times 2 \times 10^6 \ \mu\text{K}. \qquad (4)$$

3. SCALING RELATION FOR GAS DISTRIBUTED SIMILARLY TO DARK MATTER

In order to compute the Thomson depth as it was done by DSN it is assumed that the dark matter density profile of a cluster of galaxies is of the form proposed by Navarro *et al.* (1995) (NFW)

$$\rho_{dm}(x) = \frac{\rho_s}{x(1+x)^2}. \qquad (5)$$

Here, ρ_s is the product of the nondimensional overdensity δ_c and the critical density $\rho_{crit} = 1.88 \times 10^{-29} h^2$ g cm^{-3} ($h = H_0/100$ km s^{-1} Mpc^{-1}, and $x = r/r_s$ is the radius measured in units of the scaling radius. The NFW profile is self-similar, meaning that for dark matter halos of different virial mass the shape remains the same and just scales with the overdensity and the scaling radius. These two quantities are not independent. For a given set of cosmological parameters they can be computed as a function, e.g., of the virial mass of a cluster (Navarro *et al.* 1997). Therefore, Eq. (5) represents a one-parameter family of profiles. To compute the Thomson depth for the NFW profile one has to solve the following integral:

$$\tau_T(z) = \sigma_T r_s \frac{\Omega_b}{\Omega_0} \frac{\rho_s}{m_p} \int \frac{dl}{x(1+x)^2}, \qquad (6)$$

where the projected radius z and the coordinate along the line of sight l, both measured in units of the scaling radius, were introduced. They are related to the radial distance x by $x^2 = z^2 + l^2$. The Thomson depth as computed in Eq. (6) is just proportional to the surface mass density $\tau_T = \sigma_T(\Omega_b/\Omega_0)(\Sigma_{dm}/m_p)$. Since this is an important quantity for studying the effects of gravitational lensing due to a cluster of galaxies, it has been computed in this context for the NFW profile by Bartelmann (1996)

$$\tau_T(z) = \sigma_T r_s \frac{\Omega_b}{\Omega_0} \frac{\rho_s}{m_p} \frac{2 f(z)}{z^2 - 1} \qquad (7)$$

with

$$f(z) = \begin{cases} 1 - \dfrac{2}{\sqrt{z^2-1}} \arctan\left(\sqrt{\dfrac{z-1}{z+1}}\right), & z > 1 \\ 0, & z = 1 \\ 1 - \dfrac{2}{\sqrt{1-z^2}} \arctan\left(\sqrt{\dfrac{1-z}{1+z}}\right), & z < 1. \end{cases}$$

Since $f(z)$ involves only nondimensional quantities, Eq. (7) implies that for a given cluster with a certain virial mass and therefore given overdensity and scaling radius, the Thomson depth scales as $\rho_s r_s$: $\tau_T \propto \rho_s r_s$.The temperature profile of the ICM used by DSN can be written as

$$kT_e(r) = \frac{m_p \sigma_{dm}^{\parallel}(r)^2}{2} = \frac{1}{2} \frac{m_p G M_{dm}(<r)}{r}. \qquad (8)$$

The NFW density profile implies a mass profile given by

$$M_{dm}(<x) = 4\pi \rho_s r_s^3 \left[\ln(1+x) - \frac{x}{1+x} \right]. \qquad (9)$$

Therefore, Eq. (3) reads as

$$\frac{\Delta T_r}{T_r} = c_1 \rho_s^2 r_s^3 \int \frac{\ln(1+x) - x/(1+x)}{x^2(1+x)^2} \mathrm{d}l \qquad (10)$$

with the constant

$$c_1 = -\frac{4\pi}{3} \frac{\sigma_T G m_p (\Omega_b/\Omega_0)}{m_e c^2}.$$

This integral (Eq. (10)) cannot be solved analytically for $z > 0$, and does not depend upon the virial mass of a cluster. This implies that the SZ decrement should obey the scaling $\Delta T_r \propto \rho_s^2 r_s^3$. With these scalings we find that the ratio $\Delta T_r/\tau_T^2$ should not be constant but rather scale with mass as r_s.

So far the effects of the finite spatial resolution, which is inherent to numerical simulations, upon the relation found by DSN have been neglected. For example the spatial resolution of the OCDM model they found their relation for is $\delta r = 30 h^{-1}$ kpc. This is modeled analytically by folding the computed Thomson

depth and SZ decrement with Gaussian windows of relative beamsize $a = \delta r/r_s$. This method gives results consistent with a central integration ($z = 0$) with a lower integration limit $l_{\min} \sim a$. The beam-averaged Thomson depth and microwave decrement therefore read as

$$\hat{\tau}_{\mathrm{T}}(a) = \int_0^\infty \frac{e^{-z^2/2a^2}}{a^2}\tau_{\mathrm{T}}(z)z\,dz \tag{11}$$

and

$$\Delta\hat{T}_r(a) = \int_0^\infty \frac{e^{-z^2/2a^2}}{a^2}\Delta T_r(z)z\,dz. \tag{12}$$

The important thing to note is that since δr is constant, the relative beamsize a decreases with increasing scaling radius. For a more massive cluster, the relative beamsize is therefore smaller and only the more central parts of the cluster are probed in the averaging. This is essentially the origin of the relation found by DSN.

Working this out quantitatively yields an expression for the normalization found by DSN and its dependence on the parameters of the model

$$\frac{\Delta\hat{T}_r}{\hat{\tau}_{\mathrm{T}}^2} = \frac{4\pi}{3}\frac{Gm_p^2T}{\sigma_{\mathrm{T}}m_ec^2}\frac{\delta r}{(\Omega_{\mathrm{b}}/\Omega_0)}g(a) \approx 2\times10^6\ \mu\mathrm{K},$$

where we use $T_r = 2.725$ K, the CMB temperature (Mather *et al.* 1999), $\Omega_{\mathrm{b}} = 0.0125h^{-2}$ (Smith *et al.* 1993), and $\Omega_0 = 0.3$. The dependence on a is collected in the function $g(a)$. As mentioned previously, since a depends upon the scaling radius and therewith upon the virial mass of a cluster, we can compute the ratio $\Delta\hat{T}_r/\hat{\tau}_{\mathrm{T}}^2$ as a function of virial mass instead of a. The variation of $g(a)$ over the mass range 1×10^{13} to $3\times10^{15}\,M_\odot$ is less than 10%. This explains why DSN found the relation between the SZ decrement and the Thomson depth in their studies.

4. ISOTHERMAL GAS IN A NFW DARK MATTER POTENTIAL

It is an observational fact that the central parts of relaxed, non cooling flow clusters are close to isothermal. Their surface brightness profile is well fitted by the so-called β profile (Cavaliere and Fusco-Femiano 1978), which implies an electron density profile

$$n_e(r) = \frac{n_e^0}{(1+(r/r_c)^2)^{3\beta/2}}. \tag{13}$$

The relationship of the parameters of the β profile (n_e^0, r_c, and β) to the parameters characterizing the NFW profile (ρ_s and r_s) is not easy to interpret. Integrating the force balance in hydrostatic equilibrium for the gravitational potential given by the mass distribution (Eq. (9)) of a NFW-profile

$$\frac{dp_{\mathrm{g}}}{dr} = -\frac{GM_{dm}(<r)}{r^2}\rho_{\mathrm{g}} \tag{14}$$

with ρ_{g} the gas pressure, under the assumption of isothermality leads to the following gas density distribution (Makino *et al.* 1998):

$$\rho_{\mathrm{g}}(x) = \rho_{\mathrm{g}}^0 e^{-b}(1+x)^{b/x}, \tag{15}$$

where b is given by

$$b = \frac{4\pi Gm_p\rho_s r_s^2}{kT_e}. \tag{16}$$

It is assumed that the gas is at a temperature given by the virial theorem. To fix the constant of integration the following normalization of the gas density is used. The ratio of the gas mass to the dark matter mass inside the virial radius is given by the universal baryon fraction

$$\frac{M_{\mathrm{gas}}(<r_{\mathrm{vir}})}{M_{dm}(<r_{\mathrm{vir}})} = \frac{\Omega_{\mathrm{b}}}{\Omega_0}. \tag{17}$$

Using this relation for the normalization leads to

$$\rho_{\mathrm{g}}^0 = \rho_s\frac{\Omega_{\mathrm{b}}}{\Omega_0}\left[\ln(1+c) - \frac{c}{1+c}\right] \times\left[e^{-b}\int_0^c x^2(1+x)^{b/x}dx\right]^{-1} \tag{18}$$

with $c = r_{\mathrm{vir}}/r_s$ is the concentration parameter. The Thomson depth and SZ decrement resulting from this density profile must be computed numerically. Note that the gas density profile (Eq. (13)) is very sensitive to the parameter b, which depends upon the gas temperature. Although the derived gas density distribution can be well fitted to a β-profile, the core radii one obtains are up to one order of magnitude smaller than the observed ones, suggesting that additional physical processes have to be included (Makino *et al.* 1998).

5. CLUSTERS WITH OBSERVED SZ DECREMENTS

Recent progress in observational techniques has allowed a significant detection of the SZ decrement in about a dozen clusters of galaxies. More clusters have been observed, but not all data have been published yet. The published data has been compiled by Cooray (1999), who scaled the observations made with different instruments and, therefore, at different frequencies to the RJ part of the spectrum and applied relativistic corrections where appropriate. The cluster temperatures, as derived from broad-band single-phase plasma, fits to ASCA data by White (2000) were used. To this

Thomson depths, electron temperatures, and SZ decrements for observed clusters

Clusters	τ_T, 10^{-3}	T_e, keV	ΔT_r, mK
A0478	13.13 ± 2.66	06.58 ± 0.26	−0.92 ± 0.15
A0665	11.06 ± 1.64	07.73 ± 0.38	−0.91 ± 0.09
A0773	09.69 ± 1.85	08.63 ± 0.68	−0.89 ± 0.10
A1413	12.32 ± 1.83	07.32 ± 0.25	−0.96 ± 0.11
A1656	05.96 ± 1.20	08.67 ± 0.17	−0.55 ± 0.10
A1689	19.44 ± 3.64	09.23 ± 0.28	−1.91 ± 0.30
A1835	15.41 ± 2.67	08.17 ± 0.50	−1.34 ± 0.15
A2142	09.37 ± 1.79	09.02 ± 0.32	−0.90 ± 0.14
A2163	13.64 ± 2.64	13.29 ± 0.64	−1.93 ± 0.28
A2204	12.51 ± 4.08	07.21 ± 0.25	−0.96 ± 0.28
A2218	12.36 ± 1.99	06.84 ± 0.34	−0.90 ± 0.10
A2256	05.94 ± 1.31	06.96 ± 0.11	−0.44 ± 0.09
Zw3146	13.72 ± 2.84	05.89 ± 0.26	−0.86 ± 0.14
CL0016 + 16	13.95 ± 3.56	08.15 ± 0.80	−1.21 ± 0.19
MS 0451.6–0305	12.91 ± 0.98	10.40 ± 0.90	−1.43 ± 0.10
RX J0658–5557	07.84 ± 4.22	17.00 ± 5.00	−1.42 ± 0.43

sample, two high redshift clusters ($z \approx 0.5$) were added, for which recent observations of the SZE have been reported: MS 0451.6–0305 (Reese *et al.* 2000) and RX J0658–5557 (Andreani *et al.* 1999). The Thomson depth for these clusters were computed with Eq. (1) under the assumption of isothermality (see the table).

6. SZ DECREMENT AND THOMSON DEPTH FOR SIMULATED CLUSTERS

In recent years, numerical simulations of clusters of galaxies that treat the dark matter and the gas component consistently have been performed by several groups. It was possible to obtain the data necessary for the purposes of this paper from two sources: the Santa Barbara Cluster Project (Frenk *et al.* 1999) and the Simulated Cluster Archive (Norman *et al.* 2000). The Santa Barbara Cluster Project compiled and compared simulations of a cluster with a virial mass of $1.1 \times 10^{15} M_\odot$ by several groups with different codes and found general consistency of the results. The cosmological parameters used in their simulations were $h = 0.5$, $\Omega = 1$, $\Omega_b = 0.1$ and $\sigma_8 = 0.9$. We used their research of the gas density and temperature profile to compute the Thomson depth and the SZ decrement.

The Simulated Cluster Archive is a project to make data for several simulated clusters of galaxies publicly available on the Internet. The following cosmological parameters for a ΛCDM model were used in those simulations: $h = 0.7$, $\Omega_0 = 0.3$, $\Omega_b = 0.026$, and $\sigma_8 = 0.928$. The Thomson depth and the SZ decrement were computed for 16 clusters having virial masses in the range of 5×10^{14}–$2 \times 10^{15} M_\odot$.

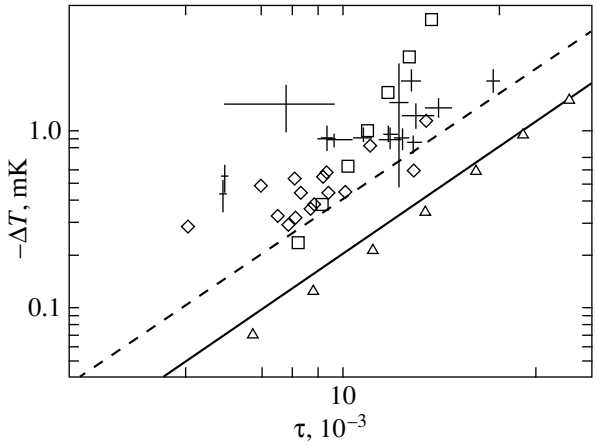

SZ decrement versus Thomson depth. These two quantities were computed for a sequence of virial masses in the range 1×10^{14} to $3 \times 10^{15} M_\odot$ for samples of dark matter (triangles) and gas (squares). The positions of modeled and observed clusters are marked by diamonds and crosses, respectively. The solid line indicates the relation of DSN: $\Delta T = -\tau_T^2 \times 2 \times 10^6$ μK. The dashed line indicates the same relation for $\beta = 0.6$.

7. RESULTS

In this section, the results from the previous sections are presented and discussed. The SZ decrement of each cluster from the four samples is plotted against its Thomson depth in the figure. The solid line is the relation found by DSN: $\Delta T_r \approx -\tau_T^2 \times 2 \times 10^6$ μK. The triangles, which trace this relation are seven models of a cluster with a virial mass in the range from 1×10^{14} to $3 \times 10^{15} M_\odot$. Given the virial mass of the dark matter halo, the scaling radius and the overdensity were computed according to the algorithm provided in Navarro *et al.* (1997). With these parameters, the Thomson depth and the microwave decrement were derived as described in Section 3.

The same method was used for the second sample covering the same virial mass range. The Thomson depth was computed with the gas density distribution given by Eq. (15). Because this model assumes isothermality, the SZ decrement is simply proportional to the Thomson depth. The temperature and its scaling with virial mass were chosen in such a way, that the parameter b remained constant over the given mass range, corresponding to a fixed $\beta = 2/3$. The positions of these clusters in the $\Delta T_r - \tau_T$ plane are marked by squares. It is obvious that, for this sample, the slope of the relation is much steeper. It is close to $\Delta T_r \propto \tau_T^4$, which would imply the dependence $T_e \propto \tau_T^3$. The significance of this steep dependence is nevertheless doubtful because, as mentioned in one of the previous sections, there are some inconsistencies related with this gas density distribution. The actual slope of the relation is very sensitive to the scaling of the parameter b with virial mass. Changing the absolute value for b or, equivalently, β

does not change the slope of the relation but mainly shifts the data points to higher Thomson depths.

The positions of the observed clusters are plotted together with their error bars. This sample is obviously strongly biased: the hottest, most massive clusters were chosen to be observed in order to make the detection of the SZE more probable. Future observations with higher sensitivity will detect lower mass clusters and therefore show how the relation extends down to smaller Thomson depths.

Finally, the derived Thomson depth and SZ decrement for the simulated clusters are plotted with diamonds. It is obvious that the slope for the observed and simulated clusters is more shallow than a dependence $\Delta T_r \propto \tau_T^2$. A best fit to the combined data set gives a slope of about 3/2. A different slope is not surprising since gas and dark matter are distributed differently in clusters of galaxies. The simulated and observed clusters lie all above the relation found by DSN. If one assumes a value of 0.6 for β instead of 1.2, the normalization of the relation being proportional to β^{-1} simply doubles (dashed line in the figure). There is still a discrepancy of about a factor of 2, which might indicate the influence of some neglected physical processes, e.g., nongravitational heating.

8. SUMMARY AND DISCUSSION

In this paper, we offered an explanation of the relation between the Thomson depth and the CMB decrement caused by the SZE found in studies of dark matter *N*-body simulations of clusters of galaxies. This relation was derived by assuming that the density profiles of dark matter halos in *N*-body simulations can be described by the NFW-profile and by modeling the finite spatial resolution of numerical simulations.

An attempt has furthermore been made to investigate if there are hints for the existence and slope of such a relation from other samples of clusters of galaxies. Constructing clusters with a more realistic description of the gas density distribution resulted in a steeper slope of the relation. Based on the data for the observed and simulated clusters, we cannot confirm a relation although a certain trend is discernible, having a much shallower slope. Future observations and numerical simulations should allow to test, whether such a relation still holds at and how it extends down to smaller Thomson depths. Although this relation awaits a firm establishment, it is important to mention possible applications. As mentioned earlier a relation between the SZ decrement and the Thomson depth would imply, if clusters are close to isothermal, a relation between T_e and τ_T or, equivalently, between ΔT_r and T_e. A relation like this would enable one to estimate the temperature of the cluster from the observed SZ decrement. Combining this relation with the mass temperature relation, one could derive a $M_{vir} - \tau_T$ or, equivalently, $M_{vir} - \Delta T_r$ relation for clusters of galaxies, which is rather important since the virial mass is an important but difficult quantity to determine. This might become especially important for high redshift clusters, which are too faint in X-rays.

ACKNOWLEDGMENTS

We used data available from the Simulated Cluster Archive (http://sca.ncsa.uiuc.edu/).

REFERENCES

1. P. Andreani, H. Boehringer, G. Dall'Oglio, *et al.*, Astrophys. J. **513**, 23 (1999).
2. M. Bartelmann, Astron. Astrophys. **313**, 697 (1996).
3. M. Birkinshaw, Phys. Rep. **310**, 97 (1999).
4. J. E. Carlstrom, M. K. Joy, L. Grego, *et al.*, astro-ph/9905255 (1999).
5. A. Cavaliere and R. Fusco-Femiano, Astron. Astrophys. **70**, 677 (1978).
6. A. R. Cooray, Mon. Not. R. Astron. Soc. **307**, 841 (1999).
7. A. Diaferio, R. A. Sunyaev, and A. Nusser, Astrophys. J. Lett. **533**, L71 (2000).
8. A. E. Evrard, A. C. Metzler, and J. F. Navarro, Astrophys. J. **469**, 494 (1996).
9. C. S. Frenk, S. D. M. White, P. Bode, *et al.*, Astrophys. J. **525**, 554 (1999).
10. D. J. Horner, R. F. Mushotzky, and C. A. Scharf, Astrophys. J. **520**, 78 (1999).
11. N. Makino, S. Sasaki, and Y. Suto, Astrophys. J. **497**, 555 (1998).
12. J. C. Mather, D. J. Fixsen, R. A. Shafer, *et al.*, Astrophys. J. **512**, 511 (1999).
13. J. F. Navarro, C. S. Frenk, and S. D. M. White, Astrophys. J. **490**, 493 (1997).
14. J. F. Navarro, C. S. Frenk, and S. D. M. White, Mon. Not. R. Astron. Soc. **275**, 720 (1995).
15. M. L. Norman, G. Daues, and E. Nelson, astro-ph/0005183 (2000).
16. E. D. Reese, J. J. Mohr, J. E. Carlstrom, *et al.*, Astrophys. J. **533**, 38 (2000).
17. Y. Rephaeli, Annu. Rev. Astron. Astrophys. **33**, 541 (1995).
18. M. S. Smith, L. H. Kawano, and R. A. Malaney, Astrophys. J., Suppl. Ser. **85**, 219 (1993).
19. R. A. Sunyaev and Ya. Zel'dovich, Annu. Rev. Astron. Astrophys. **18**, 537 (1980).
20. R. A. Sunyaev and Ya. Zel'dovich, Comments Astrophys. Space Phys. **4**, 173 (1972).
21. D. A. White, Mon. Not. R. Astron. Soc. **312**, 663 (2000).

Astronomy Letters, Vol. 27, No. 3, 2001, pp. 140–149. Translated from Pis'ma v Astronomicheskiĭ Zhurnal, Vol. 27, No. 3, 2001, pp. 170–179.

The Ursa Major Supercluster of Galaxies: I. The Luminosity Function

A. I. Kopylov* and F. G. Kopylova

Special Astrophysical Observatory, Russian Academy of Sciences, Niznič Arkhyz, Karachaevo-Cherkessia, 357147 Russia

Received April 7, 2000

Abstract—Catalogs of bright galaxies in the central regions of 11 clusters in the Ursa Major supercluster are presented. Absolute and relative coordinates and total *B* and *R* magnitudes are given for each galaxy. Plates taken with the 2-m Tautenburg Observatory telescope and CCD images obtained with the 6-m and 1-m SAO telescopes are used. The luminosity functions (LFs) for galaxies in the cluster nuclei (3 Mpc × 3 Mpc) and the composite LF for the supercluster are constructed. The composite LF is well fitted by a Schechter function with $M_B^* = -20\overset{m}{.}91$, $\alpha = -1.02$ and with $M_R^* = -22\overset{m}{.}39$, $\alpha = -1.06$. A comparison with the LFs of field galaxies and of various samples of clusters and superclusters shows that the Ursa Major supercluster have LF parameters characteristic of the field and, thus, differ from those of the Corona Borealis supercluster, which is apparently at a later stage of dynamical evolution. © *2001 MAIK "Nauka/Interperiodica".*

Key words: *galaxies, groups and clusters of galaxies*

INTRODUCTION

Superclusters of galaxies are systems or elements of the large-scale structure of maximum size and mass with a dynamical evolution time comparable to the age of the Universe. Photometric, morphological, and dynamical studies of these systems can be used to analyze the effects of factors acting on the largest spatial and time scales of the formation and evolution of galaxies. Depending on how a system is formed, from large to small scales or vice versa, the formation and evolution of galaxies in superclusters can be more or less coherent in nature. In particular, information about these processes is contained in such an important (integrated) characteristic of the galaxy system as the luminosity function of its constituent galaxies. The dependence of the luminosity function on the morphological type, position within the system, and ambient density of the galaxies under study is also of interest in a more detailed analysis.

Ursa Major is one of the nearest ($z \simeq 0.06$) compact superclusters. We found its nucleus to consist of six Abell (1958) clusters (A1270, A1291, A1318, A1377, A1383, and A1436) and five more clusters of lower but comparable populations; four of them (Anon1, Anon2, Anon3, and Anon4) were revealed by Bayer (1980) and one (Sh166) by Shectman (1985). We established that these five clusters belong to the supercluster by measuring the radial velocities for several brightest galaxies in each of them. Apart from the above six Abell clusters, A1452 and A1507, the two most isolated peripheral members of the system, were assigned to the Ursa Major supercluster in the catalog of superclusters (Einasto *et al.* 1997).

At present, only photographic measurements of galaxies in A1377 (Bucknell *et al.* 1979; Flin *et al.* 1995), as well as CCD measurements for several galaxies in A1291 (Merrifield and Kent 1989) and for one or two galaxies in other clusters, have been published. Here, our main goals are to compile and analyze photometric catalogs of clusters, to construct their luminosity functions, and select a sample of early-type (E, S0) galaxies to be subsequently used to determine the relative distances of clusters (Kopylova and Kopylov 2001).

OBSERVATIONS AND DATA REDUCTION

We determined the redshifts of galaxies and clusters from the spectra taken in 1991–1993 with a 1024-channel photon counter—the scanner (IPSC) mounted at the Nasmyth-1 focus of the 6-m telescope on the SP-124 spectrograph (Drabek *et al.* 1986; Afanas'ev *et al.* 1986). We performed our observations by using the B1 grating (600 lines mm^{-1}) in the spectral range 3600 to 5500 Å with a dispersion of 1.9 Å per channel. We also used the radial-velocity data for the A1318 and Anon4 clusters from Zabludoff *et al.* (1993) and for A1291 from Merrifield and Kent (1991). Table 1 contains the following data: (1) ACO cluster numbers (Abell *et al.* 1989); (2) equatorial coordinates [the first row gives coordinates of the cluster center for epoch B1950.0 from the ACO catalog (A1270, A1291, A1318, A1377, A1383, and A1436), from Bayer (1980) (Anon1,

* E-mail address for contacts: akop@sao.ru

Table 1. Data on clusters and coordinates of the centers of the regions studied

Cluster	α	β	N_A	$\langle V_0 \rangle$	σ_v	N_v
A1377	$11^h44^m18^s$	+56°01′00″	59	15210	570	18
	$11^h44^m54^s$	+56°01′28″				
Sh166	$12^h00^m54^s$	+55°11′00″	39	15360	230	4
	$12^h00^m41^s$	+55°02′30″				
A1291	$11^h29^m18^s$	+56°18′00″	61	15720	700	21
	$11^h29^m19^s$	+56°18′06″				
A1318	$11^h33^m42^s$	+55°14′00″	56	17140	270	13
	$11^h33^m29^s$	+55°15′32″				
A1383	$11^h45^m30^s$	+54°54′00″	54	18080	530	12
	$11^h45^m39^s$	+54°54′01″				
Anon4	$11^h35^m12^s$	+56°01′00″	38	18400	520	7
	$11^h36^m32^s$	+55°52′14″				
A1436	$11^h57^m54^s$	+56°32′00″	69	19250	380	11
	$11^h57^m43^s$	+56°30′32″				
Anon3	$11^h26^m18^s$	+55°44′00″	40	20480	350	3
	$11^h27^m41^s$	+55°41′38″				
A1270	$11^h26^m42^s$	+54°20′00″	40	20660	420	10
	$11^h26^m57^s$	+54°25′57″				
Anon1	$11^h13^m12^s$	+54°46′00″	52	20970	570	8
	$11^h12^m48^s$	+54°44′55″				
Anon2	$11^h16^m48^s$	+54°43′00″	30	21100	240	7
	$11^h16^m44^s$	+54°43′34″				

Anon2, Anon3, and Anon4), and from Sheckman (1985) (Sh166), and the second row gives coordinates of the center of the region we studied]; (3) the measure of cluster richness, which is equal to the number of bright galaxies in the cluster according to ACO and (for additional clusters) estimates of this parameter calculated from the number of galaxies brighter than $M_B = -19^m$ in the central (3 Mpc × 3 Mpc) cluster region with calibration based on six Abell clusters of the supercluster; (4) cluster mean radial velocities reduced to the Local Group centroid; (5) radial-velocity dispersions; and (6) the number of measured radial velocities.

Photographic observations were performed with the Schmidt telescope at the Tautenburg Observatory (Germany) on February 7–8 and March 6–7, 1989, in the *B* (ZU21 + GG13) and *R* (Kodak 103aE + RG1) bands (emulsion and filter are given in parentheses). Plates were taken with 30- and 90-min exposures in the *B* and *R* bands, respectively, for 2″–3.″5 seeing. To cover the entire supercluster by 3.°25 × 3.°25 plates with a 51.″4 mm^{-1} scale, we had to photograph three areas centered at 11^h22^m, 55°31′, $11^h36^m.5$, 55°30′, and 11^h52^m, 55°25′ (B1950). We took two plates in *B* and one plate in *R* for each of the three areas. In this case, adjacent areas are overlapped approximately by a third, which allowed us to obtain twice as many independent measurements for five clusters in the overlapping areas (A1270, A1291, A1377, A1383, and Anon3) as those for the remaining six clusters. We determined the object coordinates with an accuracy of 1.5–2″ by using the Ascorecord coordinate-measuring instrument.

Plates were scanned with the AMD-2 automatic microdensitometer at the Special Astrophysical Observatory with a 20-μm step and a 25 μm × 25 μm slit. Photographic densities were converted to relative intensities by using a wedge imprinted on each plate. For all clusters, we analyzed their central regions, about 30′ × 30′ in size, which corresponds to ≈3 Mpc × 3 Mpc (below, we use $H_0 = 50$ km s^{-1} Mpc^{-1} and $q_0 = 0.5$). We chose the region center near the brightest galaxy in such a way that the density of galaxies brighter than $B = 17.^m5$–18^m reached a maximum within the region. For the photometric measurements, we visually selected all extended objects brighter than $19.^m5$–20^m in *B*, which is ~100 galaxies in each cluster, on the average.

We performed aperture photometry for selected galaxies. The background, where possible, was measured in a narrow band adjacent to the central aperture. If neighboring objects were a hindrance, we chose a clean background area near the measured galaxy. The aperture size exceeded the apparent galaxy size on plates by a factor of 1.5 to 2. A square or rectangular aperture was chosen depending on the degree of galaxy elongation and its orientation. We photometered close objects first with a large aperture, to obtain the total magnitude, and then each of them separately with the largest possible aperture (but without overlapping), in order to roughly estimate the contribution of each object to the total magnitude. To increase the accuracy and to keep track of the microdensitometer operation, we selected a series of check galaxies in A1291 and A1377 with published photometry. These galaxies were scanned at the beginning and at the end of each measuring session and subsequently used to reduce all measurements to the same photometric scale. The internal accuracy of determining the aperture magnitude was found by measuring the

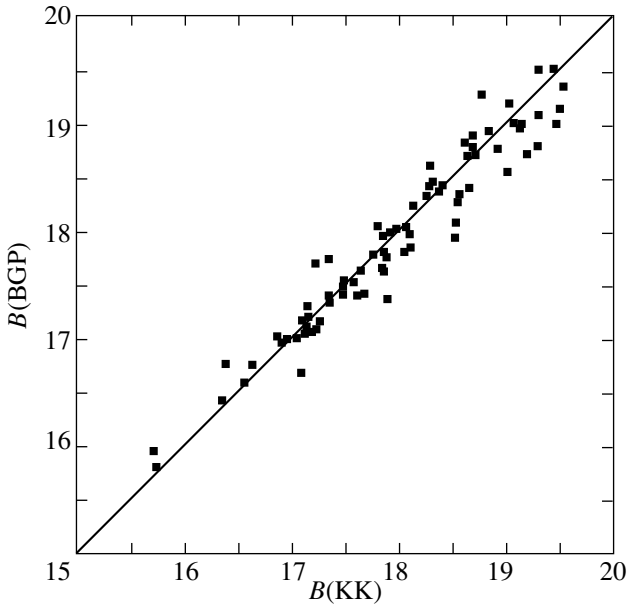

Fig. 1. Comparison of our photographic aperture magnitudes *B*(KK) and the photographic isophotal magnitudes *B*(BGP) from Bucknell *et al.* (1979) for A1377. The rms scatter is $0^m.22$.

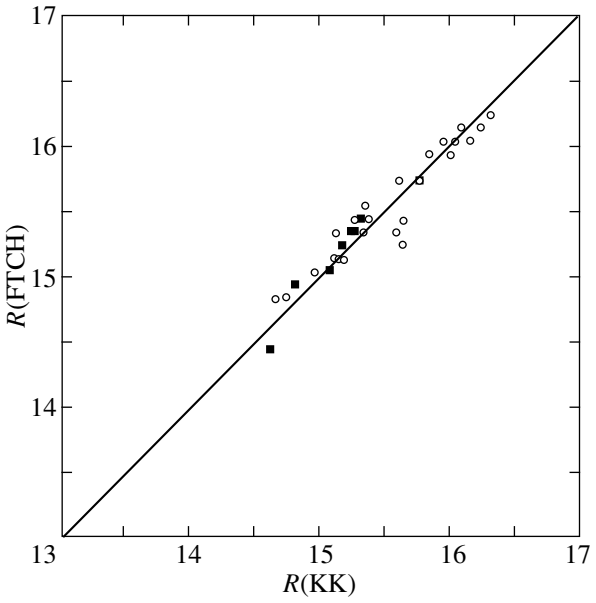

Fig. 2. Comparison of our total magnitudes *R*(KK) (squares and circles are for CCD and photographic data, respectively) and the total photographic magnitudes *R*(FTCH) from Flin *et al.* (1995) for A1377. The rms scatter is $0^m.11$.

same galaxies on different plates to be $0^m.07$ and $0^m.04$ in *B*- and *R*, respectively.

We calibrated the photographic magnitude scale in two steps by using two independent series of CCD observations for more than 100 galaxies together with photometric standards. The standard technique (Kopylova and Kopylov 1998) was used to reduce the CCD data. At the first step, we determined the zero point of our photographic system. *B*, *V*, and *R* CCD images (in Johnson-Cousins's system; below, all data are given in this system, unless stated otherwise) for six clusters (Anon1, Anon2, Anon3, A1377, A1383, and A1436) were obtained in 1992 with the 6-m telescope with a focal reducer for $1''.5$ seeing. The galaxies observed with CCD were measured in the same way (identical apertures for object and background) as those on plates. At the second step, we transformed the aperture magnitudes for all clusters to the total CCD *R* galaxy magnitudes measured with the 6- and 1-m telescopes from 1993 until 1999. Only for one cluster (A1270) does the correction m(CCD)–m(AMD) = $-0^m.013 \pm 0^m.040$ (the rms deviation is $0^m.107$) differ significantly from the mean correction of $-0^m.130 \pm 0^m.012$ (the rms deviation of corrections for ten galaxies is $0^m.038$) for the remaining clusters. Finally, given the distance-modulus differences between closer and more distant clusters, the uniform limit on absolute magnitude for our cluster sample is $B = -19^m.5$ and $R = -21^m.0$.

Table 2[1] gives the following parameters for 1192 measured galaxies in 11 clusters: (1) galaxy numbers; (2) and (3) equatorial coordinates (B1950.0); (4) and (5) *X* and *Y* coordinates (in arcsecs) relative to the cluster center chosen; (6) and (7) total *B* and *R* magnitudes, respectively; and (8) *B*–*R* color indices. In column (9), numbers 1, 2, and 3 mark cluster members with available radial velocities, foreground and background galaxies with measured radial velocities, and presumed (with a high probability) field galaxies, respectively; in column (10), galaxies with *R* CCD measurements (the *B* magnitudes were corrected in accordance with the *B*–*R* color index, which was left unchanged) are marked by letter "c".

Figures 1 and 2 compare our measurements with published photographic measurements. In Fig. 1, our *B* data for A1377 are compared with the data from Bucknell *et al.* (1979). Our aperture magnitudes agree with the isophotal magnitudes (25^m arcsec^{-2}) from the above paper with an rms scatter of $0^m.22$. In Fig. 2, our total *R* magnitudes for A1377 are compared with the photographic data from Flin *et al.* (1995), which were transformed to our magnitude scale, $R = F + 0.24$. In this case, the agreement is better ($0^m.11$). The three greatly deviating points in Fig. 2 correspond to interacting galaxies. The two brightest cluster galaxies (nos. 97 and 157) are not shown in Fig. 2 because their extended envelopes lie partially outside our CCD images, and we

[1] Table 2 is published in electronic form only and is accessible via ftp cdsarc.u-strasbg.fr/pub/cats/J (130.79.128.5) or http://cdswed.u-strasbg. fr/pub/cats/J.

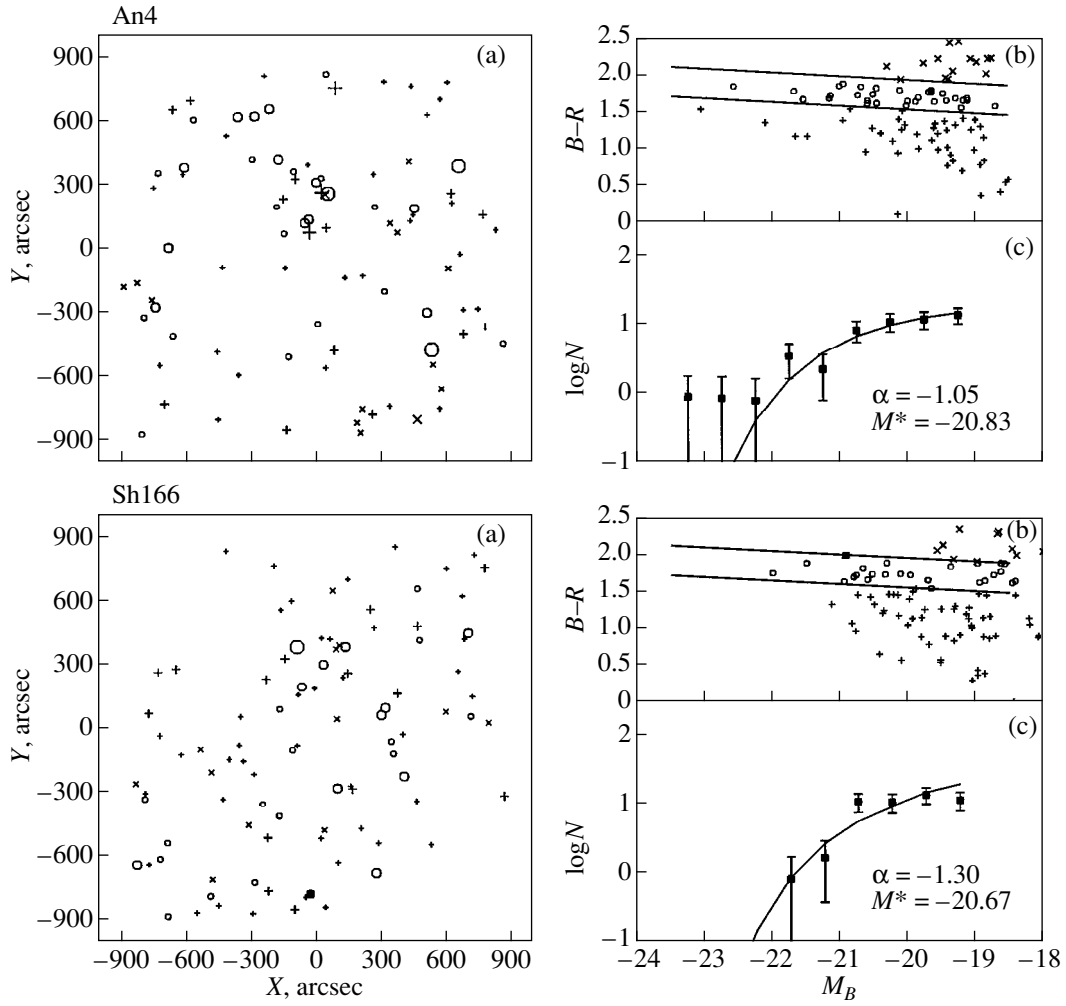

Fig. 3. Photometric data for 11 clusters. (a) The spatial distribution of cluster galaxies (cluster number is indicated above the figure, north is at the top, and east is to the left). The galaxies that fall within the band in the upper right corner, blue galaxies, red galaxies above the band, and field galaxies are indicated by circles, pluses, crosses, and filled squares, respectively; larger symbols correspond to brighter galaxies. (b) The color–magnitude $(B–R) – M_B$ diagram for the cluster; the middle line of the $0^m.4$-wide band corresponds to the equation $B–R = –0.05N_B + 0^m.74$. (c) The B luminosity function; the errors are defined as $\sqrt{n}$, where n is the number of objects in the interval.

determined the total magnitudes for these galaxies by fitting de Vaucouleurs's profiles ($r^{1/4}$) (de Vaucouleurs 1948) to the observed surface brightness profiles. The same technique was used to determine the parameters of several more brightest galaxies: no. 74 in A1291; nos. 80 and 19 in A1318; and no. 61 in Anon1.

Figure 3 shows a set of three figures for each cluster (the number is given at the top). The spatial distribution of galaxies in the central cluster regions is shown on the left. The early-type galaxies that fall within the band (upper right in the figures), blue galaxies, very red (presumably background) objects, and field galaxies are indicated by circles, pluses, crosses, and filled squares, respectively. Larger symbols correspond to brighter galaxies with a separation into three magnitude intervals ($< –21^m.5$, $> –20^m.0$, and intermediate). The color–magnitude $(B–R)$–M_B diagrams for clusters are shown in the upper right corner. A sequence of early-type galaxies is clearly distinguished in these diagrams. The upper and lower lines in these figures lie $0^m.2$ above and below the middle line of the band given by the equation $B – R = –0.05M_B + 0^m.74$, which was derived by linear regression (this dependence for bright field ellipticals was first found by Baum (1959)). Such a detection of early-type galaxies was analyzed for several clusters (see, e.g., Visvanathan and Sandage 1977; Andreon *et al.* 1997; Molinari and Smareglia 1998; Gladders *et al.* 1998, Garilli *et al.* 1999). Garilli *et al.* showed that using two colors increased the accuracy of identifying cluster members.

LUMINOSITY FUNCTION

The differential luminosity function (LF) $\Phi(M)dM$ gives the number of galaxies with total magnitudes in

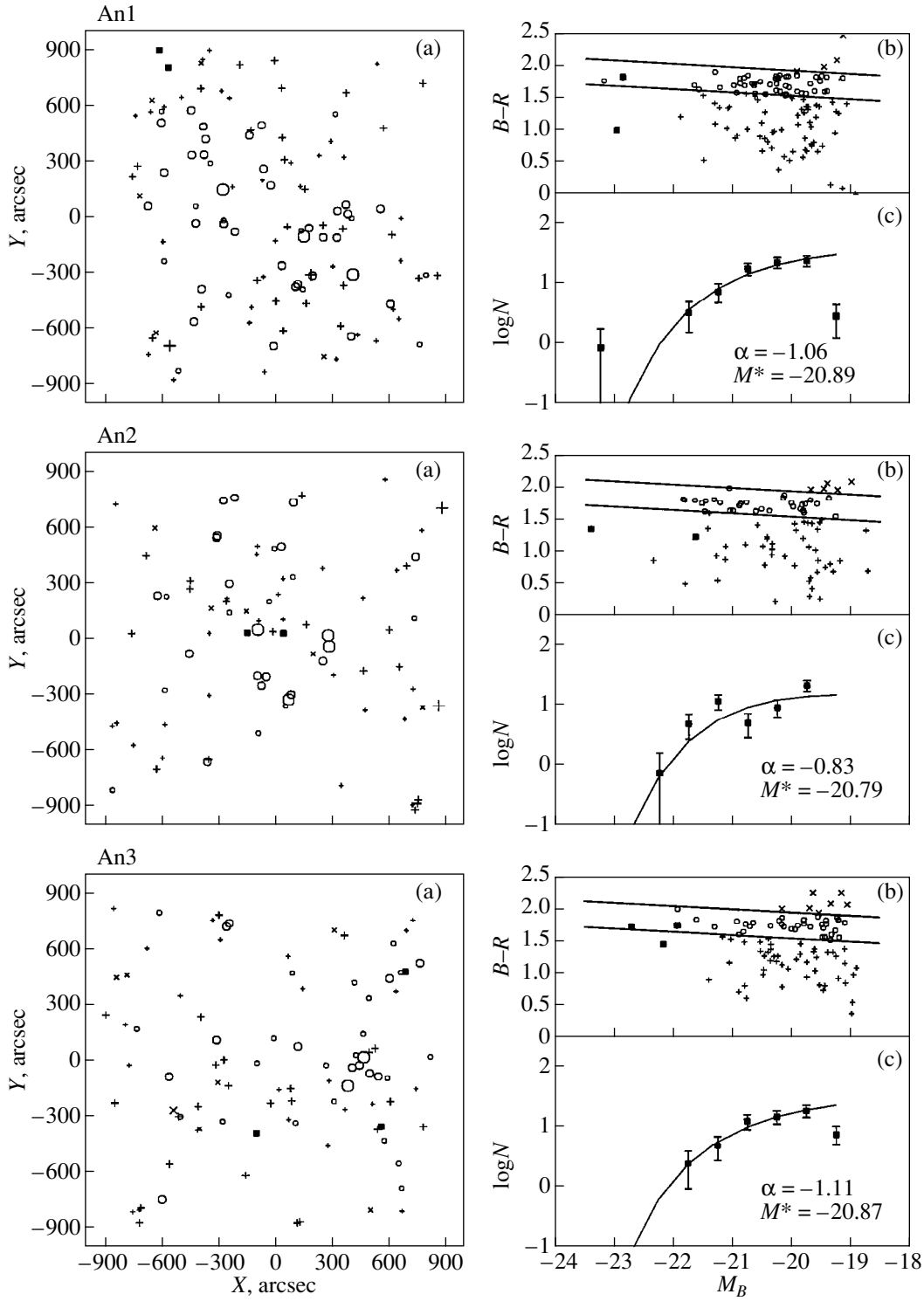

Fig. 3. (Contd.)

the interval $[M, M + dM]$. It is usually fitted by the function introduced by Schechter (1976):

$$\Phi(M) = (0.4\ln 10)\Phi^*(10^{0.4(M^*-M)})^{1+\alpha} \times \exp(-10^{0.4(M^*-M)}),$$

where α is the slope of the dependence for faint magnitudes, M^* is the characteristic magnitude known as the "break" of the luminosity function, and Φ^* is the normalization constant.

In order to construct the LF, we transformed the observed magnitudes of galaxies (Table 2) to absolute

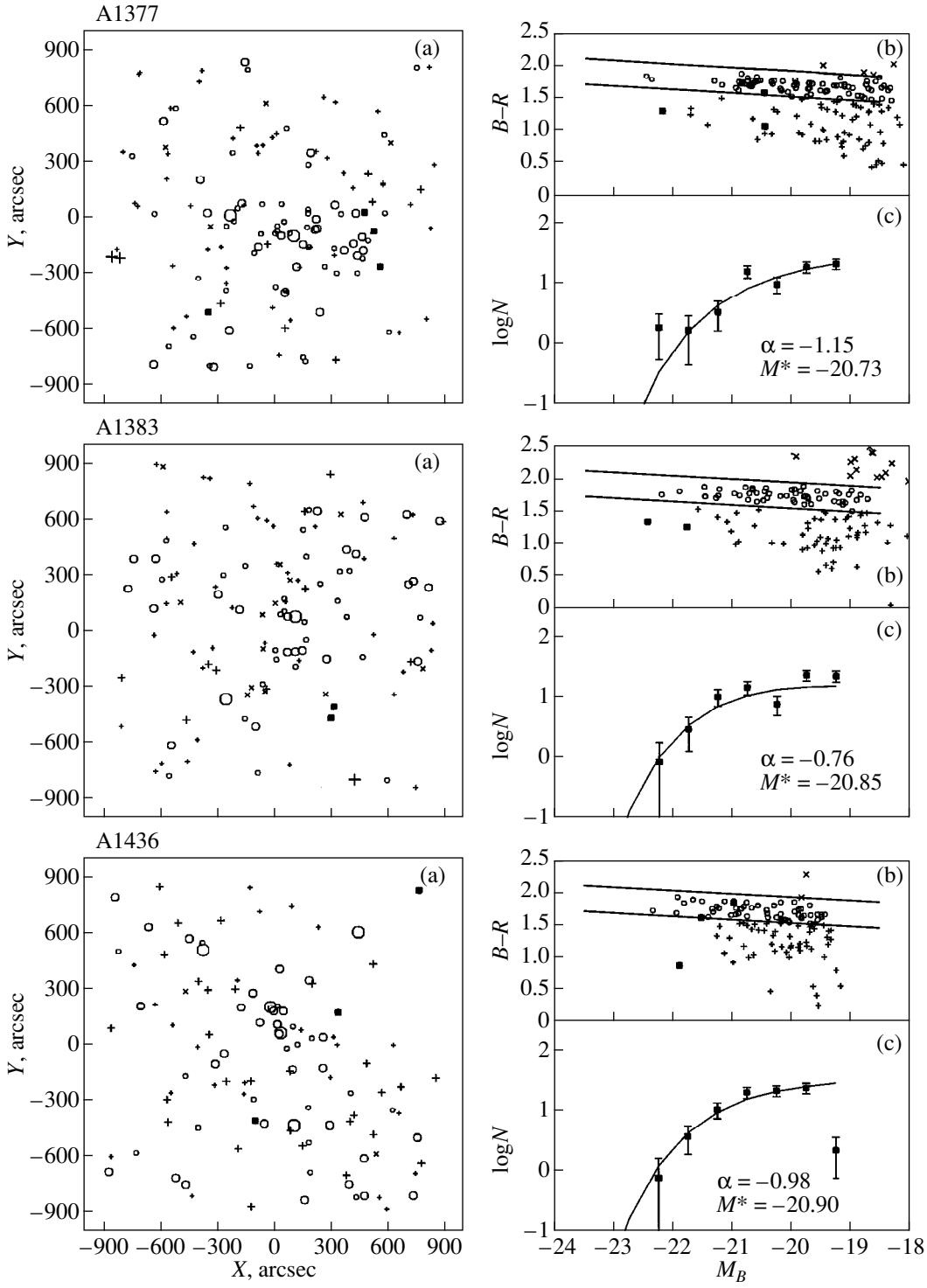

Fig. 3. (Contd.)

magnitudes in accordance with the cluster radial velocities (Table 1). We then applied a *K* correction for early-type galaxies and a correction for evolution (Poggianti 1997) to these magnitudes. Galaxies were counted in $0^m.5$ intervals. To take into account field galaxies in our counts, we used the *B* data from Maddox *et al.* (1990) and subtracted the background in each interval. For the *R* band, we used the Las-Campanas Redshift Survey (LCRS) counts (Lin *et al.* 1996). Subsequently, we estimated parameters of the Schechter function (M^* and α) for the LF of each cluster by nonlinear least-squares fitting. The constant Φ^* was set equal to the total number of cluster galaxies (with field galaxies subtracted)

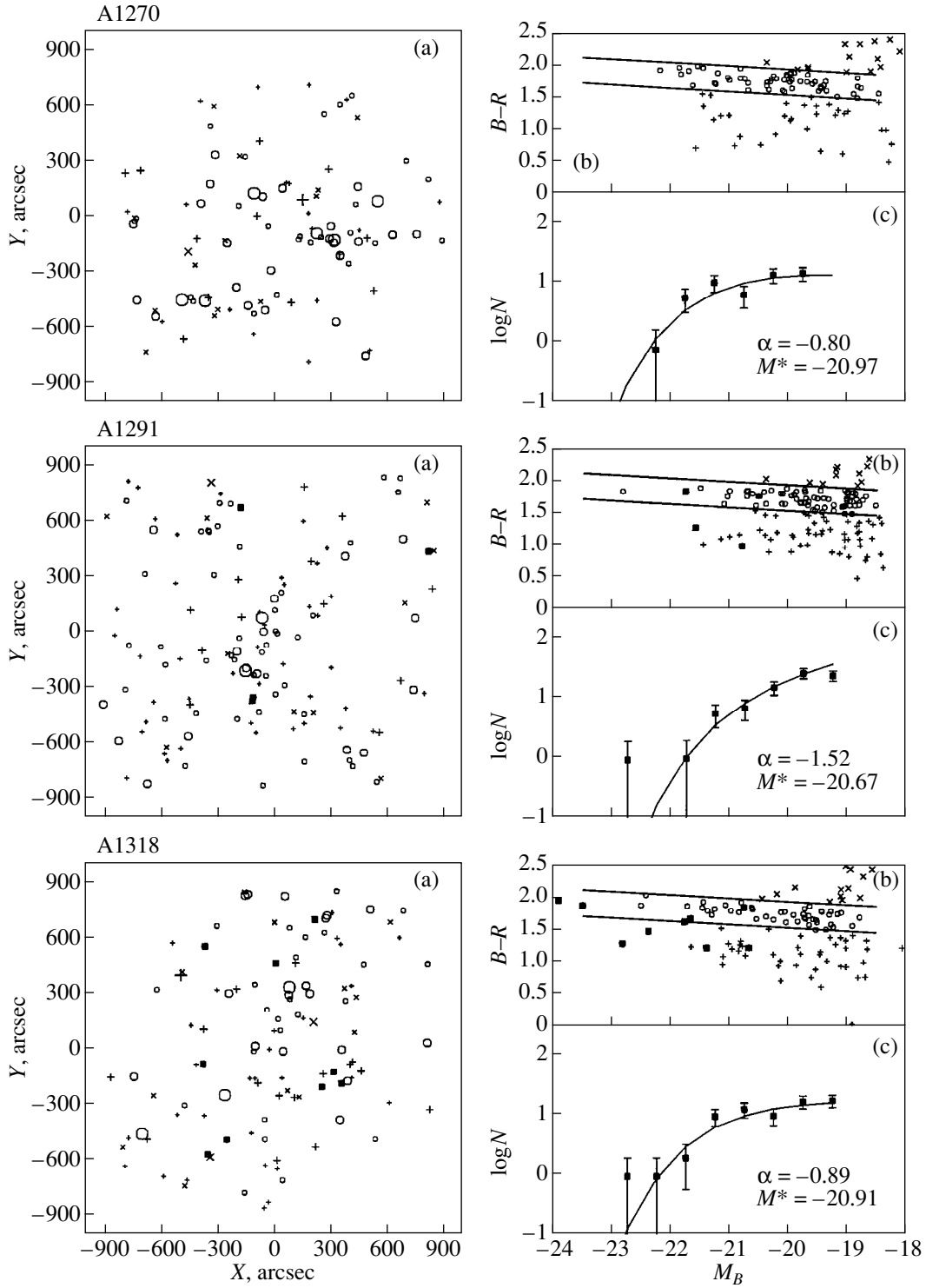

Fig. 3. (Contd.)

within the magnitude range in which the LF was fitted. When determining the parameters, we excluded the brightest galaxy in A1291, A1318, and Anon1, and the two brightest galaxies in A1377 and in Anon4. Figure 3 (lower right corner) shows the LF of each cluster. The LF parameters are summarized in Table 3: columns 2 and 3 give α and M_B^* with their rms errors, respectively, and column 4 gives Φ^*.

The composite LF, especially its bright end, has been constructed more than once. To construct it, we added up the galaxy counts in all clusters (after subtracting field galaxies) in the corresponding intervals.

Table 3. Parameters of the Schechter function

Cluster	α	M_B^*	Φ*	Cluster	α	M_B^*	Φ*
A1377	–1.15 ± 0.30	–20.73 ± 0.20	56.2	Anon4	–1.05 ± 0.20	–20.83 ± 0.15	40.2
Sh166	–1.30 ± 0.27	–20.67 ± 0.16	37.9	A1436	–0.98 ± 0.10	–20.90 ± 0.08	87.6
A1291	–1.52 ± 0.14	–20.67 ± 0.08	56.7	Anon3	–1.11 ± 0.09	–20.87 ± 0.07	56.7
A1318	–0.89 ± 0.18	–20.91 ± 0.15	53.9	A1270	–0.80 ± 0.21	–20.97 ± 0.19	51.0
A1383	–0.76 ± 0.34	–20.85 ± 0.26	61.0	Anon1	–1.06 ± 0.09	–20.89 ± 0.08	81.7

Table 4. Luminosity-function parameters for various samples

Sample	*N*	α	*M**	Limit
Stromlo–APM (Loveday *et al.* 1992)	Field	–0.97 ± 0.15	–20.86 ± 0.13	$M_{b_j} \sim -17.5$
Colless (1989)	14	–1.21	–21.40	$M_{b_j} < -19.5$
Lumsden *et al.* (1997)	22	–1.22 ± 0.04	–21.42 ± 0.02	$M_{b_j} < -19.5$
Valotto *et al.* (1997)	55	–1.40 ± 0.1	–21 36 ± 0.1	$M_{b_j} < -18.5$
Norris (Small *et al*. 1997)	CrB[1]	–1.10 ± 0.15	–21.40 ± 0.34	$M_{B_{AB}} < -18.6$
	A2069[1]	–1.06 ± 0.18	–20.82 ± 0.26	$M_{B_{AB}} < -19$
Kopylov and Kopylova (this paper)	UMa[1]	–1.02 ± 0.06	–20.91 ± 0.05	$M_B < -19.5$
LCRS (Lin *et al.* 1996)	Field	–0.70 ± 0.05	–22.13 ± 0.02	$M_r < -16.5$
Norris (Small *et al*. 1997)	Field	–1.04 ± 0.17	–22.29 ± 0.30	$M_r < -17.0$
Hunsberger and Charlton (1998)	39[2]	–0.52	–22.35	$M_R \sim -18.25$
Yamagata and Maehara (1986)	6[3]	–1.07 ± 0.04	–22.11 ± 0.10	$M_V < -17.1$
Oegerle and Hoessel (1989)	8	–1.25	–22.27	$M_R < -19$
Lugger (1989)	9	–1.21 ± 0.09	–22.81 ± 0.13	$M_R < -20$
Gaidos (1997)	20	–1.09 ± 0.08	–22.63 ± 0.11	$M_R < -18.9$
Lopez-Cruz *et al.* (1997)	45	–1.04 ± 0.05	–22.53 ± 0.09	$M_R < -20$
Garilli *et al.* (1999)	65[4]	–0.95 ± 0.06	–22.53 ± 0.12	$M_r \sim -18.5$
Kopylov and Kopylova (this paper)	UMa[1]	–1.06 ± 0.07	–22.39 ± 0.06	$M_R < -21.0$

[1] Supercluster of galaxies.
[2] Compact groups.
[3] Poor clusters.
[4] Isophotal magnitudes.

Parameters of the Schechter function of the composite LF were determined in the same way as they were for individual clusters (see Table 4). Table 4 also summarizes some of the results obtained by various authors for field galaxies, groups, clusters, and superclusters (column 1 gives a reference to the sample). The second column gives the number of clusters used or the supercluster name. For a convenient comparison of the results of different authors, we reduced *M**, where necessary, to $H_0 = 50$ km s^{-1} Mpc^{-1} and transformed them as follows: $B = b_j + 0.14$; $B = B_{AB} + 0.14$, $R = V - 0.54$, and $R = r - 0.34$. The limiting magnitude in the last column is given in the original photometric band.

Figure 4 shows the composite LF in *B* and, for comparison, the LF of the Corona Borealis supercluster from Small *et al.* (1997) normalized to our LF at $-20\overset{m}{.}0$.

DISCUSSION

An analysis of the data in Table 4 shows that the parameters of our LF in *B* are close to those of the LFs for field galaxies (Stromlo–APM) and, at the same, to those of the LFs for the A2069 supercluster and for poor clusters. In the *R* band, *M** is $0\overset{m}{.}26$ brighter and α is 0.36 larger than those for LF field galaxies (LCRS), but close to the LF field values obtained in the Norris survey.

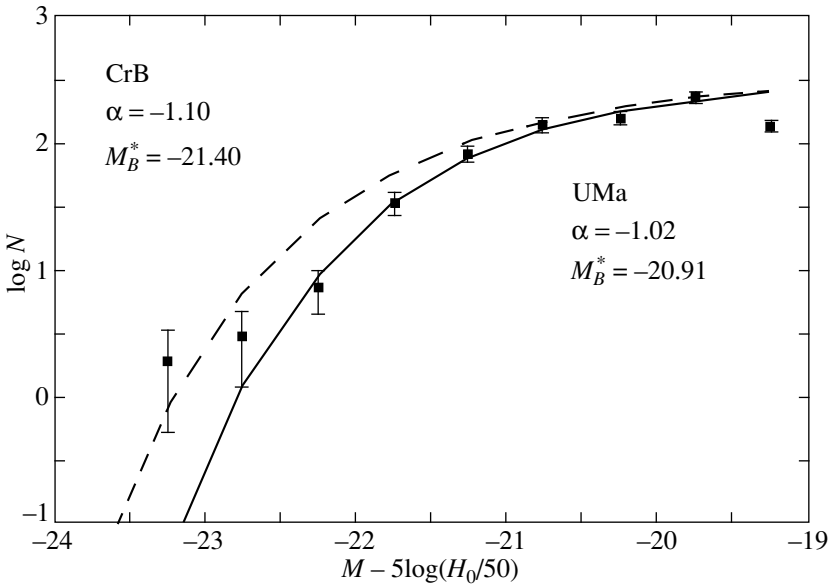

Fig. 4. Composite *B* LF for the Ursa Major supercluster. The dashed line represents the LF of the Corona Borealis supercluster (Small *et al.* 1998) normalized to our LF at $-20^m.0$. The error is defined as $\sqrt{n}$, where *n* is the number of objects in the interval.

As we see from Fig. 4, the Ursa Major supercluster, in contrast to the Corona Borealis supercluster (with M^* brighter than that for Ursa Major by $\approx 0^m.5$), exhibits no excess of bright clusters. The Corona Borealis supercluster is unique. As our direct measurements of photometric distances show, the nucleus of this system is most likely to be at the stage of gravitational contraction (Kopylova and Kopylov 1998).

The formation of galaxies in the Corona Borealis supercluster appears to have begun at an earlier epoch than that in field galaxies, which is reflected in the LF. The formation of clusters in the Ursa Major supercluster, which is at a relatively earlier stage of isolation from the global expansion of the Universe, takes place at the current epoch. Galaxy mergers, which affect the bright end of the LF, are apparently also far from being complete.

Apart from analyzing the LF per se, our goal was to select early-type galaxies in all clusters of the supercluster in the same way. Based on the color-magnitude diagram and choosing galaxies in the band ($-0.05M_B + 0^m.54 \le B–R \le -0.05M_B + 0^m.94$) and their redshifts, we drew a sample of E and S0 cluster galaxies. We used these galaxies to determine the photometric distances to clusters and the spatial structure of the supercluster along the line of sight (Kopylova and Kopylov 2001; see Kopylova and Kopylov (1996) for preliminary results).

ACKNOWLEDGMENTS

We wish to thank R. Ziener, who obtained observational data with the Tautenburg telescope, an O. Dobrodiĭ, G. Korotkova, and Ts. Georgiev for help in preparing and on the initial stage of plate measurement with AMD-2.

REFERENCES

1. G. O. Abell, Astrophys. J., Suppl. Ser. **3**, 211 (1958).
2. G. O. Abell, H. G. Corwin, Jr., and R. P. Olowin, Astrophys. J., Suppl. Ser. **70**, 1 (1989).
3. V. L. Afanas'ev, V. A. Lipovetskiĭ, V. P. Mikhaĭlov, *et al.*, Otchet SAO, No. 138 (1986).
4. S. Andreon, E. Davoust, and T. Heim, Astron. Astrophys. **323**, 337 (1997).
5. F. W. Baier, Astron. Nachr. **301**, 17 (1980).
6. W. A. Baum, Publ. Astron. Soc. Pac. **71**, 106 (1959).
7. M. J. Bucknell, J. G. Godwin, and J. V. Peach, Mon. Not. R. Astron. Soc. **188**, 579 (1979).
8. M. Colless, Mon. Not. R. Astron. Soc. **237**, 799 (1989).
9. S. V. Drabek, I. M. Kopylov, N. N. Somov, and T. A. Somova, Astrofiz. Issled. (Leningrad) **22**, 64 (1986).
10. M. Einasto, E. Tago, J. Laaniste, J. Einasto, and H. Andernach, Astron. Astrophys., Suppl. Ser. **123**, 119 (1997).
11. P. Flin, D. Trévese, G. Cirimele, and P. Hickson, Astron. Astrophys., Suppl. Ser. **110**, 313 (1995).
12. E. Gaidos, Astron. J. **113**, 117 (1997).
13. B. Garilli, D. Maccagni, and S. Andreon, Astron. Astrophys. **342**, 408 (1999).
14. M. Gladders, O. López-Cruz, H. K. Yee, and T. Kodama, Astrophys. J. **501**, 571 (1998).
15. S. D. Hunsberger and J. C. Charlton, Astrophys. J. **505**, 536 (1998).
16. A. I. Kopylov and F. G. Kopylova, Bull. Spec. Astrophys. Obs. **39**, 44 (1996).

17. F. G. Kopylova and A. I. Kopylov, Pis'ma Astron. Zh. **24**, 573 (1998) [Astron. Lett. **24**, 491 (1998)].
18. F. G. Kopylova and A. I. Kopylov, Pis'ma Astron. Zh. (in press) [Astron. Lett. (in press)].
19. H. Lin, R. P. Kirshner, S. A. Shectman, *et al.*, Astrophys. J. **464**, 60 (1996).
20. O. López-Cruz, H. K. Yee, J. P. Brown, *et al.*, Astrophys. J. Lett. **475**, L97 (1997).
21. J. Loveday, B. A. Peterson, G. Efstathiou, and S. Maddox, Astrophys. J. **390**, 338 (1992).
22. P. Lugger, Astrophys. J. **343**, 572 (1989).
23. S. L. Lumsden, C. A. Collins, R. C. Nichol, *et al.*, Mon. Not. R. Astron. Soc. **290**, 119 (1997).
24. S. J. Maddox, G. Efstathiou, and W. J. Sutherland, Mon. Not. R. Astron. Soc. **246**, 433 (1990).
25. M. R. Merrifield and S. M. Kent, Astron. J. **98**, 351 (1989).
26. M. R. Merrifield and S. M. Kent, Astron. J. **101**, 783 (1991).
27. E. Molinari and R. Smareglia, Astron. Astrophys. **330**, 447 (1998).
28. W. R. Oegerle and J. G. Hoessel, Astron. J. **98**, 1523 (1989).
29. B. M. Poggianti, Astron. Astrophys., Suppl. Ser. **122**, 399 (1997).
30. P. Schechter, Astrophys. J. **203**, 297 (1976).
31. S. A. Shectman, Astrophys. J., Suppl. Ser. **57**, 77 (1985).
32. T. A. Small, W. L. W. Sargent, and D. Hamilton, Astrophys. J. **487**, 512 (1997).
33. C. A. Valotto, M. A. Nicotra, H. Muriel, and D. G. Lambas, Astrophys. J. **479**, 90 (1997).
34. G. de Vaucouleurs, Ann. Astrophys. **11**, 247 (1948).
35. N. Visvanathan and A. Sandage, Astrophys. J. **216**, 214 (1977).
36. A. I. Zabludoff, M. J. Geller, J. P. Huchra, and M. S. Vogeley, Astron. J. **106**, 1273 (1993).
37. T. Yamagata and H. Maehara, Publ. Astron. Soc. Pacif. **38**, 661 (1986).

Translated by A. Dambis

Astronomy Letters, Vol. 27, No. 3, 2001, pp. 150–155. Translated from Pis'ma v Astronomicheskiĭ Zhurnal, Vol. 27, No. 3, 2001, pp. 180–186.

Caustic Crossing in the Gravitational Lens Q2237 + 0305

V. N. Shalyapin*

Institute of Radio Astronomy, National Academy of Sciences of Ukraine, Kharkov, Ukraine

Received April 4, 2000; in final form, September 13, 2000

Abstract—The monitoring of the gravitational lens Q2237 + 0305 carried out by the OGLE group during 1997–2000 is analyzed. The significant light amplifications in the C and A quasar components with maxima in mid- and late 1999, respectively, are interpreted as the crossing of microlens caustics by the source. A constraint on the emitting-region size $R \leq 10^{15}$ cm has been obtained from the light-curve shape by assuming a power-law quasar brightness distribution $(r^2 + R^2)^{-p}$. To estimate the exponent $p \sim 1.2$ requires refining the standard model for the quasar continuum formation in an optically thick accretion disk with $p = 1.5$. © *2001 MAIK "Nauka/Interperiodica".*

Key words: *quasars, gravitational lenses, accretion disks*

1. INTRODUCTION

Quasar variability under the effect of microlenses depends both on parameters of the mass distribution for compact bodies and on the appearance of the emitting region. For instance, the larger the quasar, the smaller the amplitudes of light variations in its images. Thus, it becomes possible to formulate the inverse problem of determining the sizes and structure of quasars from their observed light curves. The main difficulty in solving this problem is that the distribution of the amplification produced by microlenses is not known in advance and exhibits a fairly complex pattern with many randomly located caustic lines [see, e.g., Zakharov (1997) and Zakharov and Sazhin (1998)]. In general, the specific form of this distribution is not known in advance and can be analyzed only statistically. Exceptions are only those portions of the light curve that correspond to caustic crossing by the quasar. The amplification of a point source during caustic crossing obeys a simple law: it remains approximately constant as the caustic is approached, then abruptly increases to infinity at the caustic itself, and subsequently falls off as $x^{-1/2}$ with increasing distance x from the caustic (Chang and Refsdal 1984; Blandford and Narayan 1986).

Microlenses show up most clearly in the multiple quasar images produced by the gravitational effect of galaxy macrolenses. First, the microlensing probability is rather high in such situations. Second, intrinsic quasar variability can, in principle, be separated from microlensing variability. Of all the gravitationally lensed quasars, Q2237 + 0305 ($z_s = 1.675$) is undoubtedly the most promising object for microlensing analysis. Because of the unique proximity of a lensing galaxy ($z_l = 0.039$), microlensing variability in this object must take place faster than in other objects by an order of magnitude and with a large amplitude.

The quasar Q2237 + 0305 has been monitored virtually since its discovery, and it actually proved to be the first object in which microlensing variability was detected (Irwin *et al.* 1989; Corrigan *et al.* 1991). The observations by Østensen *et al.* (1996) showed that virtually all four quasar images were more or less variable.

The regularity and quality of the Q2237 + 0305 monitoring have improved markedly when the OGLE group joined it in the last four years (Wozniak *et al.* 2000) (see Fig. 1). Measurements are made in the *V* band approximately once a week during the observing season from May through December. The latest observations (http://www.astro.princeton.edu/~ogle/ogle2/huchra.html) show that image C passed its intensity peak in mid-1999, while image A peaked in late 1999. Interpreting the light-curve maxima as resulting from caustic crossing allows the size and structure of the quasar emitting region in the object under study to be determined.

2. AMPLIFICATION OF AN EXTENDED SOURCE IN THE CAUSTIC REGION

When a source crosses a caustic line, an additional pair of images appears (or disappears). The total intensity of this pair depends on the distance to the caustic as $x^{-1/2}$. Therefore, the intensity of a point source in the caustic region can be represented as (Schneider and Weiss 1987)

$$I_p(x) = I_0 + \theta(x) a_0 x^{-1/2}. \quad (1)$$

Here, I_0 is the intensity of all the remaining microimages except the additional pair; $\theta(x)$ is the Heaviside

* E-mail address for contacts: vshal@ira.kharkov.ua

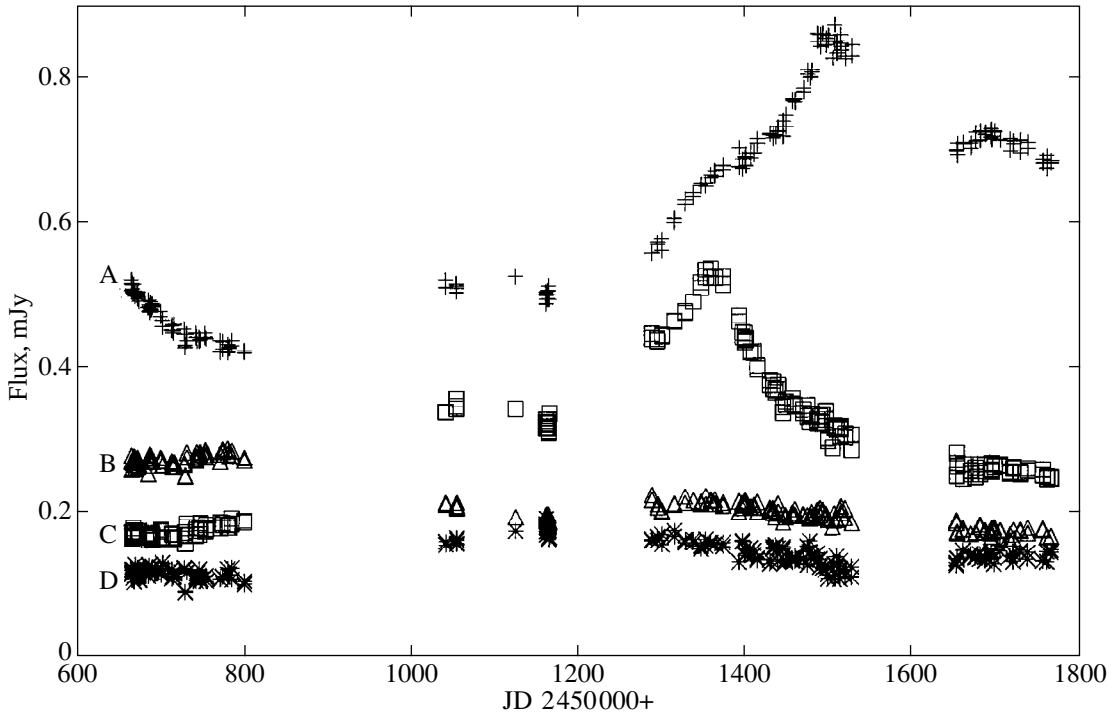

Fig. 1. *V* light variations of the four images of the quasar Q2237 + 0305 during 1997–2000 as observed by the OGLE group.

unit function; and a_0 is the caustic strength. The amplification of an extended source with a brightness distribution $P(r)$ can be calculated by ordinary summation over the set of infinitely small sources with individual implification factors:

$$I = [\int d\mathbf{r} P(\mathbf{r}) I_p(\mathbf{r})]/[\int d\mathbf{r} P(\mathbf{r})]. \quad (2)$$

To describe the brightness distribution in the source, we use a power-law model

$$P(r) = \left(1 + \frac{r^2}{R^2}\right)^{-p} \quad (p > 0), \quad (3)$$

which is determined by the source radius R and by the rate of brightness decline p.

Let the source center be at a distance D from the caustic line. In the normalized coordinates $\xi = x/R$ and $\eta = y/R$ and using normalized distance $d = D/R$, we obtain

$$I = I_0 + a_0 R^{-1/2} J(d), \quad (4)$$

where the function $J(d)$ is

$$J(d) = \left[\int_{-\infty}^{+\infty} d\eta \times \int_0^{+\infty} d\xi P(\xi, \eta)\xi^{-1/2}\right] / \left[\int_{-\infty}^{+\infty} d\eta \int_{-\infty}^{+\infty} d\xi P(\xi, \eta)\right] \quad (5)$$

or, taking into account the symmetry in η and the total intensity

$$\int P(r) dr = \frac{\pi R^2}{p-1}, \quad (6)$$

we obtain:

$$J(d) = 2\frac{p-1}{\pi}\int_0^\infty d\xi \int_0^\infty d\eta \xi^{-\frac{1}{2}}[1 + (\xi - d)^2 + \eta^2]^{-p}. \quad (7)$$

Taking the internal integral over η yields

$$J(d) = \frac{p-1}{\pi}\int_0^\infty d\xi \mathrm{B}\left(\frac{1}{2}, p - \frac{1}{2}\right) \times \xi^{-1/2}[\xi^2 - 2\xi d + d^2 + 1]^{\frac{1}{2} - p}, \quad (8)$$

where B is the beta function. The subsequent integration over ξ yields

$$J(d) = \frac{\Gamma\left(p - \frac{1}{2}\right)\Gamma\left(2p - \frac{3}{2}\right)}{\Gamma(p-1)\Gamma(2p-1)} \times (1 + d^2)^{\frac{3}{4} - p} {}_2F_1\left(\frac{1}{2}, 2p - \frac{3}{2}; p; \frac{1}{2}\left(1 + \frac{d}{\sqrt{1 + d^2}}\right)\right). \quad (9)$$

Here, Γ and ${}_2F_1(a; b; c; z)$ are the gamma function and the Gauss hypergeometric function, respectively.

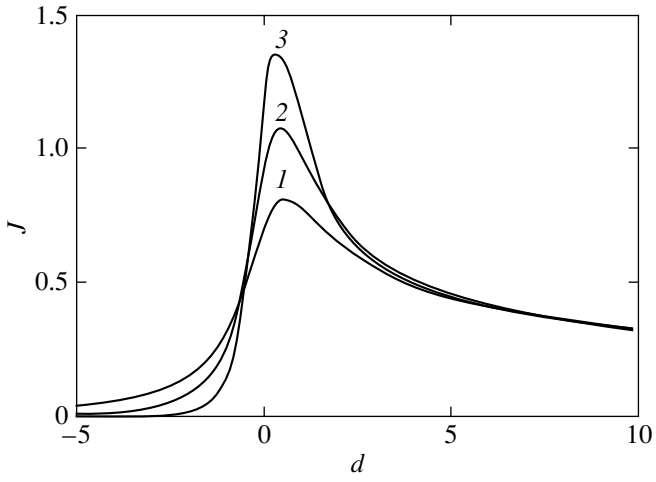

Fig. 2. Function $J(d)$ for several exponents p: for p = (*1*) 1.5, (*2*) 2.0, and (*3*) 3.0.

Figure 2 shows the function $J(d)$ for several values of p. We clearly see from the figure that the sharpness of the jump in amplitude increases with increasing source brightness concentration toward the center during caustic crossing, tending to an infinite point-source limit for very large p.

For some particular p values, for example, for $p = 3/2$, 2, and 3, the hypergeometric function can be expressed as a combination of elementary and other special functions. Thus, we have for $p = 3/2$

$$J(d)|_{p=3/2} = [2(1+d^2)((1+d^2)^{1/2} - d)]^{-1/2}. \quad (10)$$

3. VARIABILITY ANALYSIS

We see from Fig. 1 that the intensities of all four quasar images have varied during the last four years. The largest variations were observed in image C, which passed its maximum in mid-1999, and in image A, which reached its maximum in late 1999. The approach to interpreting the variability of these two images is the same. Let us assume that, in both cases, the source crosses the caustic; the brightness distribution must follow the law (4). The general form of the curve depends on five parameters:

(1) Contribution I_0 from the remaining microimages, which is assumed to be approximately constant;

(2) Caustic strength a_0;

(3) The time it takes for the source to cross its radius Δt of the source, which is proportional to the source size R;

(4) The time t_0 of caustic crossing by the source center;

(5) Exponent p in the brightness distribution (3).

Estimating the five parameters reduces to minimizing the sum of the squared differences between model and observed light curves

$$\chi^2 = \sum_{i=1}^{N} \frac{1}{\sigma_i^2}[I_{\text{model}}(I_0, a_0, \Delta t, t_0, p) - I_{\text{obs}}]^2. \quad (11)$$

The summation is performed over all N points of observations with weights that are inversely proportional to the squares of the observational errors σ_i.

The best set of parameters is sought by the Marquardt method [see, e.g., Chapter 15.5 in the book by Press *et al.* (1992)].

3.1. Image A

The model parameters estimated from the light curve of image A with 218 data points during the entire observing period are given in the table. The combination $a_0/\Delta t$ is more convenient to calculate than the caustic strength a_0. The listed formal accuracies of the parameter estimates should be considered only as their lower limits.

Figure 3 shows the model light curve together with measured values. The 1997 observations are poorly fitted by a single curve, implying that approaching the caustic did not show up in the first year. Such a behavior is characteristic of numerical microlensing models for Q2237 + 0305, in which one amplification event is often superimposed on another to form complex light curves. Excluding the 1997 data from our analysis, while significantly improving the total χ^2 residual, affects the parameter estimates only slightly.

When the caustic is crossed in image A, an additional pair of images emerges. A characteristic feature of this direction of motion is a steep rise in light amplification followed by a gentler decline. The dashed line in Fig. 3 represents the expected behavior of image A in the immediate future. We assume that the brightness will continue to decline and (if no additional causes of amplification arise) will reach the original 1997 level in two to three years.

3.2. Image C

Attempts to fit the light curve of image C over the entire observed period have failed. At the same time, excluding 80 data points for 1997 from our analysis results in quite reasonable estimates, which are given in the table and shown in Fig. 4. Interestingly, the best solution corresponds to caustic crossing in the negative direction, with *the pair of images disappearing*. The local minimum of χ^2 corresponding to the motion in the positive direction is several times greater than the absolute minimum reached during the motion in the negative direction.

The inability to fit the entire observed period by a single curve becomes more understandable in light of the recent results by Wyithe *et al.* (2000). These authors argue that the intensity variations in image C have been composite in pattern during the last four years, and, it is

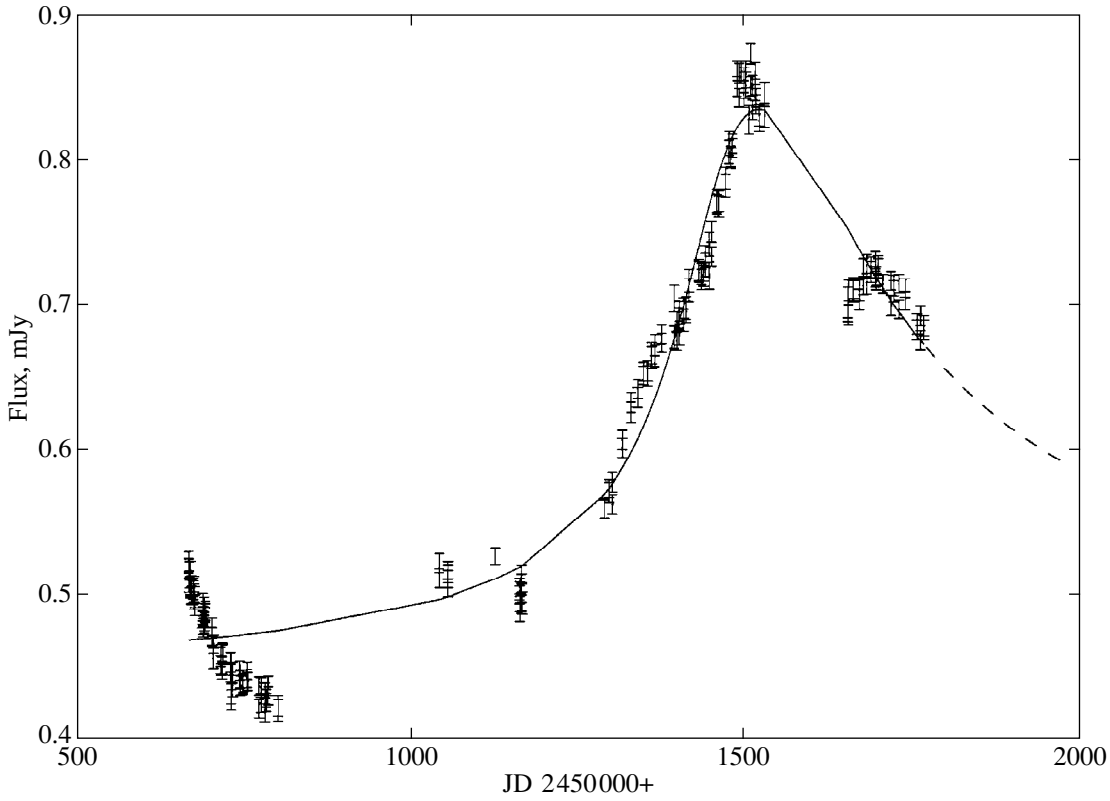

Fig. 3. Variability of image A during 1997–2000. Observational data, model, and forecast (dashed line).

quite possible that another caustic crossing was overlooked during the observing seasons in 1997 and 1998.

The dotted and dashed lines indicate the best extrapolation computed in the model with a single caustic crossing in 1997 and our forecast until the end of 2000, respectively. No appreciable intensity variations in image C are expected in the immediate future.

4. THE SIZE AND STRUCTURE OF THE QUASAR-EMITTING REGION

For the quasar radius estimates Δt in time units to be transformed to linear sizes R, we must know the apparent quasar velocity; only the velocity component $v_\perp$ is perpendicular to the caustic line is important. Of course, the exact velocity is unknown. Nevertheless, a statistical analysis of the time derivatives of brightness variations by Wyithe *et al.* (1999) yielded an upper limit of $v < 500$ km s^{-1}. The perpendicular velocity component can only be lower than this value. The most probable value of $v_\perp$ was found to be 300 km s^{-1}.Given the angular distances from the observer to the quasar (D_{os}) and to the lens (D_{ol}) in the model of a flat Universe with H_0 = 60 km s^{-1} Mpc^{-1}, the most probable source radius is estimated to be

$$R = v_\perp \Delta t \frac{D_{os}}{D_{ol}} \sim 2.0 \times 10^{13} \left(\frac{v_\perp}{300 \text{ km s}^{-1}}\right)\left(\frac{\Delta t}{1 \text{ day}}\right) \text{ cm}. \quad (12)$$

Using the crossing time Δt_A = 90 days for image A gives the most probable quasar radius $R = 1.8 \times 10^{15}$ cm, while substituting the crossing time for image C, Δt_C = 30 days, reduces this estimate to $R = 6 \times 10^{14}$ cm. At the same time, the velocity constraint $v < 500$ km s^{-1} together with the crossing time Δt_C give an upper limit on the source radius, $R \le 10^{15}$ cm.

Another parameter that characterizes the mass distribution is the exponent p. It follows from the table that its computed value lies between 1.1 and 1.25. It is interesting to note that different models for the quasar structure can lead to different dependences of the emissivity on distance from the center. For instance, a power-law

Best-fit model parameters

Image	I_0	$a_0/\Delta t$	Δt	t_0	p
A 1997–2000	0.44 ± 0.01	0.73 ± 0.07	91 ± 4	1462 ± 1	1.24 ± 0.03
C 1998–2000	0.22 ± 0.01	0.95 ± 0.15	–29 ± 2	1390 ± 1	1.10 ± 0.02

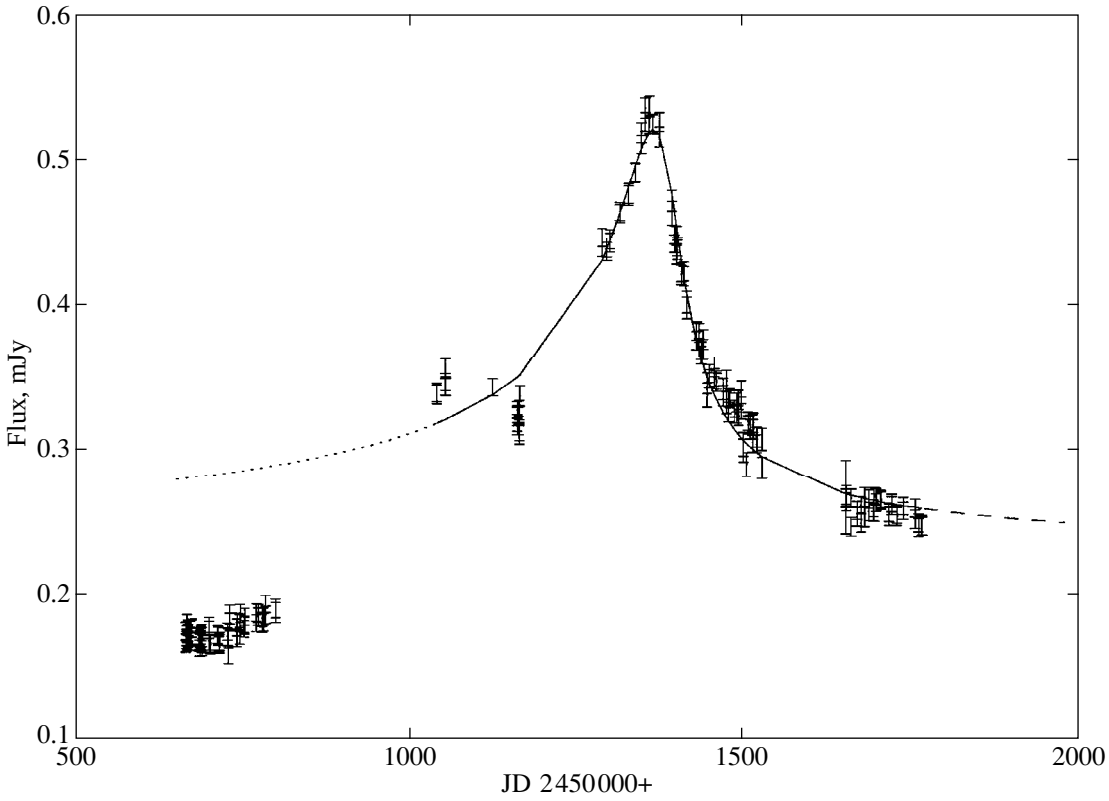

Fig. 4. Light curve of image C during 1997–2000. Observations, model (dotted line), and forecast (dashed line).

dependence with $p \le 0.5$ follows from the model of an optically thin accretion disk (Manmoto *et al.* 1997). At the same time, the standard model of an optically-thick accretion disk yields an r^{-3} dependence (Shakura and Sunyaev 1973), which changes to $(r^2 + R^2)^{-3/2}$ for a finite radius. Our estimate $p \sim 1.2$ favors the standard model, but more complex accretion-disk models should be analyzed to achieve better agreement.

5. DISCUSSION

Let us consider the legitimacy of some of the assumptions made here. The main assumption is associated with the hypothesis of caustic crossing. Numerical calculations show that there are two effects capable of causing a significant increase in amplification. Apart from fold-caustic crossing, the source can also pass near the caustic beak. However, events of the second type for the images of Q2237 + 0305 are several times less probable than those of the first type (Wambsganss *et al.* 1992; Lewis and Irwin 1996) and, in general, are more symmetric. These two properties can serve as a statistical justification for using the hypothesis of caustic crossing.

A power-law model with a finite core radius is used to calculate the quasar size and structure. Three models of a caustic-crossing source are encountered in the literature: a homogeneous disk, a Gaussian source (Schneider and Weiss 1987), and a $(1 - r^2/R^2)^{1/2}$ distribution (Schneider and Wagoner 1987). All of them are completely determined by their radii. The $(1 + r^2/R^2)^{-p}$ model differs radically in that it is a two-parameter model. Estimating the rate of brightness decline p allows us to choose between different models for the quasar structure.

Allowance for the spatial orientation of the emitting region appreciably complicates the analysis. Two additional parameters associated with the orientation-angle components of the initial circular source appear. The first and second parameters determine, respectively, the apparent-ellipse eccentricity and the angle of motion with respect to the perpendicular to the caustic (in this case, allowance for the direction of motion does not reduce to a simple substitution of the transverse velocity). Besides, accretion-disk rotation can cause an additional asymmetry of the emitting region in the spectral range considered due to the Doppler effect.

In view of many influencing factors, the possibility of reconstructing, at least in principle, the one-dimensional quasar profile (along the x-axis) as the solution of an integral equation (Grieger *et al.* 1991; Mineshige and Yonehara 1999; Agol and Krolik 1999) seems of great interest. However, this is a separate, independent problem, which is yet to be applied to an actual monitoring.

The simple amplification behavior $\sim x^{-1/2}$ for a point source located in the caustic region is possible only

when several conditions are satisfied. The radius of caustic curvature must be considerably larger than the source size [see Fluke and Webster (1999) for curvature allowance]. The caustic must be isolated lest the source cover several caustics simultaneously. In addition, it is implied that there is no large-scale time gradient in amplification variations. Thus, for example, introducing a constant slope as an additional free parameter allows a model curve of image C to be easily fitted to the entire observing period 1997–2000. However, since there were no such large gradients throughout the entire 15-year-long monitoring history of Q2237 + 0305 and since their physical origin is not completely understood, we have to abandon the additional parameter.

Finally, the problem can be further complicated by intrinsic quasar variability. In general, the latter is rather difficult to separate from microlensing variability. However, given that the delays between the images in our cases do not exceed several days, intrinsic quasar variability must be repeated in all quasar images (with individual amplification factors) virtually simultaneously. The fact that the brightness variations in all four components are not synchronous provides circumstantial evidence that intrinsic quasar variability is negligible in this source.

Despite the possible complicating factors listed above, we have every reason to believe that the simple model used here is capable of faithfully reproducing the observational data, and that its implications deserve a careful analysis.

After this paper was mainly complete, Wyithe *et al.* (2000) independently published a preprint where they also interpreted the OGLE-group observations of Q2237 + 0305. These authors analyzed the light curves by using statistical methods based on conditional probability distributions.

Wyithe *et al.* (2000) focused mainly on computing the probability of occurrence of brightness bursts with observed parameters and on estimating the possibility of subsequent bursts. The conclusion that there is an additional overlooked brightness burst in image C associated with caustic crossing between the observing seasons of 1997 and 1998 seems to be of considerable interest. Such an event can account for the difficulties of modeling the light curve for image C in terms of the model with a single caustic crossing. Wiythe *et al.* (2000) also expect another caustic crossing in image C 500 days after the 1999 summer maximum (with a large uncertainty of ~100–2000 days, though).

The amplification in image A in late 1999 is interpreted as a caustic crossing in the negative direction, just as we did here. However, the peak of image C in mid-1999 is assumed to be caused by the passage of the source near the caustic beak. The choice between the two interpretations of the image C variability could be made by analyzing color variations of the source, which are much larger during caustic crossing than during beak passage. A color analysis could be performed by invoking additional data of the simultaneous monitorings at the Apache Point and Maidanak Observatories (Bliokh *et al.* 1999) through various filters during the same observing period.

ACKNOWLEDGMENTS

I wish to thank the OGLE group for organizing and carrying out the monitoring of Q2237 + 0305 and for providing access to the data before its publication.

REFERENCES

1. E. Agol and J. Krolik, Astrophys. J. **524**, 49 (1999).
2. R. D. Blandford and R. Narayan, Astrophys. J. **310**, 568 (1986).
3. P. V. Bliokh, V. N. Dudinov, V. G. Vakulik, *et al.*, Kinematika Fiz. Nebesnykh Tel **15**, 338 (1999).
4. K. Chang and S. Refsdal, Astron. Astrophys. **132**, 168 (1984).
5. R. T. Corrigan, M. J. Irwin, J. Arnaud, *et al.*, Astron. J. **102**, 34 (1991).
6. C. J. Fluke and R. L. Webster, Mon. Not. R. Astron. Soc. **302**, 68 (1999).
7. B. Grieger, R. Kayser, and T. Schramm, Astron. Astrophys. **252**, 508 (1991).
8. M. J. Irwin, R. L. Webster, P. C. Hewett, *et al.*, Astron. J. **98**, 1989 (1989).
9. G. F. Lewis and M. J. Irwin, Mon. Not. R. Astron. Soc. **283**, 225 (1996).
10. T. Manmoto, S. Mineshige, and M. Kusunose, Astrophys. J. **489**, 791 (1997).
11. S. Mineshige and A. Yonehara, Publ. Astron. Soc. Jpn. **51**, 497 (1999).
12. R. Østensen, S. Refsdal, R. Stabell, *et al.*, Astron. Astrophys. **309**, 59 (1996).
13. W. Press, S. Teukolsky, W. Vetterling, *et al.*, *Numerical Recipes in FORTRAN* (Cambridge Univ. Press, Cambridge, 1992, 2nd ed.), p. 675.
14. P. Schneider and R. V. Wagoner, Astrophys. J. **314**, 154 (1987).
15. P. Schneider and A. Weiss, Astron. Astrophys. **171**, 49 (1987).
16. N. I. Shakura and R. A. Sunyaev, Astron. Astrophys. **24**, 337 (1973).
17. J. Wambsganss, H. J. Witt, and P. Schneider, Astron. Astrophys. **258**, 591 (1992).
18. P. R. Wozniak, C. Alard, A. Udalski, *et al.*, Astrophys. J. **529**, 88 (2000).
19. J. S. B. Wyithe, E. L. Turner, and R. L. Webster, astro-ph/0001307 (2000).
20. J. S. B. Wyithe, R. L. Webster, and E. L. Turner, Mon. Not. R. Astron. Soc. **309**, 261 (1999).
21. A. F. Zakharov, *Gravitational Lenses and Microlenses* (Yanus, Moscow, 1997).
22. A. F. Zakharov and M. V. Sazhin, Usp. Fiz. Nauk **168**, 1041 (1998) [Phys. Usp. **41**, 945 (1998)].

Translated by A. Dambis

Astronomy Letters, Vol. 27, No. 3, 2001, pp. 156–162. Translated from Pis'ma v Astronomicheskiĭ Zhurnal, Vol. 27, No. 3, 2001, pp. 187–193.

Light Variations in the Candidate for Protoplanetary Objects HD 179821 = V1427 Aql in 1899–1999

V. P. Arkhipova*, N. P. Ikonnikova, R. I. Noskova, G. V. Sokol, and S. Yu. Shugarov

Sternberg Astronomical Institute, Universitetskiĭ pr. 13, Moscow, 119899 Russia

Received June 2, 2000

Abstract—We present photoelectric and photographic observations of the supergiant HD 179821 with a large infrared excess, a candidate for protoplanetary objects. Over, ten years of our *UBV* observations, the star exhibited semiregular light variations with amplitudes $\Delta V = 0\overset{m}{.}10$, $\Delta B = 0\overset{m}{.}15$, and $\Delta U = 0\overset{m}{.}25$, as well as systematic color and light variations. From 1990 until 1996, the yearly mean *U–B* and *B–V* color indices decreased by 0.25 and 0.15, respectively. After 1996, the motion of the star in the two-color (*B–V*)–(*U–B*) diagram upward and to the left slowed down. The color excess that we derived from our observations, by assuming that the star's spectral type was F3 I in the 1990s, is $E(B–V) = 1.0$. The photographic observations of HD 179821 from 1899 until 1989 show that its brightness m_{pg} generally increased while significantly fluctuating. An analysis of the observational data suggests that HD 179821 is most likely a post-AGB star of intermediate or low mass.

Key words: *observations of protoplanetary objects*

INTRODUCTION

HD 179821 (IRAS 19114+0002 = BD –0°3679 = AFGL 2343 = SAO 124414 = V1427 Aql = HIP 94496), a bright ($V \sim 8^m$) star of spectral type G5 (HD catalog) with Galactic coordinates $l = 35\overset{\circ}{.}6$ and $b = -5\overset{\circ}{.}0$, exhibits a large far-infrared excess. Based on its far-infrared fluxes, Pottasch and Parthasarathy (1988) and Hrivnak *et al.* (1989) classified the star as a candidate for protoplanetary objects. They attributed the infrared excess to a large-scale mass loss at the AGB evolutionary phase, which gave rise to an expanding dust envelope. The temperature of the dust envelope was estimated from IRAS data to be $T_d = 128$ K (Odenwald 1986).

HD 179821 exhibits several other properties characteristic of post-AGB objects. Thus, a complex Hα profile (Tamura and Takeuti 1991; Zacs *et al.* 1996; Reddy and Hrivnak 1999), suggesting mass outflow, is observed in many protoplanetary nebulae (for example, IRAS 18095+2704, SAO 163075, and HD 161796). The bipolar or axisymmetric structure of the HD 179821 envelope is one of the criteria for classifying the star as a protoplanetary object (Bujarrabal *et al.* 1992). The chemical composition of the stellar atmosphere—its enrichment with oxygen, nitrogen, and s-process elements (Zacs *et al.* 1996; Reddy and Hrivnak 1999), also argues for the assumed post-AGB status of HD 179821.

However, the expansion velocity of the CO envelope found by Zuckerman and Dyck (1986), $V_{exp} = 34$ km s^{-1}, is appreciably higher than 10–15 km s^{-1}, which is typical of low- and intermediate-mass post-AGB stars. Besides, the unusually-intense absorption lines of the O I λ7774 Å triplet and the distance derived from the interstellar components of the Na I D_1 and D_2 lines (Reddy and Hrivnak 1999) strongly suggest that the star may be a high-luminosity ($M_V \approx -8\overset{m}{.}9 \pm 1\overset{m}{.}0$) object and, thus, a massive supergiant. Kastner and Weintraub (1995) compared HD 179821 with the massive hypergiant IRC+10420, one of the brightest far-infrared sources. There is currently no consensus on the evolutionary status of HD 179821.

UBV OBSERVATIONS OF HD 179821 = V1427 Aql

We included HD 179821 in our program of searching for and studying the optical variability of stars with infrared excesses, which are considered as candidates for protoplanetary objects, in 1990. Our two-year-long observations revealed its photometric variability (Arkhipova *et al.* 1993). In the variable star catalog, the object was designated V1427 Aql (Kazarovets and Samus 1997) and was classed with SRd variables. Our subsequent observations confirm the conclusion that the object is variable.

Our observations were carried out in a system close to Johnson's standard system at the Crimean Station of the Sternberg Astronomical Institute (SAI) using the

* E-mail address for contacts: vera@sai.msu.ru

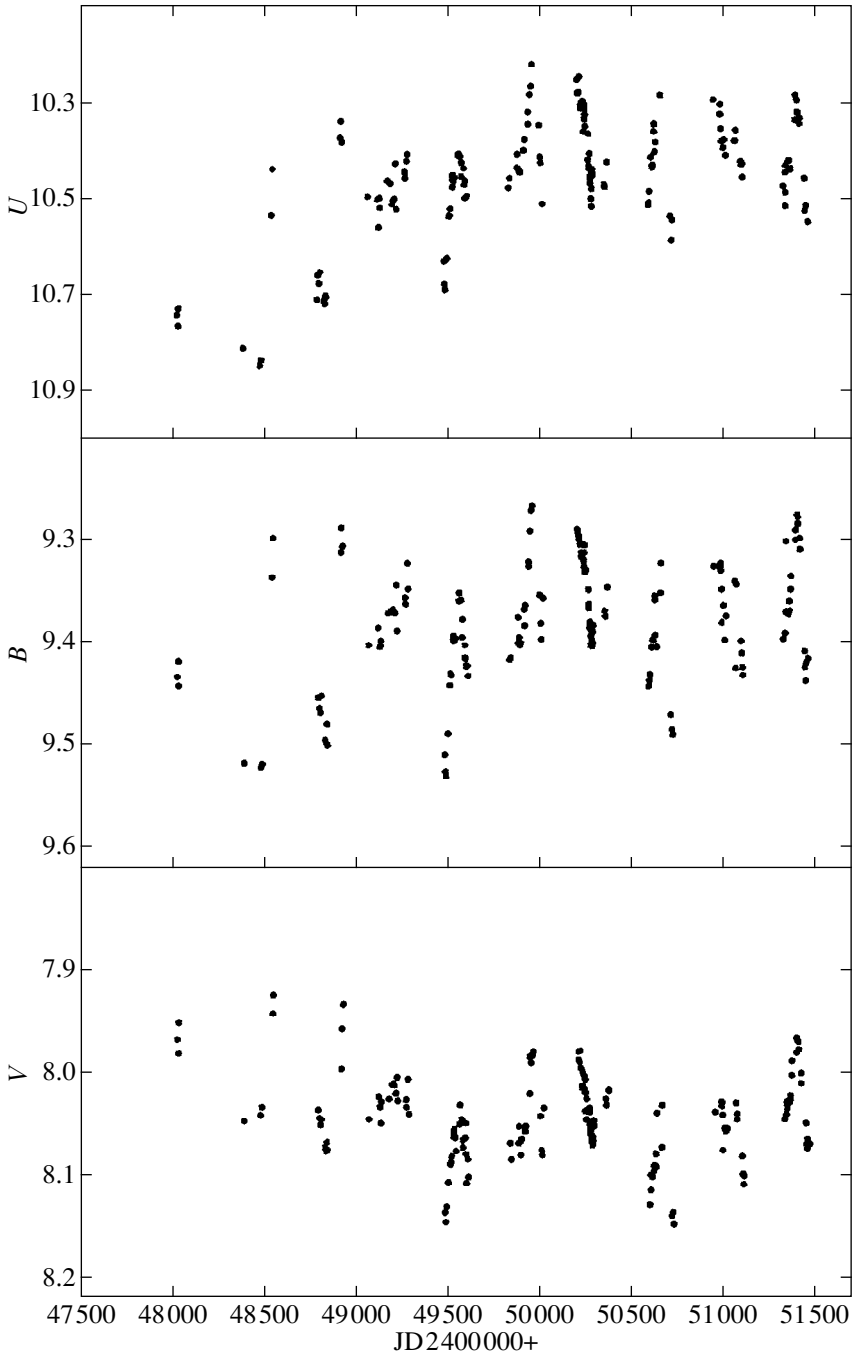

Fig. 1. *UBV* light curves of HD 179821 in 1990–1999.

60-cm reflector with a *UBV* photometer. As before (Arkhipova *et al.* 1993), the comparison star was SAO 124412. Table 1[1] gives our ten-year-long observations, including those published previously (Arkhipova *et al.* 1993), but reduced to Johnson's system with different reduction equations. The accuracy of our measurements was $\pm 0^m.005$.

[1] Table 1 is published in electronic form only and is accessible via ftp cdsarc.u-strasbg.fr/pub/cats/J (130.79.128.5) or http://cdsweb.u-strasbg.fr/pub/cats/J.

Figure 1 shows, *UBV* light curves of HD 179821 for 1990–1999. As we see from the figure, the star underwent semiregular light variations. Their amplitudes were $\Delta V = 0^m.10$, $\Delta B = 0^m.15$ and $\Delta U = 0^m.25$. During the light variations, a clear correlation shows up in the color-magnitude diagram (Fig. 2): the star becomes bluer as it brightens, which is characteristic of pulsations. The mean brightness also clearly exhibits a systematic trend. Having subtracted the seasonal mean from the original series, we searched for periodicities in

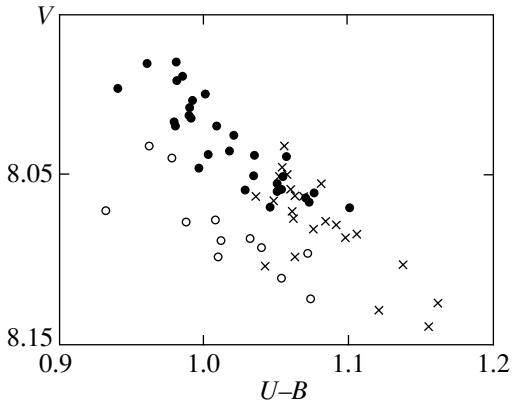

Fig. 2. Behavior of HD 179821 in the color-magnitude ($U-B$) V diagram. The 1994, 1996, and 1997 observations are represented by crosses, filled circles, and open circles, respectively.

the B light variations in the interval JD 2449484–2451470 by the Fourier-transform method using the code developed by Yu.K. Kolpakov at SAI.

Three extrema corresponding to periods $P_1 = 205^d \pm 2^d$, $P_2 = 132\overset{d}{.}5 \pm 1\overset{d}{.}5$, and $P_3 = 433^d \pm 2^d$ are distinguished in the power spectrum. Since P_2 and P_3 are one-year aliases of P_1, we chose P_1 as the principal period, though its significance is low and its value exceeds the mean duration of the observing seasons for V1427 Aql ($\Delta T = 157 \pm 28$ days). After subtracting the mean curve with P_1, we found yet another period, $P_4 = 142 \pm 2$ days. Their frequency ratio is $\nu_1/\nu_4 \approx 0.7$, which corresponds to the ratio of the first overtone to the fundamental tone. Thus, we assume that pulsations, probably in two modes, are mainly responsible for the variability of V1427 Aql in the ten-year interval. The star is apparently outside the instability strip; therefore, it would be unreasonable to expect strict periodicity in its light variations.

Since the pulsation periods are comparable to the duration of the observing seasons for V1427 Aql, averaging the observations within each season makes it possible to trace the star's behavior outside pulsations. Figure 3 shows yearly mean color and V light curves for HD 179821. A two-color diagram of the averaged observations is presented in Fig. 4. From 1990 until 1996, the $U-B$ and $B-V$ color indices monotonically decreased: the star became bluer and moved, in the two-color diagram upward, and to the left. After 1996, this motion in the ($B-V$)–($U-B$) diagram slowed down, while the 1998–1999 observations already show a tendency for the star to redden. In the two-color diagram,

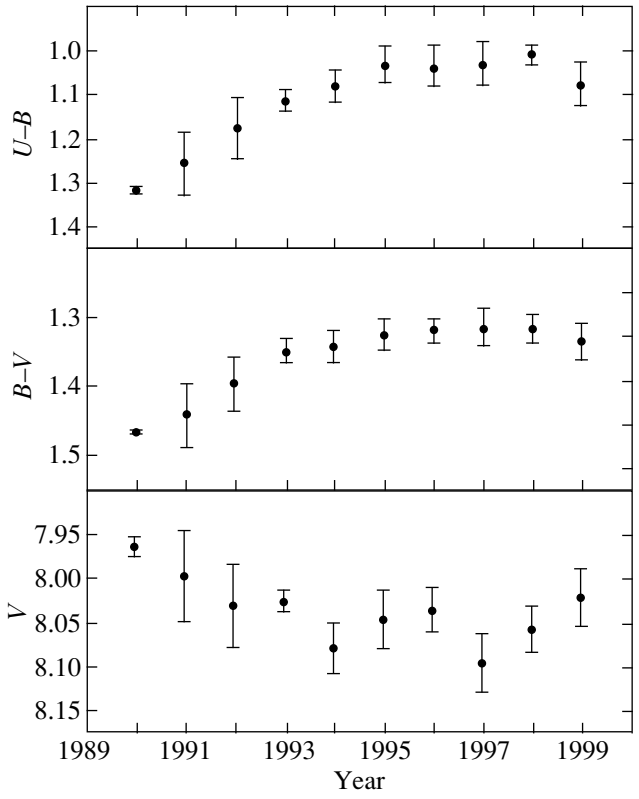

Fig. 3. Yearly mean ($B-V$) and ($U-B$) color indices and V magnitudes of HD 179821 in 1990–1999.

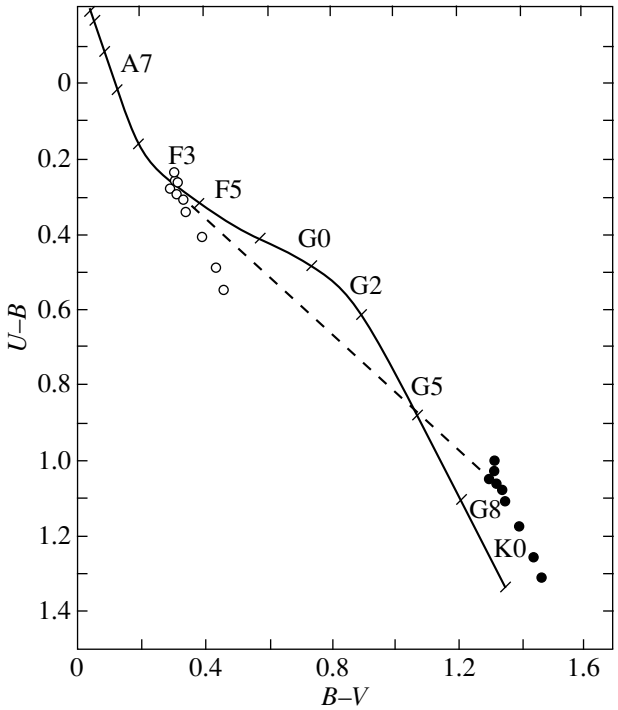

Fig. 4. Two-color diagram for the yearly mean observations of HD 179821. Filled circles are the observed color indices of HD 179821; solid line represents the normal colors of supergiants, as inferred by Straizys (1977); dashed line represents the interstellar reddening line for the law of Whitford (1958); and open circles are the color indices of HD 179821 corrected for a reddening with $E(B-V) = 1.0$.

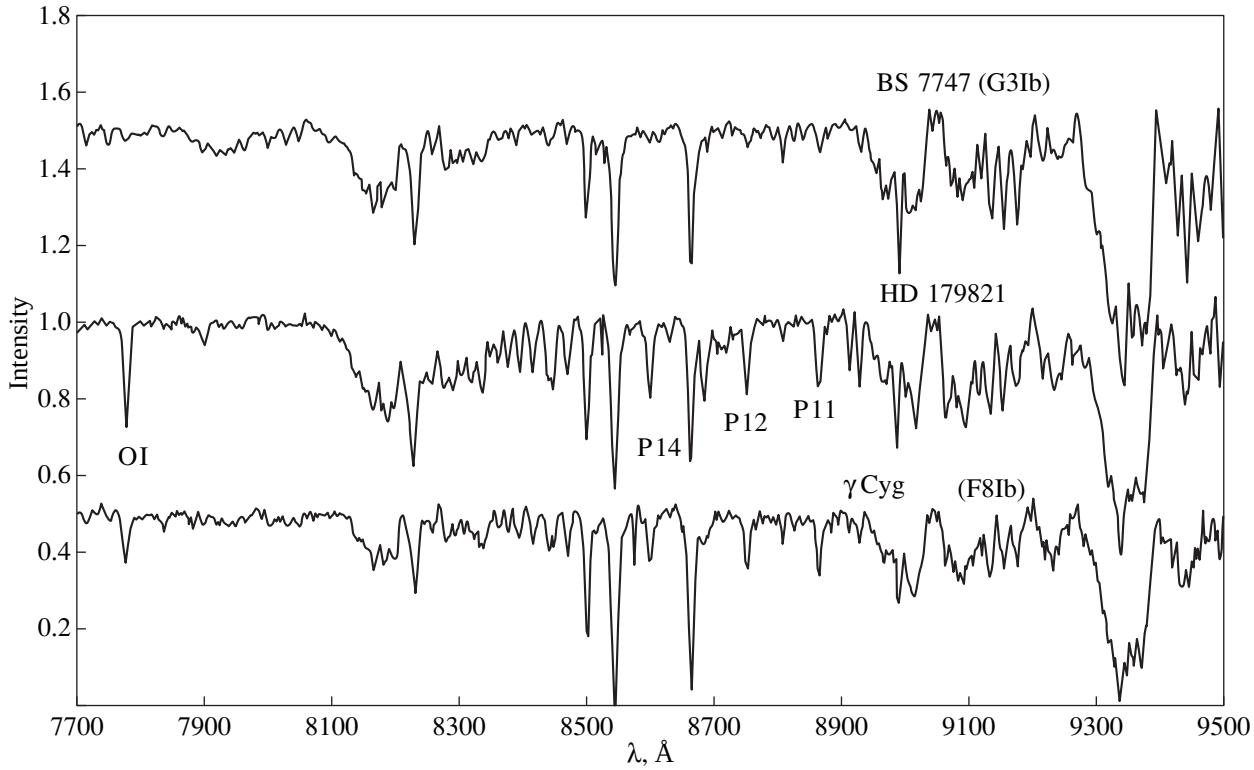

Fig. 5. Continuum-normalized spectra of HD 179821, BS 7747, and γCyg taken on September 20, 1999. The Paschen P11, P12, and P14 lines and the O I λ7774 Å triplet are marked.

the reddening line for HD 179821 crosses the normal color line for supergiants at two points, and we must know the star's spectral type to determine its color excess.

The spectral classification of HD 179821 from the HD epoch until the 1980s [G5: HD catalog; G Ia: Bidelman (1981); G4 0-Ia: Keenan (1983); ~G5Ia: Hrivnak *et al.* (1989)], which is based on low-resolution spectra, led to a G supergiant. However, having analyzed the high-resolution spectrum taken in 1992, Zacs *et al.* (1996) found $T_{\rm eff}$ = 6800 K. Studying the star's echelle spectrum in 1997, Reddy and Hrivnak (1999) found $T_{\rm eff}$ = 6750 K. These effective temperatures correspond to an F star rather than a G star. Reddy and Hrivnak (1999) believe that the systematic discrepancy between the spectral classification based on low-resolution spectra and $T_{\rm eff}$ determined by analyzing spectral lines in high-resolution spectra can be explained, in part, by the hydrogen emission, which is clearly seen above the continuum in Hα. As a result, the Balmer hydrogen lines are weakened, and the ratios based on them, such as Fe, CH λ4325/Hγ and Fe λ4143/Hδ, imply a cooler star.

We used our observations to determine the spectral type of HD 179821. On September 20, 1999, we obtained spectra for HD 179821 and the comparison stars BS 7747 (G3 Ib) and γCyg (F8 Ib) in the wavelength range 4000–9500 Å using a fast spectrograph of the 125-cm telescope equipped with a CCD camera (resolution 5.2 Å per pixel) at the Crimean Station of SAI. Since the detector sensitivity was low in the blue spectral range, we could not use the line ratios that are commonly applied for spectral classification. Figure 5 shows the 7500–9500 Å spectra of HD 179821 and the comparison stars. Noteworthy are the intense Paschen hydrogen lines in the spectrum of HD 179821; they are comparable in intensity to the hydrogen lines in the spectrum of γCyg (F8 Ib) and are considerably stronger than the lines in the spectrum of BS 7747 (G3 Ib). These results and the star's temperature determined by Zacs *et al.* (1996) and Reddy and Hrivnak (1999) lead us to conclude that HD 179821 was an F star in the 1990s.

The temperature of 6750–6800 K deduced from high-resolution spectroscopic data (Zacs *et al.* 1996; Reddy and Hrivnak 1999) corresponds, on the scale of Flower (1996), to the normal color index $(B–V)_0$ = 0.30 of a supergiant and, according to Straizys (1977), to the spectral type F3 I. The color excess is then $E(B–V)$ = 1.0. Estimation of the interstellar reddening from neighboring stars within 1°.5 of HD 179821 yields an upper limit $E_1(B–V)$ = 0.4. Only the star SAO 124421 with $E(B–V) \approx$ 0.8 constitutes an exception. The additional reddening of $E_{\rm d}(B–V) \approx 0.6$ is most likely produced by the circumstellar dust envelope around HD 179821.

The star's color variations from 1990 until 1999 cannot be explained by monotonic changes in tempera-

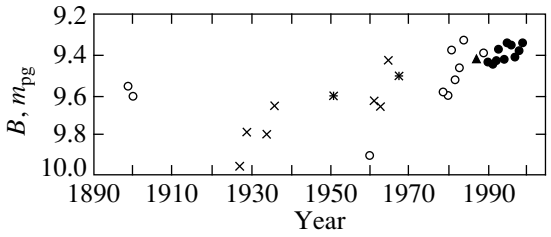

Fig. 6. The photographic light curve of HD 179821 [open circles are our measurements on plates from the SAI collection; crosses are our measurements on plates from the Sonneberg collection; and asterisks are m_{pg} estimated on the Palomar O print and the print from the atlas of Vehrenberg (1970)]. Also plotted are the yearly mean photoelectric *B* magnitudes (filled circles) and the *B* magnitude estimate from Hrivnak *et al.* (1987) (triangle).

ture, but we can assume both the influence of a variable stellar wind and variations of the circumstellar reddening in the dust envelope around the star due to its expansion and inhomogeneity.

THE PHOTOMETRIC HISTORY OF HD 179821

Given the star's current unusual light variations, it would be of interest to trace the photometric history of HD 179821 in the past. To this end, we used materials of the SAI Sky Service, plates of the Sonneberg Observatory photograph collection, and available sky atlases. Our measurements averaged over each year ($\bar{m}_{pg}$). The number of plates (*N*) and rms deviations (σ_N) are given in Table 2. On the Palomar Observatory Sky Survey O print for August 23–24, 1951, we estimated m_{pg} of the star to be $9^m.6$. On the print from the atlas of Vehrenberg (1970), the star is slightly brighter. We estimated its photographic magnitude to have been $9^m.5$ on July 28–29, 1968.

Table 2. Photographic observations of HD 179821

Year	$\bar{m}_{pg}$	*N*	σ_N
1899	9.55	2	0.00
1900	9.60	2	0.00
1927	9.95	2	0.02
1929	9.78	11	0.11
1934	9.79	2	0.03
1936	9.65	3	0.10
1960	9.94	6	0.06
1961	9.62	11	0.10
1963	9.65	15	0.09
1965	9.42	18	0.11
1979	9.58	7	0.08
1980	9.60	19	0.08
1981	9.37	11	0.10
1982	9.52	13	0.07
1983	9.46	9	0.06
1984	9.32	4	0.03
1989	9.39	10	0.10

Figure 6 shows the star's light curve constructed from its measurements on plates and in the above atlases. We also plotted our photoelectric *B* magnitudes of HD 179821 averaged over each observing season from 1990 until 1999 and the *B* magnitude estimated by Hrivnak *et al.* (1989) on September 4, 1987. We do not reduce all measurements to the same system, because the errors of photographic observations ($\sim 0^m.1$) are several times larger than the difference between the photometric systems. The photographic observations of HD 179821 from 1899 until 1989 show that its brightness m_{pg} generally increased while significantly fluctuating. Noteworthy is the low brightness of the star in 1927 and 1960, when $m_{pg} \sim 10^m$.

We now turn to the visual brightness. At the HD epoch, the star had $m_{ptm} = 8^m.38$ and the spectral type G5. Applying the bolometric correction BC = –0.32 (Flower 1996), we then obtain the apparent bolometric magnitude $m_{bol} = 8^m.06$. Currently, the mean brightness is $V \approx 8^m.0$, and assuming the spectral type F3 I, for which BC = 0.02, we find $m_{bol} = 8^m.02$. Within uncertainties in the bolometric corrections and given that the star undergoes semiregular light variations with an amplitude of $\sim 0^m.1$ in *V*, it could be assumed that the *V* brightness trend from the HD epoch until the 1990s is attributable to the star's evolution at a constant bolometric luminosity.

However, the 100-year-long photographic observations are in conflict with this evolutionary track. Assuming the color excess $E(B–V) = 1.0$ and the spectral type G5, the star would have $B = m_{ptm} + (B–V)_0 + E(B–V) = 8.38 + 1.08 + 1.00 = 10^m.46$ at the beginning of this century, whereas the photographic observations of HD 179821 do not give magnitudes fainter than 10^m. This large difference cannot be explained by the measurement errors and the star's photometric variability alone.

EXTINCTION IN THE CIRCUMSTELLAR DUST ENVELOPE OF HD 179821

We made an attempt to study the extinction law in the circumstellar dust envelope of HD 179821 by using the red and near-infrared photometric data obtained by other authors (Hrivnak *et al.* 1989; Yudin *et al.* 2000). Firstly, all color indices of the star expressed as $V–\lambda$, where λ refers to the *RIJHKL* bands, or as $\lambda–V$, if the *B* and *U* bands are used, were corrected for the interstellar reddening, for which we found above $E_1(B–V) = 0.4$, with the standard reddening curve from Whitford (1958).

Subsequently, assuming that the star's spectral type in the 1990s was F3 I and using multicolor photometry for F3 I, we plotted the circumstellar color excesses $E_d(V-\lambda) = (V-\lambda) - E_1(V-\lambda) - (V-\lambda)_0$ against λ^{-1} and then compared the plots with a normal reddening law normalized to the circumstellar color excess $E_d(B–V)$ of HD 179821. While the dependence of E on λ at optical wavelengths is essentially the same, the near-infrared circumstellar extinction is higher than that given by the law of Whitford (1958). This may imply that the dust envelope contains larger particles than those in the ordinary interstellar medium and particles with a different chemical composition.

DISCUSSION

Our photometric observations of HD 179821 in 1990–1999 revealed two types of its variability. First, it exhibits semiregular light variations attributable to pulsations. A periodicity analysis revealed two frequencies of moderately high significance, but their ratio of 0.7 allow them to be considered as real. Bimodal pulsations appear to be characteristic of yellow supergiants, candidates for protoplanetary objects (Arkhipova *et al.* 2000); therefore, the detection of a possible double periodicity in HD 179821 argues that the star should belong to this type of objects.

Second, during our observations, HD 179821 showed a trend in brightness and colors. The part of this trend observed in 1990–1996, when the star's color indices systematically decreased, is probably attributable to a rise in its temperature, which was caused, for example, by a change in stellar-wind activity. The possibility of a temporal decrease in reddening in the circumstellar dust envelope cannot be ruled out either, although we have to assume an abnormal reddening law. The color variations may also be cyclic. Whether the star is binary is still an open question. In any case, the light and color variations in HD 179821 over the past ten years are apparently not directly related to the star's evolution.

By contrast, the detected variations in the star's visual brightness over approximately 100 years are in agreement with the idea that the star is a rapidly evolving post-AGB supergiant. The difference between its spectral types at the HD epoch and at present, if real, lends strong support to the hypothesis of an evolving post-AGB star. Here, we showed that the apparent bolometric magnitude, derived from visual observations, was essentially constant, at least since the HD epoch. However, the 100-year-long photographic observations are in conflict with the evolutionary track. The conflict can be removed by assuming that the HD spectral type is in error for the reasons given by Reddy and Hrivnak (1999). The question of the star's evolution should then be considered closed.

The photometric data allowed us to estimate the star's color excess. It was found to be fairly large, $E(B-V) = 1.0$, compared to the maximum interstellar color excess (0.4) estimated in the direction of the Galaxy under consideration. Thus, we conclude that the role of circumstellar extinction HD 179821 is significant. Reddy and Hrivnak (1999) have already reported on the large absorption ($A_V \approx 4^m$) inferred from spectroscopic and photometric observations. The complex, multicomponent structure of the D_1, D_2 Na I absorption lines in the spectrum of HD 179821 (see Reddy and Hrivnak 1999) should also be mentioned in this connection. The authors interpreted the components at radial velocities of –10, +11, and +48 km s^{-1} as interstellar and the remaining components, at +68 and +103 km s^{-1}, as belonging to the star and its envelope. In our view, the large half-width of the component at V_r = +48 km s^{-1}, similar to that of the stellar components, most likely suggests that it belongs to the HD 179821 system. A significant fraction of the total Na I absorption then belongs to the star and to its envelope, which confirms a large intrinsic absorption. Intense Na I absorption lines are observed in the circumstellar envelopes of many post-AGB stars, for example, in V4334 Sgr (Arkhipova *et al.* 1999), FG Sge (Kipper *et al.* 1995), as well as in the hotter stars V886 Her (Arkhipova *et al.* 2001) and V1853 Cyg (Smith and Lambert 1994).

The above arguments support the hypothesis that HD 179821 is most likely an intermediate- or low-mass post-AGB supergiant rather than a massive star, as assumed by some authors (Kastner and Weintraub 1995; Hawkins *et al.* 1995; Jura and Werner 1999). Their conclusions are based on the star's high luminosity estimated from the intense O I λ7774 Å triplet lines and from the distance inferred from the radial velocities of the components of interstellar Na I lines and DIBs. An abundance analysis for HD 179821 (Zacs *et al.* 1996; Reddy and Hrivnak 1999) shows that the star's relative atmospheric oxygen abundance is 0.5 dex higher than that of normal F supergiants, which are used to calibrate the relation between O I line intensities and luminosity. The abundances of CNO and s-process elements in HD 179821 are similar to those in a typical representative of post-AGB stars. As for the distance determined from the interstellar lines, the interpretation of Na I components (and probably DIBs as well) seems to be open to debate. Besides, the method itself cannot be reliable enough to determine the object's luminosity.

ACKNOWLEDGMENTS

We wish to thank V.F. Esipov for the spectroscopic data, P. Kroll, who provided plates from the Sonneberg Observatory archive, and V.M. Lyuty for the valuable remarks. This study was supported, in part, by the Russian Foundation for Basic Research (project no. 00-15-96533).

REFERENCES

1. V. P. Arkhipova, N. P. Ikonnikova, and R. I. Noskova, Pis'ma Astron. Zh. **19**, 436 (1993) [Astron. Lett. **19**, 169 (1993)].
2. V. P. Arkhipova, N. P. Ikonnikova, R. I. Noskova, and G. V. Sokol, Pis'ma Astron. Zh. **26**, 705 (2000) [Astron. Lett. **26**, 609 (2000)].
3. V. P. Arkhipova, V. G. Klochkova, and G. V. Sokol, Pis'ma Astron. Zh. **27**, 1 (2001) [Astron. Lett. **27** (2001) (in press)].
4. V. P. Arkhipova, R. I. Noskova, V. F. Esipov, and G. V. Sokol, Pis'ma Astron. Zh. **25**, 711 (1999) [Astron. Lett. **25**, 615 (1999)].
5. W. P. Bidelman, Astron. J. **86**, 553 (1981).
6. V. Bujarrabal, J. Alcolea, and P. Planesas, Astron. Astrophys. **257**, 701 (1992).
7. P. J. Flower, Astrophys. J. **469**, 355 (1996).
8. G. W. Hawkins, C. J. Skinner, M. M. Meixner, *et al.*, Astrophys. J. **452**, 314 (1995).
9. B. J. Hrivnak, S. Kwok, and K. M. Volk, Astrophys. J. **346**, 265 (1989).
10. M. Jura and M. W. Werner, Astrophys. J. **525**, L113 (1999).
11. J. H. Kastner and D. A. Weintraub, Astrophys. J. **452**, 833 (1995).
12. E. V. Kazarovets and N. N. Samus, Inf. Bull. Var. Stars, No. 4471, 1 (1997).
13. P. C. Keenan, Bull. Inf. Centre Donnees Stellaires, No. 24, 19 (1983).
14. T. Kipper, M. Kipper, and V. G. Klochkova, Astron. Astrophys. **297**, L33 (1995).
15. S. F. Odenwald, Astrophys. J. **307**, 711 (1986).
16. S. R. Pottasch and M. Parthasarathy, Astron. Astrophys. **192**, 182 (1988).
17. B. E. Reddy and B. J. Hrivnak, Astron. J. **117**, 1834 (1999).
18. V. V. Smith and D. L. Lambert, Astrophys. J. Lett. **424**, L123 (1994).
19. V. Straĭzhis, *Multicolor Photometry of Stars* (Mokslas, Vilnius, 1977).
20. S. Tamura and M. Takeuti, Inf. Bull. Var. Stars, No. 3561, 1 (1991).
21. H. Vehrenberg, *Atlas Stellarum* (Treugesell.-Verlag, Düsseldorf, 1970).
22. A. E. Whitford, Astron. J. **63**, 201 (1958).
23. B. F. Yudin *et al.*, private communication (2000).
24. L. Zacs, V. G. Klochkova, V. E. Panchuk, and R. Spelmanis, Mon. Not. R. Astron. Soc. **282**, 1171 (1996).
25. B. Zuckerman and H. M. Dyck, Astrophys. J. **311**, 345 (1986).

Translated by N. Samus'

Astronomy Letters, Vol. 27, No. 3, 2001, pp. 163–170. Translated from Pis'ma v Astronomicheskiĭ Zhurnal, Vol. 27, No. 3, 2001, pp. 194–202.

Expulsion of Magnetic Flux from the Core and Its Dissipation in the Crust of a Neutron Star

D. Yu. Konenkov[1]* and U. Geppert[2]

[1] *Ioffe Physicotechnical Institute, ul. Politekhnicheskaya 26, St. Petersburg, 194021 Russia*
[2] *Potsdam Astrophysical Institute, Potsdam, Germany*

Received March 13, 2000

Abstract—We construct a model for the magnetic-field evolution of an isolated neutron star by assuming that its core is a type II superconductor and that the field penetrates the core in the form of magnetic lines (fluxoids). We consider the fluxoid expulsion from the core and the field dissipation in a conducting crust. The magnetic-field evolution is calculated self-consistently by taking into account the inverse effect of crustal magnetic line bending on the fluxoid velocity in the core. We consider the evolution of two magnetic configurations, in which the bulk of the magnetic flux passes through the neutron-star core and crust. The buoyancy of fluxoids and the force from the neutron vortexes are mainly responsible for their expulsion from the core in the former and latter cases, respectively. © *2001 MAIK "Nauka/Interperiodica".*

Key words: *pulsars, neutron stars, magnetic-field evolution*

INTRODUCTION

The magnetic-field evolution of neutron stars (NSs) has been the subject of much debate since the discovery of radio pulsars. It is primarily determined by the configuration of currents inside NSs and by the conductive properties of the layers, in which these currents are located. The magnetic-flux conservation during gravitational collapse and/or the effect of magnetic dynamo in a convective proto-neutron star (Thompson and Duncan 1993) result in a uniform distribution of the magnetic flux over the NS and in the passage of its bulk through the core. On the other hand, a magnetic field can be generated in the outer-crustal layers of a young NS after its birth under the effect of, for example, thermomagnetic instability (Urpin *et al.* 1986). In this case, the bulk of the magnetic flux is confined to the NS crust (see Fig. 1). Unfortunately, there is currently no consensus on the generation mechanism of NS magnetic fields.

Neutrons and protons in the NS core are believed to become superfluid at early cooling stages (Alpar 1991); the superfluid core of the NS is involved in its rotation, forming a lattice of neutron vortexes (see, e.g., Shapiro and Teukolsky 1983). The neutron vortexes are parallel to the spin axis. As was shown by Baym *et al.* (1969), protons form a type II superconductor, in which the magnetic field exists in the form of vortex lines, or fluxoids (Lifshitz and Pitaevskiĭ 1978). Each fluxoid carries a quantum of magnetic flux $\Phi_0 = hc/2e \approx 2 \times 10^7$ G cm^2. A fluxoid consists of a nonsuperconducting nucleus, with a characteristic diameter of the order of the proton coherence length ξ_p, surrounded by the shielding current of superconducting protons with sizes of the order of the London length of magnetic-field penetration into a superconductor, $\lambda_p \sim 10^{-12}$ cm. In a type II superconductor, $\xi_p/\lambda_p \le 1/\sqrt{2}$. The magnetic field is $B_p = \Phi_0/(4\pi\lambda_p^2)\ln(\lambda_p/\xi_p) \approx 1.9 \times 10^{16} x_p \rho_{15} \ln(\lambda_p/\xi_p)$ G inside the fluxoid and falls off exponentially outside the fluxoid, with a characteristic length λ_p (Ding *et al.* 1993). Here, x_p is the proton-to-neutron density ratio in the core, and ρ_{15} is the density in units of 10^{15} g cm^{-3}. By the mean core magnetic field, we mean $B_c = \Phi_0 n_p$, where $n_p = 5 \times 10^{18}(B_c/10^{12}\ \text{G})$ cm^{-2}, is the number of fluxoids per unit area.

The magnetic-field evolution in the core is directly related to the motion of the fluxoids. The buoyancy force (Muslimov and Tsygan 1985a, 1985b), the force from neutron vortexes (Ding *et al.* 1993), and the drag force (Harvey *et al.* 1985) act on the fluxoids. The radial fluxoid velocity (and the magnetic-field evolution) in the core of an isolated NS under the action of these forces was first calculated by Ding *et al.* (1993). Jahan-Miri (1999) used the same model to calculate the magnetic evolution of NSs in binary systems. These authors determined the fluxoid velocity and the magnetic-field evolution in the core from the balance condition for the forces exerted on fluxoids. The surface field relaxed to the core field in the dissipation time of the crustal currents, which is a parameter of the problem. However, as the fluxoid roots move, the crustal magnetic lines bend, the magnetic energy outside the

* E-mail address for contacts: dyk@astro.ioffe.ru; D.Konenkov@aip.de

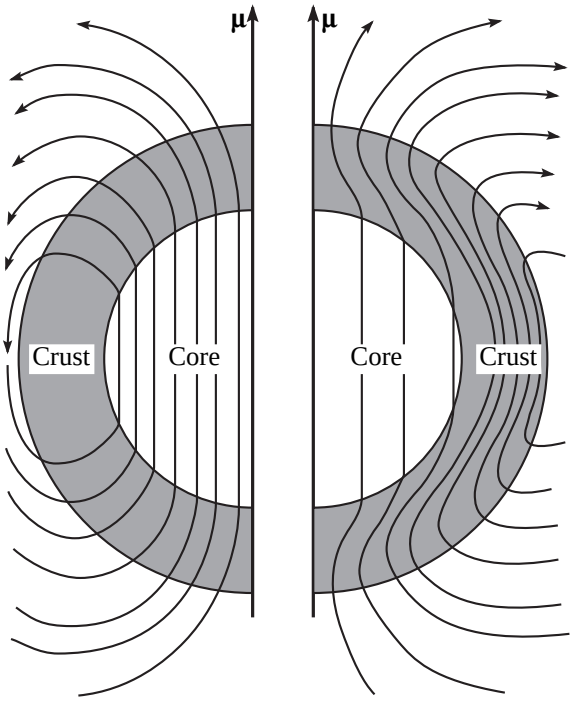

Fig. 1. Two possible configurations of the NS poloidal magnetic field. On the left, the bulk of the magnetic flux passes through the NS core; if the core is a type II superconductor, then the magnetic field penetrates it in the form of fluxoids. On the right, the bulk of the magnetic flux passes through the NS crust.

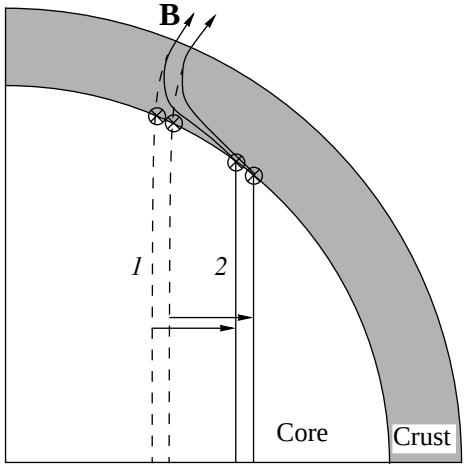

Fig. 2. Motion of fluxoids from position *1* to position *2*. The fluxoid roots are marked by ⊗.

core changes, and currents are generated in the crust. Consequently, additional work needs to be done to move the fluxoid root (Fig. 2). This factor was disregarded by Ding *et al.* (1993) and Jahan-Miri (1999). Here, we calculate the expulsion of magnetic flux from the NS core, in a self-consistent way, by taking into account this effect. We consider the evolution of the two possible magnetic configurations shown in Fig. 1.

STATEMENT OF THE PROBLEM

Alpar *et al.* (1984) showed that a magnetic field comparable in magnitude to the magnetic field inside a fluxoid is generated inside neutron vortexes. As a result, fluxoids and neutron vortexes interact with each other as they draw closer together, with the interaction energy being $E_p \sim 10$ MeV per intersection. The radial velocity of neutron vortexes is determined by the spindown rate of an isolated NS; in turn, spindown is attributable to the losses of rotational kinetic energy of an isolated NS through the magnetodipole radiation and the ejection of relativistic particles:

$$v_n(t) = \frac{rk(t)\Omega_s}{2}, \quad (1)$$

where

$$k(t) = K\frac{8B_e^2(t)R^6}{3Ic^3}.$$

Here, r is the radial coordinate, Ω_s is the angular velocity of the superfluid NS core, R is the NR radius, I is the moment of inertia, B_e is the NS surface magnetic field on the magnetic equator, and c is the speed of light. In general, the coefficient $K \le 1$ depends on the inclination of the spin axis to the magnetic axis, on the spin period, and on the magnetic field. For simplicity, we assume that $K = 1$. We emphasize that Ω_s is not equal to the observed angular velocity Ω_c of the crust. There are three modes of relative motion of fluxoids and neutron vortexes: fluxoids can move either faster than neutron vortexes (forward creeping), or the velocities of both types of vortex lines can be the same (comoving), or neutron vortexes can move faster than fluxoids (reverse creeping). The force exerted per unit fluxoid length by neutron vortexes is given by (Ding *et al.* 1993)

$$f_n = \frac{n_v}{n_p}F_M \approx \frac{2\Phi_0\rho r\Omega_s(t)\omega(t)}{B_c(t)}, \quad (2)$$

where n_v is the number of neutron vortexes per unit area, $F_M = \rho\kappa r\omega$ is the Magnus force per unit vortex length, ρ is the core matter density, $\kappa = h/2m_n$ is the velocity circulation quantum, and $\omega = \Omega_s - \Omega_c$ is the difference between the angular velocities of a superfluid core and a conducting solid crust. Depending on the sign of ω, the force from neutron vortexes can be positive (directed to the crust, i.e., expels a fluxoid outward) or negative (directed into the NS, i.e., prevents fluxoid expulsion).

The maximum magnitude of the force exerted by a neutron vortex on a fluxoid per intersection can be estimated by using the formula $f_p \approx E_p/\lambda_p$. The Magnus force acting on neutron vortexes is balanced by the force from fluxoids. It thus follows that $|\omega| \le \omega_{cr}$ (Ding *et al.* 1993; Jahan-Miri 1999). In the forward creeping, comoving, and reverse creeping modes, $\omega = \omega_{cr}$, $|\omega| <$

ω_{cr}, and $\omega = -\omega_{cr}$, respectively. Ding *et al.* (1993) derived the following expression for ω_{cr}:

$$\omega_{cr} = 8.7\times10^{-2}x_p\alpha_g r_6^{-1}\left(\frac{\delta m_p^*}{m_p}\right)\left(\frac{m_p^*}{m_p}\right)^{-1/2}$$
$$\times(B_c/10^{12}\ \mathrm{G})^{1/2}\ln(\lambda_p/\xi_p)\sin(2\chi)\ \mathrm{rad\ s^{-1}}.$$

Here, α_g is a geometric factor of the order of unity, r_6 is the distance from the neutron vortex to the spin axis (in units of 10^6 cm), m_p^* is the effective proton mass, $\delta m_p^* = m_p - m_p^*$, and χ is the angle between the spin axis and the magnetic dipole axis. In our calculations, we assume that $x_p = 0.025$, $m_p^* = 0.8m_p$, $\lambda_p/\xi_p = 1/\sqrt{2}$, and $\sin(2\chi) = 1$.

Apart from the force of neutron vortexes, the buoyancy force acts per unit fluxoid length (Muslimov and Tsygan 1985a, 1985b):

$$f_b = \left(\frac{\Phi_0}{4\pi\lambda_p}\right)^2\frac{1}{R_c}\ln\left(\frac{\lambda_p}{\xi_p}\right), \quad (3)$$

where R_c is the core radius. This force is always positive, i.e., it tends to expel a fluxoid from the core.

Finally, the drag force attributable to electron scattering by the fluxoid magnetic field acts per unit length of a fluxoid moving at velocity v_p. This force is proportional to the fluxoid velocity and is given by (Harvey *et al.* 1985)

$$f_v = -\frac{3\pi}{64}\frac{n_e e^2\Phi_0^2}{E_F\lambda_p}\frac{v_p}{c}, \quad (4)$$

where n_e is the electron density in the core (we assume it to be equal to the proton density), and E_F is the electron Fermi energy. This equation for the drag force remains valid when the collective effects during fluxoid motion are ignored, which is justifiable for $B_c \ll B_p$.

According to Ding *et al.* (1993), the equation for the fluxoid velocity can be written as

$$f_n + f_b + f_v(v_p) = 0. \quad (5)$$

These authors also attempted to take into account the force that arises as fluxoids bend. Allowance for these forces gave rise to a coefficient of the order of unity near f_b in Eq. (5). On the other hand, Eq. (33) from Ding *et al.* (1993), which relates the field evolution in the core to the fluxoid velocity, explicitly implies that the core field is uniform (i.e., the fluxoids are straight, and their density is constant throughout the entire core). We assume, for simplicity, that the fluxoids remain straight as they move. Whether this simplification is acceptable is discussed below. The magnetic field concentrated in the core of the fluxoids also passes through the nonconducting crust. The crustal-magnetic lines, bend as the fluxoid roots move (Fig. 2); consequently, the forces exerted on a fluxoid do work as the fluxoid root moves, which was not included in Eq. (5). A more consistent allowance for this effect requires that Eq. (5) be replaced by

$$\sum_{\text{fluxoids}}\int(\mathbf{f}_n + \mathbf{f}_b + \mathbf{f}_v)\mathbf{v}_p dl = \int_{V_{crust}}\frac{j^2}{\sigma}dV + \frac{d}{dt}\int_V\frac{B^2}{8\pi}dV. \quad (6)$$

The left part of this equation represents the total power of the forces exerted on fluxoids, the integration is performed along the fluxoid length, and the summation is carried out over all fluxoids. In the right part, the first integral is taken over the crust volume, while the second integral is taken over the crust volume and the entire space outside the NS. Assuming, for simplicity, that the mean core magnetic field is uniform and substituting for all quantities their values at the crust-core boundary, we can write the left part as $(f_n + f_b + f_v)v_p(R_c)N_p\langle l_p\rangle$, where $N_p = 4\pi R_c^2 B_c/\Phi_0$ is the total number of fluxoids, and $\langle l_p\rangle = 4R_c/3$ is the mean fluxoid length. Thus, instead of the forces per unit length, we introduce the total forces exerted on the fluxoids in the core:

$$F_{n,b,v} = f_{n,b,v}\times 4R_c/3\times N_p. \quad (7)$$

We can also introduce a quantity that has the meaning of the force acting on the fluxoid roots as they move:

$$F_{crust}(v_p) = -\frac{1}{v_p}\left(\int_{V_{crust}}\frac{j^2}{\sigma}dV + \frac{d}{dt}\int_V\frac{B^2}{8\pi}dV\right). \quad (8)$$

If the fluxoids move outward (the velocity is positive) and if the magnetic energy in the crust increases, then this force is negative; i.e., it prevents the motion of the fluxoid roots toward the magnetic equator. Equation (6) can now be rewritten as

$$F_n + F_b + F_v(v_p) + F_{crust}(v_p) = 0. \quad (9)$$

The magnetic-field evolution in a solid conducting crust is described by the induction equation without a convective term:

$$\frac{\partial\mathbf{B}}{\partial t} = -\frac{c^2}{4\pi}\nabla\times\left(\frac{1}{\sigma}\nabla\times\mathbf{B}\right), \quad (10)$$

where σ is the crust conductivity. We study the magnetic evolution of NSs with classical magnetic fields (10^{12}–10^{13} G). In this case, the crustal electrons are nonmagnetized, and the conductivity is a scalar.

We consider the evolution of a poloidal magnetic field with only a dipole component outside the NS. In spherical r, θ, ϕ coordinates, in which the vertical axis coincides with the magnetic dipole axis, it is convenient to introduce a vector potential $A = (0, 0, A_\phi)$, where $A_\phi = S(r, t)\sin\theta/r^2 = B_{e0}R^2 s(r, t)\sin\theta/r$, B_{e0} is the NS field on

the magnetic equator at the initial time. Equation (10) can be rewritten as

$$\frac{4\pi\sigma}{c^2}\frac{\partial s}{\partial t} = \frac{\partial^2 s}{\partial r^2} - \frac{2s}{r^2}. \quad (11)$$

The magnetic-field components are written as a function of s as

$$B_r = \frac{2S}{r^2}\cos\theta, \quad B_\theta = -\frac{\sin\theta}{r}\frac{\partial S}{\partial r}. \quad (12)$$

There is no magnetic-field dissipation in a superconducting core, and its evolution is described by the equation

$$\frac{\partial \mathbf{B}_c}{\partial t} = \nabla \times (\mathbf{v}_p \times \mathbf{B}_c), \quad (13)$$

which can be rewritten for $s(r, t)$ as

$$\frac{\partial s}{\partial t} = -v_p\frac{\partial s}{\partial r}. \quad (14)$$

The integrals in the right part of Eq. (6) can be rewritten as

$$\int_{V_{crust}} \frac{j^2}{\sigma}dV = \frac{c^2 B_{e0}^2 R^4}{6\pi}\int_{R_c}^{R}\frac{1}{\sigma}\left(\frac{\partial^2 s}{\partial r^2} - \frac{2s}{r^2}\right)^2 dr, \quad (15)$$

$$\frac{d}{dt}\int_{V_{crust}}\frac{B^2}{8\pi}dV = B_{e0}^2 R^4\frac{d}{dt}\left(\frac{2}{3}\int_{R_c}^{R}\frac{s^2}{r^2}dr + \frac{1}{3}\int_{R_c}^{R}\left(\frac{\partial s}{\partial r}\right)^2 dr\right), \quad (16)$$

$$\frac{d}{dt}\int_{V_{vacuum}}\frac{B^2}{8\pi}dV = \frac{2B_{e0}^2 R^3}{3}s(R, t)\frac{ds(R, t)}{dt}. \quad (17)$$

The conductivity in a solid crust is mainly determined by the scattering of electrons by impurities and phonons. The scattering by phonons gives a major contribution to the conductivity at low densities and high temperatures, while the scattering by impurities dominates at high densities and low temperatures. We use expressions for the conductivity from Itoh *et al.* (1993) and Yakovlev and Urpin (1980). The frequency of electron scattering by phonons depends on the crustal temperature; we take the time dependence of the temperature from standard NS cooling calculations (Van Riper 1991). The frequency of scattering by impurities does not depend on temperature, but depends on impurity density. The latter is characterized by the impurity parameter Q, which has the meaning of rms deviation of the nuclear charge from the mean. Unfortunately, theory currently gives no definite impurity density in the NS crust. We therefore calculate the magnetic-field evolution for various values of this parameter in the range 0.01–1 and assume that Q does not depend on depth and time.

For a uniform core magnetic field ($r < R_c$), we can write

$$v_p = \alpha(t)r, \quad (18)$$

$$B_e(t) = B_{e0}\exp\left(-\int_0^t \alpha(t')dt'\right), \quad (19)$$

$$s(r, t) = \frac{B_c(t)}{B_{c0}}\frac{r^2}{R_c^2}, \quad (20)$$

where B_{c0} is the initial core field and $\alpha(t)$ can be determined from Eqs. (6) and (10). The following boundary condition must be satisfied at the NS surface ($r = R$):

$$\partial s/\partial r = -s/R. \quad (21)$$

The function s/r^2 must remain finite at the NS center ($r \longrightarrow 0$), which is automatically satisfied by Eq. (20). Equations (7)–(9) simultaneously give the fluxoid velocity and the inner boundary condition (at $r = R_c$) for Eq. (11).

We calculate the magnetic-field evolution of a NS as follows. Having chosen the initial core magnetic field, the initial $s(r, t = 0)$ profile in the crust, and the initial NS spin period P_0, we specify the initial condition. In addition, it is necessary to specify the density profile in the crust, the impurity parameter Q, the crust thickness, and the NR radius. For our calculations, we use the model of a $1.4M_\odot$ neutron star constructed for the hard equation of state by Pandharipande and Smith (1975), the NS radius R = 16.4 km, the crust thickness δR = 4200 m, and the moment of inertia $I = 2.12 \times 10^{45}$ g cm^2.

We assume that $v_p = v_n$, where v_n is given by Eq. (1). Having specified a sufficiently small time step Δt, we calculate $s(R_c, \Delta t)$ from Eq. (20), i.e., obtain the inner boundary condition for Eq. (11), and calculate the evolution of the crustal magnetic field in time Δt using an implicit scheme. Thus, we obtain $s(r, \Delta t)$ in the crust. Next, we calculate the integrals (15)–(17) and F_{crust} and then F_b and F_v ($v_p = v_n$). Finally, we derive F_n from Eq. (9) and determine ω using Eqs. (7) and (2). If $-\omega_{cr} < \omega < \omega_{cr}$, then the fluxoids and neutron vortexes actually move at the same velocity (comoving). If, alternatively, $\omega > \omega_{cr}$ or $\omega < -\omega_{cr}$, then our assumption that the velocities of fluxoids and neutron vortexes are equal is wrong: in the former and latter cases, fluxoids move more slowly (forward creeping) and faster than neutron vortexes (reverse creeping), respectively. If fluxoids move more slowly than neutron vortexes, then we assume that $\omega \equiv \omega_{cr}$. Next, we calculate $F_n = F_n(\omega_{cr})$ from Eqs. (2) and (7) and then find the true value of v_p as the root of Eq. (9) in the interval $[0, v_n]$ by the bisection method. Otherwise ($v_n < v_p$), we assume that $\omega \equiv -\omega_{cr}$, calculate $F_n = F_n(-\omega_{cr})$, and again find the true value of v_p in the interval $[v_n, \infty]$ from Eq. (9).

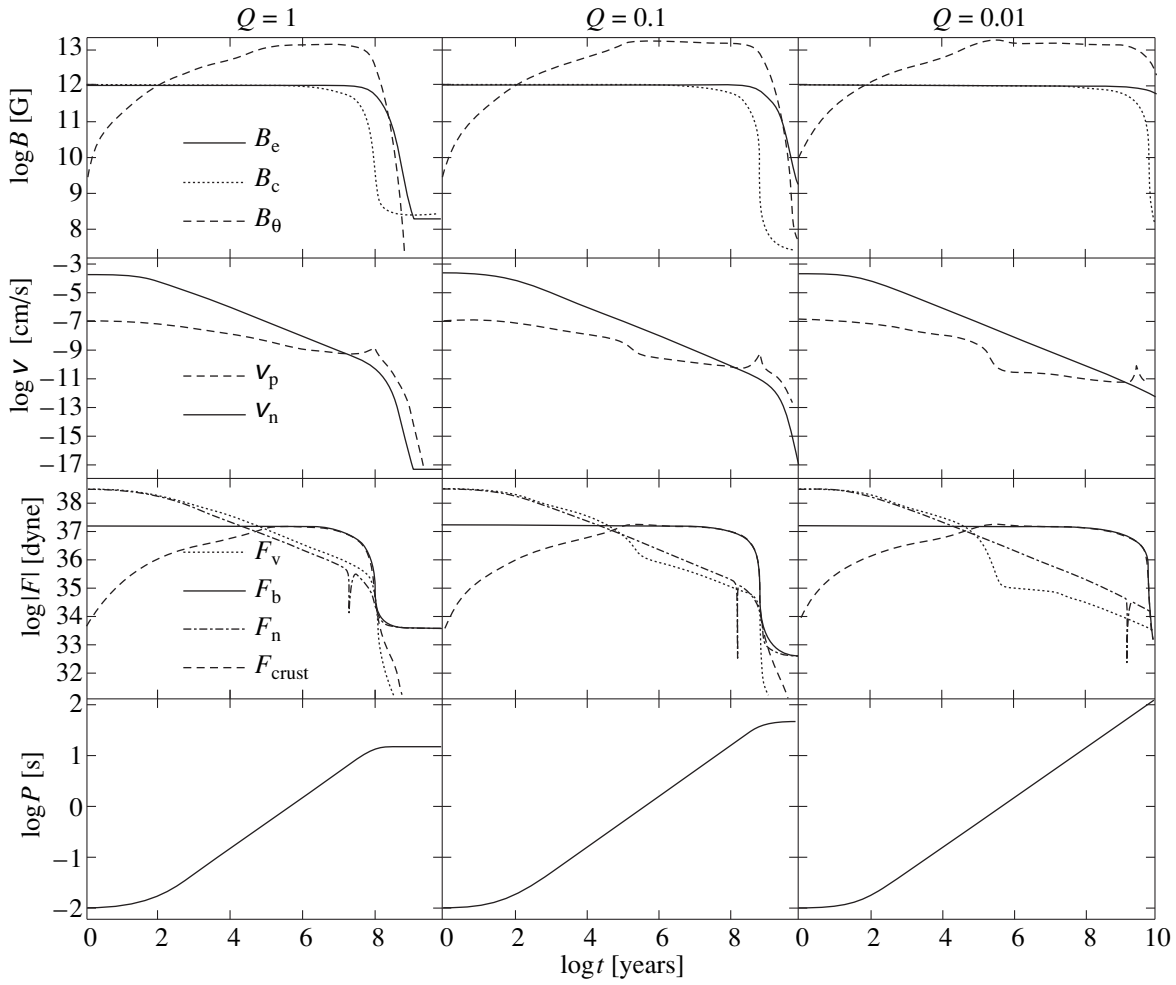

Fig. 3. Evolutionary curves for (from top to bottom) the crustal magnetic field, the NS surface magnetic field, and the θ field component at the core-crust boundary; the vortex and fluxoid velocities; the force exerted on fluxoids; and the NS spin period.

Because of the losses of rotational kinetic energy through the magnetodipole radiation and the ejection of a relativistic particle, the evolution of the NS spin period P can be calculated by using the formula

$$P\frac{dP}{dt} = \frac{32\pi^2}{3}\frac{B_e(t)^2 R^6}{c^3 I}.$$

We repeat these calculations at each time step.

RESULTS

If the magnetic field of a star was enhanced during collapse, then the bulk of the magnetic flux will pass through its core (Fig. 1, left part). However, a magnetic field can be generated in the surface layers of the already-formed young hot NSs (Urpin *et al.* 1986). In this case, the bulk of the NS total magnetic flux can pass through the crust (Fig. 1, right part), and the magnetic field in the NS crust will be much stronger than in its core. The Vela pulsar may have such a magnetic configuration (Chau *et al.* 1992). Here, we study the evolution of both configurations of the NS magnetic field.

In the former case, we chose $s(r, 0) = 1$ as the initial condition in the crust. In this case, the crustal field is initially radial, and the core field is equal to the field at the magnetic equator. Figure 3 shows the evolution of the magnetic fields, the velocities of the fluxoids and neutron vortexes, the forces exerted on the fluxoids, the NS spin period for $B_{e0} = B_{c0} = 10^{12}$ G, $P_0 = 0.01$ s, and various values of Q. Irrespective of the specific value of Q, the fluxoid velocity is initially lower than the velocity of neutron vortexes (forward creeping). The duration of this stage depends on Q: the smaller the Q, the shorter this stage. Thus, for example, fluxoids move more slowly than neutron vortexes at $Q = 0.01$ during $\sim 10^9$ years, while the velocities of both types of vortex lines become equal at $Q = 1$ in $\sim 10^7$ years. At $t \le 10^4$ years, the fluxoid velocity is virtually independent of Q and is determined by the balance of F_n and F_v [in Eq. (9), $(F_n, F_v) \gg (F_b, F_{crust})$]. In this case, $F_n > 0$ (expels fluxoids from the core) and $F_v < 0$. At $t > 10^4$ years,

Dependence of $\log(t_e)$ on B_{e0} and Q

Q \ B_{e0}, G	10^{12}	10^{13}
1	8.15	8.6
0.1	9.15	9.6
0.01	10.15	10.6

neutron vortexes affect the fluxoid dynamics only slightly, and the buoyancy force F_b becomes the main force responsible for the expulsion of fluxoids from the core. A θ magnetic-field component is generated in the crust near the boundary with the core, which exceeds the surface field by a factor of ~10. F_{crust} becomes the main force that prevents the outward motion of fluxoids; $(F_b, F_{crust}) \gg (F_n, F_v)$, and the fluxoid velocity depends on crust conductivity: the higher the crust conductivity (the smaller the Q), the lower the fluxoid velocity and the longer the time of magnetic-flux expulsion from the core. Thus, for example, the core field at $Q = 0.01$ begins to decrease only after $\sim 10^9$ years of evolution, while the NS surface field is essentially constant over the lifetime of the Universe. At $Q = 1$, the time of magnetic-field expulsion from the core is $\sim 10^7$ years. In this time, the fluxoid velocity becomes equal to the velocity of neutron vortexes and subsequently exceeds it. At this instant of time, F_n changes sign and begins to hinder the expulsion of fluxoids from the core. The fluxoid expulsion from the core ceases when the buoyancy force F_b is balanced by the force F_n from neutron vortexes. In this case, the fluxoid and vortex velocities again become equal (comoving). For the model of a NS constructed with the hard Pandharipande–Smith equation of state (PS model) with the initial magnetic field $B_{e0} = 10^{12}$ G, this occurs only for $Q = 1$. At lower values of Q, this stage is not reached on the Hubble time scale. The time of field expulsion from the core for $Q = 1$ is about 10^7 years, but the buoyancy force is balanced by the force from neutron vortexes as the core field decreases to 1.5×10^8 G. In this case, the fluxoid and vortex velocities fall to 3×10^{-18} cm s^{-1}, and the magnetic-flux expulsion from the core virtually ceases. Note that the NS surface magnetic field follows the core field with a delay, because the time of field diffusion through the crust in the NS model under consideration is $\sim 10^8/Q$ years (Urpin and Konenkov 1997).

In applications (for example, when modeling the evolution of a population of neutron stars in the Galaxy), the following analytic formula describing the evolution of the NS surface magnetic field can be of use:

$$B_e = B_{e0}\exp(-t/t_e) + B_{res}, \qquad (22)$$

where the characteristic decay time t_e of the surface field and the residual magnetic field B_{res} depend on B_{e0}, Q, and NS model. We calculated the magnetic and spin evolution of a NS for $B_{e0} = B_{c0} = 10^{13}$ G as well; the values of t_e for various B_{e0} and Q are given in the table. The residual magnetic field ($\sim 10^8$ G for $B_{e0} = 10^{12}$ G and $\sim 10^7$ G for $B_{e0} = 10^{13}$ G) is reached only for $Q = 1$. In the remaining cases, we may set $B_{res} = 0$ in Eq. (22).

We see from the table that the time of reduction in a NS surface magnetic field depends not only on conductivity, but also on the magnetic-field strength itself. This is because the buoyancy force is $F_b \propto B_c$ and because the force preventing the expulsion is $F_{crust} \propto B_c^2$. Therefore, as the magnetic field increases, the fluxoid velocity decreases, and the time of magnetic-flux expulsion from the core increases.

In Eq. (6), we disregard the force attributable to fluxoid curvature. If the radius of fluxoid curvature is comparable to the core radius, then this force will give rise to a coefficient of the order of unity near f_b in Eq. (6), and the time of flux expulsion from the core will also change by a coefficient of the order of unity; our results will not change qualitatively.

The magnetic field of a NS may be generated in its surface layer after its birth (Urpin *et al.* 1986). To model the evolution of such a magnetic configuration, we chose the following initial condition in the crust:

$$s(r, 0) = \begin{cases} B_{c0}/B_{e0}, & \text{if} \quad r < r_0 \\ (1 - r^2/r_0^2)(1 - R^2/r_0^2), & \text{if} \quad r_0 < r < R. \end{cases} \qquad (23)$$

The $s(r, 0)$ profile corresponds to the following magnetic configuration: the core field is $B_{c0} < B_{e0}$, the crustal field is radial at $R_c < r < r_0$, and the currents that produce the observed NS surface magnetic field B_{e0} flow in the $r_0 < r < R$ layer. Thus, the initial condition we chose models the magnetic configuration shown in the right part of Fig. 1. The parameters are the initial surface magnetic field B_{e0}, the initial core magnetic field B_{c0}, the thickness $z_0 = R - r_0$ of the surface layer where currents initially flow, and the impurity density described by parameter Q. Figure 4 shows the evolution of s. Specific values of the parameters are given in the caption to the figure. On the one hand, the field initially localized in the crustal surface layer (left part in Fig. 1) dissipates. In this case, it diffuses deep into the crust, just as in the case of evolution of the field localized only in the NS crust (Urpin and Muslimov 1992; Urpin and Konenkov 1997). On the other hand, the magnetic flux is expelled from the superconducting core into the crust; a θ magnetic-field component is generated near the crust-core boundary (or $\partial s/\partial r$), while the field in the core $s(R_c, t)$ decreases. Thus, for example, at the specified model parameters, the surface and core fields decrease by a factor of ~5 in 10^7 years (curve *2*) and diffuse to a depth of ~2000 m. The magnetic-flux expulsion from the core virtually ceases by 10^8 years, and s relaxes (curves *3*, *4*) to the state (curve *5*) specified by

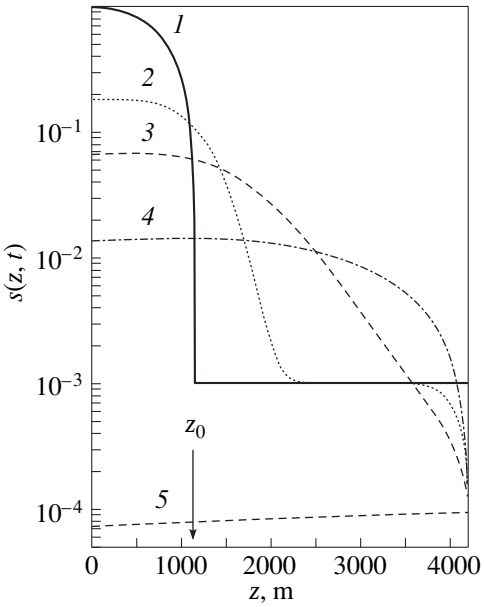

Fig. 4. Initial $s(z, 0)$ profile (*1*), where $z = R - r$ is the depth, and its evolution after (*2*) 10^7, (*3*) 10^8, (*4*) 10^9, and (*5*) 10^{10} years for the magnetic configuration in the right part of Fig. 1. The parameters are $B_{e0} = 10^{12}$ G, $B_{c0} = 10^9$ G, $Q = 1$, and $z_0 = 1146$ m. Here, B_{e0} is the initial surface magnetic field, B_{c0} is the initial core magnetic field, and z_0 is the thickness of the layer where currents flow at $t = 0$.

the boundary conditions $s(R_c, t) = \text{const}$ and Eq. (21) and by Eq. (11) for $\partial s/\partial t = 0$.

Figure 5 shows the evolution of the NS surface and core magnetic fields, the NS spin period, and the vortex and fluxoid velocities for $B_{e0} = 10^{12}$ G, $B_{c0} = 10^9$ G and for various impurity parameters Q and $z_0 = 1146$ m (the matter density at this depth is 10^{13} g cm^{-3}). Irrespective of Q, the fluxoid velocity is lower than the velocity of neutron vortexes for $t < 10^4$ years, while for $t > 10^4$ years, both types of vortex lines move at the same Q-dependent velocities. Thus, the effect of neutron vortexes on the fluxoid dynamics in this magnetic configuration is much stronger than that in the previous configuration. This directly follows from Eq. (2): the smaller the B_c (fluxoid density), the larger the f_n (the force exerted per unit fluxoid length by vortexes). The evolution of the NS surface magnetic field is determined by dissipation of the currents initially localized in a surface layer of thickness z_0 and coincides with the evolution of the magnetic field localized only in the NS crust (Urpin and Konenkov 1997) until all crustal currents dissipate. This occurs in $\sim 7 \times 10^8$ years for $Q = 1$ (with $B_c \approx 10^8$ G) and in $\sim 7 \times 10^9$ years for $Q = 0.1$ (with $B_c \approx 3 \times 10^7$ G). Subsequently, the characteristic evolution time of the NS surface magnetic field coincides with the time of magnetic-flux expulsion from the NS core, which exceeds the age of the Universe.

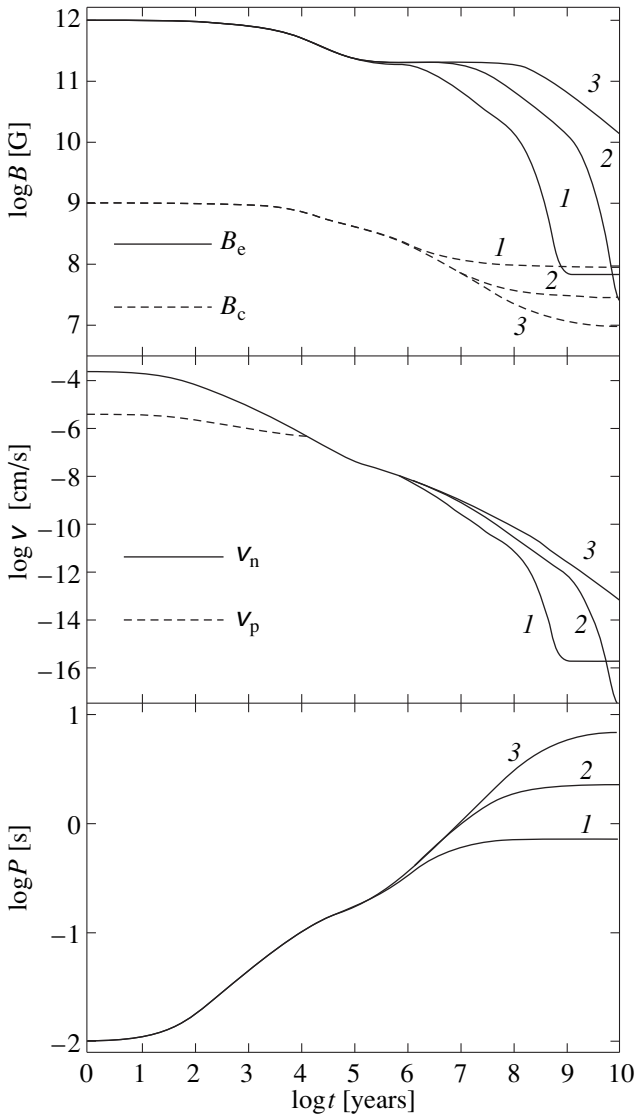

Fig. 5. Evolution of the NS surface and core magnetic fields, the vertex and fluxoid velocities, and the NS spin period for $B_{e0} = 10^{12}$ G, $B_{c0} = 10^9$ G, and $z_0 = 1146$ m. $Q = (1)$ 1, (*2*) 0.1, and (*3*) 0.01.

DISCUSSION

We have investigated the expulsion of magnetic flux from a superconducting NS core and its dissipation in a conducting crust. In contrast to previous studies (Ding *et al.* 1993; Jahan-Miri 1999), we performed self-consistent calculations by taking into account the inverse effect of a crustal magnetic line bending on the fluxoid velocity in the core. We showed that, if the bulk of the magnetic flux passes through the NS core, then the buoyancy of fluxoids (Muslimov and Tsygan 1985a, 1985b), rather than their interaction with outwardly moving neutron vortexes, is mainly responsible for the flux expulsion into the crust. The flux expulsion time can be determined from the balance of the buoyancy force and the drag force exerted on the fluxoid roots by

the NS crust. The higher the crust conductivity is and the stronger the NS magnetic field is, the longer the time of magnetic-flux expulsion from the core is. Konar and Bhattacharya (1999) calculated the expulsion of magnetic flux from the core by using the hypothesis of the so-called spindown-induced magnetic-field decay; in this hypothesis, neutron vortexes are assumed to be rigidly bound to fluxoids, and both types of vortex lines move at the same velocities throughout the entire NS evolution. We showed that if the bulk of the magnetic flux passes through the NS core, then this hypothesis is untenable.

It follows from the synthesis of populations of single radio pulsars (Bhattacharya *et al.* 1992; Hartmann *et al.* 1996) that the pulsar magnetic fields do not decay in their lifetimes. Our calculations are consistent with this conclusion: for all the values of B_{e0} and Q considered, the surface field decay time exceeds the lifetime of radio pulsars (10^7–10^8 years). For the model parameters to be determined more accurately, the results of calculations must be compared with the fields of NSs that passed the accretion stage in close binary systems. To perform such calculations requires that the effects associated with the crust heating by hot accreting material and with the emerging flow of accreting matter through the crust be included in the model. Both these factors can reduce the dissipation time of the crustal currents and the force F_{crust}.

The effect of neutron vortexes on the fluxoid dynamics is much stronger for the other possible magnetic configuration, when the bulk of the magnetic flux after the birth of a NS passes through its crust. In this case, however, the evolution of the observed NS surface magnetic field during the entire lifetime of the radio pulsar is entirely determined by crustal current dissipation. It coincides with the evolution of the field maintained by the currents that flow only in the NS crust. The evolution of such magnetic configurations was studied, for example, by Urpin and Muslimov (1992) and Urpin and Konenkov (1997).

ACKNOWLEDGMENTS

The work of D. Konenkov was supported by the A. Humboldt Foundation and by the Russian Foundation for Basic Research (project no. 00-02-04011) and the INTAS (grant no. 96-0154).

REFERENCES

1. M. Alpar, in *Neutron Stars: Theory and Observation*, Ed. by J. Ventura and D. Pines (Kluwer, Dordrecht, 1991), p. 49.
2. M. Alpar, S. Langer, and J. Sauls, Astrophys. J. **282**, 533 (1984).
3. G. Baym, C. Pethick, and D. Pines, Nature **224**, 673 (1969).
4. D. Bhattacharya, R. Wijers, J. Hartmann, and F. Verbunt, Astron. Astrophys. **254**, 198 (1992).
5. H. Chau, K. Cheng, and K. Ding, Astrophys. J. **399**, 213 (1992).
6. K. Ding, K. Cheng, and H. Chau, Astrophys. J. **408**, 167 (1993).
7. J. Hartmann, D. Bhattacharya, R. Wijers, and F. Verbunt, Astron. Astrophys. **322**, 477 (1997).
8. J. Harvey, M. Ruderman, and J. Shaham, Phys. Rev. D **33**, 2084 (1986).
9. N. Itoh, H. Hayashi, and Y. Kohyama, Astrophys. J. **418**, 405 (1993).
10. M. Jahan-Miri, astro-ph/9910490.
11. S. Konar and D. Bhattacharya, Mon. Not. R. Astron. Soc. **308**, 795 (1999).
12. E. M. Lifshitz and L. P. Pitaevskiĭ, *Course of Theoretical Physics, Vol. 5: Statistical Physics* (Nauka, Moscow, 1978; Pergamon, New York, 1980), Part 2.
13. A. G. Muslimov and A. I. Tsygan, Astrophys. Space Sci. **115**, 43 (1985a).
14. A. G. Muslimov and A. I. Tsygan, Pis'ma Astron. Zh. **11**, 196 (1985b).
15. V. Pandharipande and R. Smith, Nucl. Phys. A **237**, 507 (1975).
16. S. L. Shapiro and S. A. Teukolsky, *Black Holes, White Dwarfs, and Neutron Stars: the Physics of Compact Objects* (Wiley, New York, 1983; Mir, Moscow, 1985).
17. C. Thompson and R. Duncan, Astrophys. J. **408**, 194 (1993).
18. V. Urpin and D. Konenkov, Mon. Not. R. Astron. Soc. **292**, 167 (1997).
19. V. Urpin and A. Muslimov, Mon. Not. R. Astron. Soc. **256**, 261 (1992).
20. V. Urpin, S. Levshakov, and D. Yakovlev, Mon. Not. R. Astron. Soc. **219**, 703 (1986).
21. K. van Riper, Astrophys. J., Suppl. Ser. **75**, 449 (1991).
22. D. Yakovlev and V. Urpin, Astron. Zh. **57**, 526 (1980) [Sov. Astron. **24**, 303 (1980)].

Translated by V. Astakhov

Astronomy Letters, Vol. 27, No. 3, 2001, pp. 171–175. Translated from Pis'ma v Astronomicheskiĭ Zhurnal, Vol. 27, No. 3, 2001, pp. 203–208.

Diffusion of a Passive Scalar in a Rotating Medium with Anisotropic Turbulence

V. V. Pipin*

Institute for Solar–Terrestrial Physics, Siberian Branch, Russian Academy of Sciences, ul. Lermontova 126, Irkutsk, 664033 Russia

Received November 17, 1999; in final form, September 6, 2000

Abstract—We investigate the influence of turbulence anisotropy and rotation on the diffusion of a low-concentration passive scalar in a turbulent medium. Using the renormalization the diffusion tensor over the spectrum of turbulent fluctuations, we show that enhanced horizontal mixing reduces the vertical diffusion transport of a passive scalar. Allowance for rotation results in two effects, which have not been noted previously: (1) under the influence of Coriolis forces, horizontal turbulence also produces a vertical diffusion flux, with the horizontal and vertical diffusions being of the same order of magnitude for rapidly rotating stars and (2) in the case of rapid rotation, all diffusion fluxes of a passive scalar decrease in inverse proportion to the square root of the Coriolis number. © *2001 MAIK "Nauka/Interperiodica".*

Key words: *turbulence*

INTRODUCTION

The low Li abundance in the atmospheres of cool main-sequence stars is known to be closely related to the diffusion mixing of chemical elements beneath the convection zone. According to current views, a substantial (on evolution time scales) Li burning can take place at temperatures $>2.5 \times 10^6$ K or starting at depths >50 000 km from the bottom of the convection zone in a solar-type star. Lithium can be transported from the bottom of the convection zone to the burning region by weak turbulence. The mechanisms capable of generating turbulence beneath the convection zone are generally attributable to various instabilities of large-scale shear flows. These were considered in detail by Zahn (1983), Schatzman and Baglin (1991), Michaud and Zahn (1998). The most important property of turbulence beneath the convection zone is its anisotropy, which is so large that the turbulent flux fluctuations take place mainly in the horizontal direction (in other words, in the plane of the sphere). The vertical fluctuations are suppressed due to the high thermal stability of the radiative zone. Here, we do not consider internal gravity waves, which can also contribute to the Li transport.

In their numerical simulations, Vincent *et al.* (1996) showed that strong horizontal turbulence reduces the vertical diffusion efficiency of a passive scalar, mainly because horizontal mixing smoothes out the scalar concentration of nonuniformities transported by vertical motions. As a result, the characteristic vertical decay scale of concentration fluctuations decreases, causing the vertical diffusion efficiency to decrease.

Despite the simplicity of qualitative considerations in favor of this effect, quantitative estimates of the vertical diffusion in the presence of strong horizontal turbulence have been obtained so far only in numerical simulations. This study aims to support the numerical simulations by analytic calculations of the turbulent diffusion coefficient for a passive scalar. The effects are calculated by using the version of the renormalization method over the turbulent fluctuation spectrum proposed by Bykov and Toptygin (1990). The calculations performed by Rüdiger and Pipin (2000) in a quasi-linear approximation indicate that vertical turbulent diffusion can decrease with increasing horizontal mixing only in a special case where the vertical and horizontal turbulences have the same source (e.g., random forces of the same nature). This is apparently not the case for turbulence beneath the convection zone.

Another interesting phenomenon, which we took into account in our calculations, is the influence of stellar rotation on turbulent diffusion. The result obtained by Rüdiger and Pipin (2000) indicate that, even in the absence of vertical velocity-field fluctuations in the initial turbulence, the modification of turbulent fluxes under the effect of Coriolis forces triggers the radial transport of a passive scalar. Thus, the effects of horizontal turbulence and Coriolis forces can compete with each other.

In the next section, we derive the turbulent diffusion tensor by renormalization with allowance for the effect of rotation on turbulence. The paper ends with a discussion of possible applications of our results.

* E-mail address for contacts: pip@iszf.irk.ru

1063-7737/01/2703-0171$21.00 © 2001 MAIK "Nauka/Interperiodica"

THE TURBULENT DIFFUSION TENSOR OF A PASSIVE SCALAR IN A ROTATING MEDIUM

According to Landau and Lifshitz (1986), the diffusion of a low-concentration passive scalar is given by

$$\frac{\partial \rho C}{\partial t} + \mathrm{div}\,\rho(\mathbf{u}C + \rho D\nabla C) = 0, \quad (1)$$

where D is the microscopic diffusion coefficient. Suppose that the velocity field satisfies the quasi-elasticity condition

$$\mathrm{div}(\rho\mathbf{u}) = 0.$$

Assume that the mean and random concentration and velocity components

$$C = C' + \bar{C}, \quad \mathbf{u} = \mathbf{u}' + \bar{\mathbf{u}} \quad (2)$$

can be separated in a turbulent medium. The calculations are performed in a rotating coordinate system with $\bar{\mathbf{u}} = 0$. Suppose that the microscopic diffusion is weak compared to the turbulent diffusion. Substituting Eq. (2) in Eq. (1) and averaging yield

$$\frac{\partial \rho \bar{C}}{\partial t} - \partial_i \rho D_{ij} \partial_j \bar{C} = 0, \quad (3)$$

where D_{ij} is an unknown turbulent diffusion tensor. In a rotating medium with horizontal turbulence anisotropy, the diffusion can be represented as

$$D_{ij} = D_\parallel g_i g_j + D_\perp(\delta_{ij} - g_i g_j) + D_\Omega \frac{\Omega_i \Omega_j}{\Omega^2} + D_{\Omega_g} \frac{\mathbf{\Omega g}}{\Omega^2}(\Omega_i g_j + \Omega_j g_i). \quad (4)$$

Here, $\mathbf{g}$ is a unit vector in the vertical (radial) direction; $D_\parallel$ and $D_\perp$ are the vertical and horizontal diffusion tensor components; and D_Ω and D_{Ω_g} are the diffusion tensor components induced by the effect of rotation on turbulence.

Apart from Eq. (3), we consider a different equation for the concentration, in which averaging is performed over all harmonics, except for a narrow range of wave vectors $\Delta\mathbf{k}$:

$$\frac{\partial \rho \tilde{C}}{\partial t} - \partial_i \rho D'_{ij} \partial_j \tilde{C} + \partial_i \rho \tilde{C} \partial_j \delta u'_i = 0, \quad (5)$$

where

$$\delta\mathbf{u}'(\mathbf{r}, t) = \int_{-\infty}^{+\infty} d\omega \int_{\Delta k} d\mathbf{k} d\hat{\mathbf{u}}'(\mathbf{k}, \omega) \exp i(\mathbf{kr} - \omega t)$$

is the nonaveraged part of the velocity; the integration over $d\mathbf{k}$ is performed within a spherical layer of thickness $\Delta\mathbf{k}$; $\tilde{C}$ are the concentration fluctuations that were not averaged over the random velocity; and D'_{ij} is the diffusion tensor attributable to the turbulent velocity field minus $\delta\mathbf{u}'$. Averaging Eq. (5) over an ensemble of $\delta\mathbf{u}'$ must lead to Eq. (3) with a complete diffusion tensor D_{ij}.

Equation (5) can be averaged based on the theory of disturbances using the smallness of $\delta\mathbf{u}'$. Since $\Delta k \ll k$ is chosen arbitrarily, this approach does not limit the accuracy of the results obtained. When the averaging is performed, the Fourier harmonics of the velocity field from the Δk range are assumed to not correlate with the harmonics outside this range. This corresponds to the model representations of Kolmogorov-type turbulence. The method of renormalizing the diffusion tensor we used was described in detail by Bykov and Toptygin (1990).

Assuming that $\tilde{C} = \bar{C} + \delta C$ and $\langle \delta C \rangle = 0$, where the angular brackets denote averaging over an ensemble of $\delta\mathbf{u}'$, and averaging Eq. (5), we obtain

$$\frac{\partial \rho \bar{C}}{\partial t} - \partial_i \rho D'_{ij} \partial_j \bar{C} + \partial_i \rho \langle \delta C \delta u'_i \rangle = 0. \quad (6)$$

The correction δC in this equation must be calculated from

$$\frac{\partial \rho \delta C}{\partial t} - \partial_i \rho D'_{ij} \partial_j \delta C + \partial_i (\rho \bar{C} \delta u'_i) = 0. \quad (7)$$

The velocity field $\delta\mathbf{u}'$ in the rotating coordinate system satisfies the equation

$$\frac{\partial \delta u'_i}{\partial t} + 2(\mathbf{\Omega} \times \delta\mathbf{u}')_i + \frac{1}{\rho}\partial_j \delta p' - \nu_T \Delta \delta u'_i - \frac{\delta f'_i}{\rho} = 0, \quad (8)$$

where $\delta p'$ and $\delta f'_i$ are the pressure fluctuations and the random forces corresponding to harmonics from the Δk range. We use the diffusion approximation to simplify our calculations by assuming that $\|\partial_i D_{ij} \partial_j \delta C\| \gg \|\partial_i \delta C\|$. The time derivatives of the turbulent fluxes can then be disregarded. Taking a Fourier transform of Eqs. (7) and (8) and calculating the turbulent flux of concentration fluctuations yield the turbulent diffusion tensor $D_{ij} = D'_{ij} + \Delta D_{ij}$, in which

$$\Delta D_{ij} = \int_{\Delta\mathbf{k}} d\mathbf{k} \frac{\langle \hat{u}'_i(\mathbf{k}) \hat{u}'_j(-\mathbf{k}) \rangle}{\hat{k}_n \hat{k}_m D'_{nm}}, \quad (9)$$

where $\hat{\mathbf{k}}$ is a unit wave vector. According to the condition, the value of D'_{ij} differs only slightly from the true value of D_{ij}, and we can replace D'_{nm} with D_{nm} in Eq. (9) with the same accuracy with which Eqs. (7) and (8) were written. Integrating Eq. (9) over all wave vectors yields a transcendental equation for the turbulent diffusion tensor

$$D_{ij} = \int d\mathbf{k} \frac{\langle \hat{u}_i'(\mathbf{k})\hat{u}_j'(-\mathbf{k})\rangle}{\hat{k}_n\hat{k}_m D_{nm}}. \quad (10)$$

In order to calculate the correlation tensor of the velocity field in Eq. (10), we introduce a correlation spectral tensor of the initial turbulence. By the initial turbulence, we mean turbulence that exists in the absence of rotation but is in the presence of real turbulence sources. According to current views, turbulence in the radiative zone can be generated by the various types of instability associated with a large-scale shift in angular velocity and with meridional circulation. Since the radiative zone is characterized by a high stability to thermal disturbances, there the turbulence is highly anisotropic. We assume the initial turbulence to be statistically uniform, stationary, and anisotropic along the unit radial vector **g**,

$$\begin{aligned} Q_{ij}^{(0)}(\mathbf{k},\mathbf{k}') &= \langle \hat{u}_i^{(0)}(\mathbf{k})\hat{u}_j^{(0)}(\mathbf{k}')\rangle \\ &= \delta(\mathbf{k}+\mathbf{k}')\left(\frac{E(\mathbf{k})}{8\pi k^2}(\delta_{ij}-\hat{k}_i\hat{k}_j) + \frac{3E_2(k)}{8\pi k^2}(\delta_{ij}-\hat{k}_i\hat{k}_j\right. \\ &\left. -(\mathbf{g}\cdot\hat{\mathbf{k}})^2\delta_{ij} - g_ig_j + (\mathbf{g}\cdot\hat{\mathbf{k}})(g_i\hat{k}_j + g_j\hat{k}_i))\right). \end{aligned} \quad (11)$$

The $E(k)$ and $E_2(k)$ spectra can be related to the vertical and horizontal turbulence intensities by

$$\langle u_\parallel^{(0)2}\rangle = \frac{1}{3}\int E(k)dk,\ \langle u_\perp^{(0)2}\rangle = \frac{1}{2}\int E_2(k)dk.$$

Solving Eq. (8) and substituting the solution in Eq. (10) yield the following relation for the diffusion tensor:

$$D_{ij} = \int d\mathbf{k} \frac{\left(\delta_{in} + \frac{2(\boldsymbol{\Omega}\cdot\hat{\mathbf{k}})}{\nu_T k^2}\varepsilon_{ian}\hat{k}_a\right)\left(\delta_{jm} + \frac{2(\boldsymbol{\Omega}\cdot\hat{\mathbf{k}})}{\nu_T k^2}\varepsilon_{jbm}\hat{k}_b\right)Q_{nm}^{(0)}(\mathbf{k},-\mathbf{k})}{\hat{k}_n\hat{k}_m D_{nm}\left(1+\frac{4(\Omega\cdot\hat{k})^2}{\nu_T^2 k^4}\right)^2}, \quad (12)$$

where D_{mn} has the structure of Eq. (4). In general, Eq. (12) cannot be solved. Let us consider two important cases.

First, we neglect the effect of rotation. Then, $D_\Omega = D_{\Omega_g} = 0$, and

$$\begin{aligned} D_\parallel &= \int f_1(S)\frac{E(k)}{4k^2 D_\parallel}dk, \\ D_\perp &= \int\left(f_2(S)\frac{E(k)}{4k^2 D_\parallel} + f_1(S)\frac{3E_2(k)}{8k^2 D_\parallel}\right)dk, \end{aligned} \quad (13)$$

where we introduced $S^2 = D_\perp/D_\parallel$; the functions f_1 and f_2 are written in the Appendix. In order to analyze Eq. (13), it is convenient to pass to the mixing-length approximation:

$$\begin{aligned} E(k) &\sim 6\langle u_\parallel^{(0)2}\rangle\delta(k-l_\parallel^{-1}), \\ E_2(k) &\sim 4\langle u_\perp^{(0)2}\rangle\delta(k-l_\perp^{-1}), \\ \nu_T k^2 &\sim \tau_{\text{cor}}^{-1}. \end{aligned}$$

Let us introduce the anisotropy parameters $A^2 = \langle u_\perp^{(0)2}\rangle/\langle u_\parallel^{(0)2}\rangle$ and $A'^2 = l_\perp^2/l_\parallel^2$. By substituting and integrating these expressions in Eq. (13), we obtain:

$$\begin{aligned} D_\parallel^2 &= f_1(S)\langle u_\parallel^{(0)2}\rangle l_\parallel^2, \\ D_\parallel D_\perp &= (f_1(S)A^2A'^2 + f_2(S))\langle u_\parallel^{(0)2}\rangle l_\parallel^2. \end{aligned} \quad (14)$$

From this pair of relations, we can derive a transcendental equation that relates S to the anisotropy parameters. An approximate numerical solution of this equation yields $S \approx A^2A'^2$ at $A, A' > 1$. In this case, we obtain for the vertical diffusion

$$D_\parallel = \sqrt{f_1(A^2A'^2)}\sqrt{\langle u_\parallel^{(0)2}\rangle}l_\parallel. \quad (15)$$

At $A, A' \gg 1$,

$$D_\parallel \sim \frac{\sqrt{\pi}}{AA'}\sqrt{\langle u_\parallel^{(0)2}\rangle}l_\parallel, \quad D_\perp \sim \sqrt{\langle u_\perp^{(0)2}\rangle}l_\perp. \quad (16)$$

As we see from Eq. (16), the decrease in vertical diffusion can be caused by both an increase in intensity and by an increase in the correlation scales of horizontal mixing, because the two effects lead to the smoothing of the scalar nonuniformities transported by vertical motions. If the horizontal and vertical correlation scales of turbulence are approximately equal ($A' \approx 1$), formula (15) is in satisfactory agreement with the numerical simulations by Vincent *et al.* (1996). This is demonstrated by the figure, in which $D_\parallel/\sqrt{\langle u_\parallel^{(0)2}\rangle}\,l_\parallel$ ratio is plotted against the anisotropy parameter A. The dots in the figure represent the numerical calculations by Vincent *et al.* (1996), and the line indicates the analytic curve corresponding to Eq. (15). The close match between the shapes of the numerical and analytic curves can be explained by the fact that both numerical and analytic calculations yield the law $D_\parallel \sim A^{-1}$ at large A. The dif-

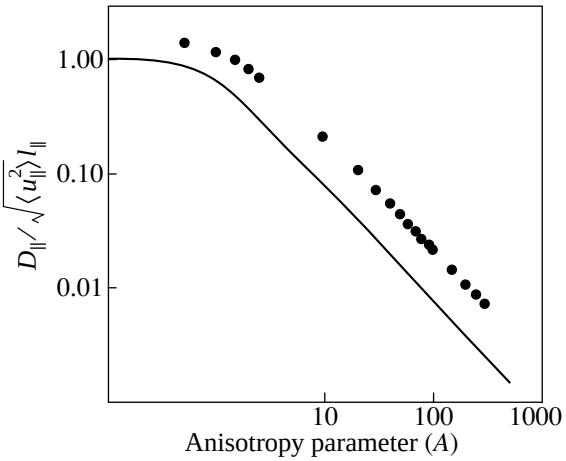

$D_\parallel/\sqrt{\langle u_\parallel^{(0)2}\rangle}\, l_\parallel$ versus turbulence anisotropy parameter $A = \sqrt{\langle u_\perp^{(0)2}\rangle/\langle u_\parallel^{(0)2}\rangle}$. The dots indicate the numerical data from Vincent *et al.* (1996); the solid line represents the dependence calculated from Eq. (15).

ference in numerical values can apparently be attributed to the different shapes of the turbulence spectra used.

Our method of calculation also indicates that the horizontal concentration of fluctuation nonuniformities are smoothed out as the anisotropy turbulence increases. The degree of horizontal scalar fluctuation nonuniformity can be estimated by determining the characteristic horizontal fluctuation scale L_H

$$L_H \sim \sqrt{\frac{\langle \delta C^2\rangle}{((\nabla_i - g_i(\mathbf{g}\cdot\nabla)\delta C)^2}},$$

where $\nabla_i - g_i(\mathbf{g}\cdot\nabla)\delta C$ is the derivative of the passive-scalar fluctuation in a direction perpendicular to g. We assume the mean scalar concentration to be nonuniform only in the direction of g. In the mixing-length approximation (omitting details of our calculations), we then obtain

$$\langle \delta C^2\rangle = \{(\mathbf{g}\cdot\nabla)\bar{C}\}^2 \frac{3}{4}\frac{\langle u_\parallel^{(0)2}\rangle l_\parallel^4}{D_\parallel^2} f_3(S),$$

$$\langle (\nabla_i - g_i(\mathbf{g}\cdot\nabla)\delta C)^2\rangle = \{(\mathbf{g}\cdot\nabla)\bar{C}\}^2 \frac{3}{4}\frac{\langle u_\parallel^{(0)2}\rangle l_\parallel^2}{D_\parallel^2} f_4(S),$$

where the functions f_3 and f_4 are written in the Appendix. From these equations, we derive

$$L_H = l_\parallel \sqrt{f_3(S)/f_4(S)}. \quad (17)$$

At $A \gg 1$, $L_H \sim \sqrt{\ln\frac{2A}{11}}$; i.e., the scalar fluctuation nonuniformities are smoothed out with increasing intensity of horizontal mixing. According to the interpretation of Vincent *et al.* (1996), the horizontal smoothing of scalar concentration fluctuation nonuniformities ultimately results in a decrease of the vertical diffusion coefficient.

Let us now consider the effect of rotation. Rotation modifies turbulence, which leads to additional diffusion fluxes of a passive scalar in the medium. As was shown by Chechkin *et al.* (1997), similar effects arise in the presence of a mean turbulence helicity. Rotation is known to induce the helicity of a turbulent velocity field. Note that the corresponding terms (of the type $\frac{2(\Omega\cdot\hat{k})}{\nu_T k^2}\varepsilon_{ian}\hat{k}_a Q_{mn}^{(0)}$) are present in the diffusion tensor Eq. (12). At the same time, Krause and Rädler (1980) pointed out that rotation alone is not enough for the mean helicity to be nonzero. The presence of, for example, a density gradient is required. In our case, the mean helicity is zero.

Equation (12) can be simplified for $\Omega^* = 2\Omega\tau_{cor} \gg 1$ (Ω^* is the Coriolis number). In this case, we derived the following relations for the diffusion tensor components:

$$D_\parallel = \int \frac{f(S,\Omega^*)dk}{4D_\parallel k^2}\left(E(k) + 3E_2(k)\left(\frac{3}{8} + \frac{7}{8}\cos^2\theta\right)\right),$$

$$D_\perp = \int \frac{f(S,\Omega^*)dk}{4D_\parallel k^2}\left(E(k) + 3E_2(k)\left(-\frac{3}{8} + \frac{7}{8}\cos^2\theta\right)\right),$$

$$D_\Omega = \int \frac{f(S,\Omega^*)dk}{4D_\parallel k^2}\left(E(k) + 3E_2(k)\left(\frac{7}{8} + \frac{3}{8}\cos^2\theta\right)\right), \quad (18)$$

$$D_{\Omega_g} = -\int \frac{f(S,\Omega^*)dk}{4D_\parallel k^2}\left(\frac{9E_2(k)}{4}\right),$$

where

$$f(S,\Omega^*) = \frac{\pi}{\Omega^*(1 + S^2 + \cos 2\theta(S^2 - 1))},$$

and $\cos\theta = \mathbf{g}\cdot\boldsymbol{\Omega}/|\Omega|$. In the mixing-length approximation, the diffusion tensor components can be expressed explicitly as

$$D_{rr} = D_\parallel + D_\Omega\cos^2\theta + 2D_{\Omega_g}\cos^2\theta$$

$$= \sqrt{\frac{\pi\langle u_\perp^{(0)2}\rangle}{192\Omega^*}\frac{l_\perp^2}{\cos^2\theta + 3}}(9 + \cos^2\theta + 21\cos^4\theta)\sqrt{1 + \frac{1}{AA'}}, \quad (19)$$

$$D_{\theta\theta} = D_\perp + D_\Omega\sin^2\theta$$

$$= \sqrt{\frac{\pi\langle u_\perp^{(0)2}\rangle}{192\Omega^*}\frac{l_\perp^2}{\cos^2\theta + 3}}(12 + 9\cos^2\theta\sin^2\theta)\sqrt{1 + \frac{1}{AA'}},$$

where D_{rr} and $D_{\theta\theta}$ are the radial and latitudinal diffusion tensor components, respectively. Having divided

the first equation by the second one, we obtained $D_{rr}/D_{\theta\theta} = f'(\theta)$ for a rapidly rotating medium (here, $f'(\theta)$ is a function of colatitude). Thus, we conclude that, in a rapidly rotating medium, the Coriolis forces can compete with the suppression of horizontal diffusion by enhanced horizontal mixing. In this case, the effective diffusion coefficients are of the same order of magnitude. It also follows from Eq. (19) that, at $\Omega^* \gg 1$, all diffusion coefficients decrease as $\Omega^{*-1/2}$, because the turbulence intensity is suppressed in inverse proportion to Ω^*.

To quantitatively estimate the diffusion coefficients in the solar-tachocline region, we take $\sqrt{\langle u_\perp^{(0)2}\rangle}\, l_\perp \approx 10^5$ cm^2 s^{-1}, according to Michaud and Zahn (1998); since $\sqrt{\langle u_\perp^{(0)2}\rangle}/l_\perp \approx \Delta\Omega \approx 10^{-6}$ s^{-1} is of the order of the rotation nonuniformity, the Coriolis number is $\Omega^* \approx 6$. It then follows from Eq. (19) that $D_{rr} \approx 10^4$ cm^2 s^{-1}, with the effective latitudinal diffusion being of the same order of magnitude. For the depth dependence of the diffusion coefficients to be estimated, specific models for the internal structure of the solar radiative zone must be invoked, as was done, for example, by Brun *et al.* (1998). Our estimate, which is valid for turbulence parameters near the base of the convection zone, is in agreement with that from the above paper. Note once again that the inferred vertical diffusion of a passive scalar results from allowance for the effect of rotation on turbulence; as a result, horizontal turbulence, along with vertical one, also contributes to D_{rr}. If we ignored this effect, the estimate would be smaller by two orders of magnitude [assuming that A, $A' \approx 100$, according to Michaud and Zahn (1998)].

CONCLUSION

Our main results can be summarized as follows. For the first time, it has been analytically shown that enhanced horizontal mixing actually reduces the vertical diffusion transport of a passive scalar. Allowance for rotation leads to two effects, which have not been noted previously: (1) under the effect of Coriolis forces, horizontal turbulence induces a vertical diffusion flux, with the horizontal and vertical diffusions being of the same order of magnitude at $\Omega^* \gg 1$, because both are mainly attributable to the same source; and (2) all diffusion fluxes decrease in inverse proportion to $\sqrt{\Omega^*}$. Hence, we immediately conclude that rapidly rotating cool solar-type stars are richer in Li, which is actually observed. Our results can also be applied to rapidly rotating hot B stars, whose atmospheres are rich in the products of the CNO-cycle proceeding in the interior. Stars of this type have outer radiative zones. In this case, the effect of rotation on the horizontal turbulence in the radiative zone could transport the CNO-cycle products from the zone of nuclear reactions to the surface (however, other effects cannot be ruled out either). I am grateful to S. Andrievskiĭ for this remark.

ACKNOWLEDGMENTS

This work was supported by the Russian Foundation for Basic Research (project nos. 99-02-16 088 and 00-15-96 659).

I am grateful to L.L. Kitchatinov for a discussion of several relevant issues.

REFERENCES

1. A. S. Brun, S. Turck-Chieze, and J. P. Zahn, in *SOHO 6/GONG 98 Workshop on Structure and Dynamics of the Interior of the Sun and Sun-like Stars, Boston, 1998*, Ed. by S. G. Korzennik and A. Wilson (European Space Agency, Noordwijk, 1998), Vol. 1; ESA SP **418** (1), 439 (1998).
2. A. M. Bykov and I. I. Toptygin, Zh. Éksp. Teor. Fiz. **97**, 194 (1990) [Sov. Phys. JETP **70**, 108 (1990)].
3. A. V. Chechkin, A. V. Tur, and V. V. Yanovsky, Electronic publication at http: www.lanl.gov/, Chao-Dyn, 9706007, 1997.
4. F. Krause and K. H. Rädler, *Mean-Field Magnetohydrodynamics and Dynamo Theory* (Akademie-Verlag, Berlin, 1980).
5. L. D. Landau and E. M. Lifshitz, *A Course of Theoretical Physics*, *Vol. 6: Fluid Mechanics* (Nauka, Moscow, 1986; Pergamon, New York, 1987).
6. G. Michaud and J.P. Zahn, Theor. Comput. Fluid Dyn. **11**, 183 (1998).
7. G. Rüdiger and V. V. Pipin, Astron. Astrophys. (2000).
8. E. Schatzman and A. Baglin, Astron. Astrophys. **249**, 125 (1991).
9. A. Vincent, G. Michaud, and M. Meneguzzi, Phys. Fluids **8** (5), 1312 (1996).
10. J.-P. Zahn, in *Astrophysical Processes in Upper Main Sequence Stars*, Ed. by A. Maeder and B. Hauck (Geneva Obs. Publ., Geneva, 1983), p. 185.

APPENDIX

The following functions were used here:

$$f_1 = \frac{2}{S^2 S'^2}\left((1+S'^2)\frac{\arctan(S')}{S'} - 1\right),$$

$$f_2 = \frac{2}{S^2 S'^2}\left((S'^2-1)\frac{\arctan(S')}{S'} + 1\right),$$

$$f_3 = \frac{2}{S^4 S'^2}\left((S'^2-1)\frac{\arctan(S')}{S'} + 1\right),$$

$$f_4 = \frac{2}{S^4 S'^4}\left((S'^4-2S'^2-3)\frac{\arctan(S')}{S'} + 3 + S'^2\right),$$

$$S' = \sqrt{\frac{1-S^2}{S^2}}.$$

Translated by Yu. Safronov

Astronomy Letters, Vol. 27, No. 3, 2001, pp. 176–180. Translated from Pis'ma v Astronomicheskiĭ Zhurnal, Vol. 27, No. 3, 2001, pp. 209–214.

Propeller Effect during Magnetocentrifugal Plasma Acceleration

S. V. Bogovalov*

Institute of Astrophysics, Moscow Institute of Engineering Physics, Kashirskoe shosse 31, Moscow, 115409 Russia

Received March 2, 2000

Abstract—We study the effect of magnetic-field axial asymmetry on the magnetocentrifugal acceleration of plasma when it flows in a source's rotating magnetosphere (propeller effect). For an axisymmetric steady plasma flow, the first corrections to the energy that arise when the source rotates slowly are proportional to Ω^4, suggesting a highly inefficient plasma acceleration. Magnetic-field axial asymmetry is shown to substantially modify the acceleration. The first corrections arise even in the first order in Ω. The plasma acceleration turns out to be considerably more efficient in a non-axisymmetric magnetic field. *© 2001 MAIK "Nauka/Interperiodica".*

Key words: *plasma astrophysics, hydrodynamics, and shock waves*

INTRODUCTION

Plasma flow in the magnetic field of a rotating source takes place in many astrophysical objects, from ordinary stars to galactic nuclei. The plasma in such flows is accelerated by the so-called magnetocentrifugal mechanism. This acceleration has a simple mechanical analogy. Since the magnetic field is frozen into the plasma, its motion can be considered as the motion of a bead on a wire (Blandford and Payne 1982), with a magnetic field line acting as the wire. When the wire rotates, the bead is accelerated by the centrifugal effect. Numerous studies of this acceleration mechanism in a model with an axisymmetric magnetic field, both analytic and numerical, show that its efficiency is fairly high only for nonrelativistic velocities of the outflowing plasma (Bogovalov and Tsinganos 1999). By contrast, the acceleration in the relativistic limit is absolutely negligible and is apparently of no astrophysical interest (Bogovalov 1997, 2000; Beskin *et al.* 1998). This disappointing conclusion was reached in various models and approximations for various (axisymmetric) magnetic-field configurations.

At the same time, the magnetic fields of actual astrophysical objects are not axisymmetric. Therefore, it is of interest to answer the question of how the acceleration of outflowing plasma in a magnetic field will change in the case of axial asymmetry. We attempted to answer this question in Bogovalov (1999), where we considered the plasma flow from an oblique rotator with a split-monopole-type field. In this model, the magnetic-field component normal to the stellar surface is uniform over the surface and changes sign only at the magnetic equator. This type of magnetic-field nonuniformity was found to have no effect on the plasma dynamics, and the relativistic plasma acceleration in the field of such an object remains as inefficient as that in an axisymmetric field. Here, we consider the question of how azimuthal nonuniformity of the magnetic-field magnitude will affect the magnetocentrifugal plasma acceleration.

BASIC EQUATIONS

The system of equations for the dynamics of a cold relativistic plasma in the approximation of ideal magnetohydrodynamics is (Akhiezer *et al.* 1975)

$$mn\left(\frac{\partial\gamma\mathbf{v}}{\partial t} + (\mathbf{v}\nabla)\gamma\mathbf{v}\right) = q\mathbf{E} + \frac{1}{c}[\mathbf{jH}], \quad (1)$$

$$\frac{\partial\mathbf{H}}{c\partial t} = -\mathrm{curl}\mathbf{E}, \quad (2)$$

$$\mathrm{curl}\mathbf{H} = \frac{4\pi}{c}\mathbf{j} + \frac{\partial\mathbf{E}}{c\partial t}, \quad (3)$$

$$\mathrm{div}\,\mathbf{H} = 0, \quad (4)$$

$$\mathrm{div}\,\mathbf{E} = 4\pi q, \quad (5)$$

$$\frac{\partial n}{\partial t} + \mathrm{div}(\mathbf{v}n) = 0, \quad (6)$$

$$\mathbf{E} + \frac{1}{c}[\mathbf{vH}] = 0. \quad (7)$$

These equations do not include the gravitational field of the central source and the thermal plasma pressure, because their effects have already been well studied and are not the subject of this paper.

* E-mail address for contacts: bogoval@axpk40.mephi.ru

1063-7737/01/2703-0176$21.00 © 2001 MAIK "Nauka/Interperiodica"

For steady-state rotation and steady plasma flow, when all parameters vary periodically, the change in arbitrary vector **A** is described by the relation (Beskin *et al.* 1983)

$$\frac{\partial \mathbf{A}}{\partial t} = [\mathbf{\Omega A}] - ([\mathbf{\Omega r}]\nabla)\mathbf{A}.$$

It thus follows that the equality

$$\frac{\partial \mathbf{H}}{\partial t} = \mathrm{curl}[[\mathbf{\Omega r}]\mathbf{H}]$$

holds for the magnetic field.

Hence, using the induction Eq. (2), we find that

$$\mathbf{E} = -[\boldsymbol{\beta}\mathbf{H}], \quad (8)$$

where $\boldsymbol{\beta} = \frac{1}{c}[\mathbf{\Omega r}]$, if the frozen-in condition is satisfied throughout the entire magnetosphere and in the central source (Beskin *et al.* 1983).

THE MODEL OF A ROTATOR WITH A QUASI-MONOPOLE NONUNIFORM MAGNETIC FIELD

The model of an axisymmetric rotator with a monopole-type magnetic field has been widely used to study the collimation and acceleration of plasma in the rotating field of a central source (Michel 1969; Sakurai 1985; Bogovalov 1992; Beskin *et al.* 1998; Bogovalov and Tsinganos 1999; Tsinganos and Bogovalov 2000). This model is convenient because it contains no regions with closed field lines, which considerably simplifies an analysis of the plasma flow. The solution for the problem of plasma flow in an initially dipole magnetic field confirms that the presence of closed field lines adds nothing new to the magnetocentrifugal plasma acceleration in the case of axisymmetric dipole rotation (Contopoulos *et al.* 1999).

Here, our main goal is to answer the question of how azimuthal magnetic-field nonuniformity affects the plasma acceleration. The flow of magnetized plasma is described by the system of nonlinear Eqs. (1)–(7). An attempt to solve the problem on the magnetospheric structure of an oblique rotator with a dipole magnetic field was made by Beskin *et al.* (1983) in the approximation of massless plasma. However, this approximation does not allow the plasma acceleration to be studied, which can be done in the MHD approximation. Generally, in the most interesting cases, the problem of plasma dynamics can be solved in the MHD approximation only numerically. Occasionally, however, the problem can be solved self-consistently and analytically if we are interested in small corrections to the known solution. In particular, small corrections can arise when the known flow from a nonrotating central source is perturbed as the source slowly rotates. This approach was first used to numerically solve the problem of the solar-wind flow (Nurney and Suess 1975). Subsequently (Bogovalov 1992), we used this approach to solve the problem of cold relativistic plasma outflow from a slowly rotating star. In recent years, this method has also been successfully used by Beskin [see Beskin and Okamoto (2000) and references therein]. The idea of this study is also based on the perturbation method. It involves the following. If azimuthal magnetic-field nonuniformity actually somehow affects the magnetocentrifugal plasma acceleration, then this effect can show up even when the central source rotates slowly. Therefore, to answer the question posed here, whether azimuthal magnetic-field nonuniformity changes the plasma acceleration, it may be suffice to consider the acceleration for a slowly rotating source.

PLASMA ACCELERATION FOR A SLOWLY ROTATING SOURCE

Axisymmetric Magnetic Field

Let us first consider some basic properties of the plasma flow in an axisymmetric magnetic field for a slowly rotating central source. The steady-state solution of this problem can be expanded in terms of powers of the central source's angular velocity Ω. Since the problem is azimuthally symmetric, the expansions of the poloidal magnetic field, plasma density, poloidal velocity, and plasma Lorentz factor must contain only even powers of Ω. By contrast, only odd powers of Ω must remain in the expansions of the toroidal magnetic field and the toroidal velocity, because these quantities change their sign as the sense of stellar rotation reverses. Therefore, the steady-state axisymmetric solution can generally be expanded in terms of powers of Ω as follows:

$$\mathbf{H}_\mathrm{p} = \mathbf{H}_{\mathrm{p},0} + \Omega^2\mathbf{H}_{\mathrm{p},2} + \ldots,$$

$$H_\varphi = \Omega H_{\varphi,1} + \Omega^3 H_{\varphi,3} + \ldots,$$

$$\mathbf{v}_\mathrm{p} = \mathbf{v}_{\mathrm{p},0} + \Omega^2\mathbf{v}_{\mathrm{p},2} + \ldots,$$

$$v_\varphi = \Omega v_{\varphi,1} + \Omega^3 v_{\varphi,3} + \ldots,$$

$$n = n_0 + \Omega^2 n_2 + \ldots,$$

$$\gamma = \gamma_0 + \Omega^2\gamma_2 + \Omega^4\gamma_4 + \ldots.$$

Here, the subscripts "0" and "p" denote the variables for a nonrotating central source and the poloidal vector component, respectively. In the special case of plasma flow in a quasi-monopole magnetic field, the first corrections to the azimuthal magnetic field and the azimuthal velocity are (Bogovalov 1992)

$$H_{\varphi,1} = -H_{\mathrm{p},0}\frac{r\sin\theta}{c}, \quad v_{\varphi,1} = 0, \quad (9)$$

where

$$H_{p,0} = H_*\left(\frac{r_*}{r}\right)^2 \quad (10)$$

is the field of the magnetic quasi-monopole. An asterisk denotes the values on the stellar surface. It follows from Eq. (9) that the first corrections to the energy begin with the terms proportional to Ω^4. Indeed, the equation for the plasma Lorentz factor is (Landau and Lifshitz 1973)

$$mnc^2\left(\frac{\partial\gamma}{\partial t} + (\mathbf{v}\nabla)\gamma\right) = \mathbf{jE}. \quad (11)$$

According to this equation, the second-order corrections in Ω to the plasma Lorentz factor are

$$mn_0c^2v_0\Omega^2\frac{\partial}{r}\gamma_2 = \frac{r\Omega\sin\theta}{4\pi}H_{p,0}\frac{\partial}{r\partial r}(rH_{\varphi,1}).$$

However, it follows from Eqs. (9) and (10) that the right part of this relation is equal to zero, implying that $\gamma_2 = 0$. Thus, the first correction to the Lorentz factor begins with the terms proportional to Ω^4; this reflects the fact that, in the axisymmetric case, the magnetocentrifugal acceleration is highly inefficient.

Acceleration in an Azimuthally Nonsymmetric Magnetic Field

The energy of the plasma flowing in a rotating, azimuthally nonsymmetric magnetic field is no longer invariant with respect to a change in the sense of rotation. In this case, energy can (but, generally, does not) depend on the sign of Ω. Therefore, the expansion of the solution takes a more general form:

$$\gamma = \gamma_0 + \Omega\gamma_1 + \Omega^2\gamma_2 + \Omega^3\gamma_3 + \ldots.$$

In the axisymmetric case, $\gamma_1 = \gamma_2 = \gamma_3 = 0$. If $\gamma_1 \neq 0$ in an azimuthally nonsymmetric flow, then this implies that the plasma acceleration in a nonaxisymmetric magnetic field is considerably more efficient than it is in an axisymmetric one. To make sure that γ_1 is actually nonzero, it will suffice to show that $\gamma_1 \neq 0$ when the magnetic field deviates only slightly from azimuthal symmetry. This problem can be solved analytically.

Plasma Flow in a Slightly Nonaxisymmetric Magnetic Field for $\Omega = 0$

Before solving the problem of a rotating nonuniform magnetosphere, it is useful first to consider a plasma flow in the nonuniform field of a nonrotating star. It follows from Eq. (11) that the energy of the cold plasma is constant in such a flow, because $\mathbf{E} = 0$ everywhere. For a slightly azimuthally nonsymmetric magnetic field, the solution can be expanded in terms of some small parameter ε, which characterizes the deviation of the magnetic field from the initial quasi-monopole field. The expansion is

$$\mathbf{H}_p = \mathbf{H}_{p,0} + \varepsilon\mathbf{h}_{p,1} + \ldots,$$

$$H_\varphi = \varepsilon h_{\varphi,1} + \varepsilon^2 h_{\varphi,2} + \ldots,$$

$$\mathbf{v}_p = \mathbf{v}_{p,0} + \varepsilon\mathbf{V}_{p,1} + \varepsilon^2\mathbf{V}_{p,2} + \ldots,$$

$$v_\varphi = \varepsilon V_{\varphi,1} + \varepsilon^2 V_{\varphi,2} + \ldots,$$

$$n = n_0 + \varepsilon\tilde{n}_1 + \ldots,$$

but

$$\gamma = \gamma_0,$$

because the energy is constant for $\Omega = 0$. It is convenient to consider the perturbation of a plasma flow in a quasi-monopole magnetic field, which arises in a slightly azimuthally nonsymmetric distribution of the normal field component on the stellar surface. For simplicity, we assume the perturbed field to have its own symmetry axis **m**. In this case, it is convenient to solve the problem in a coordinate system, in which the magnetic field is azimuthally symmetric, and then to pass to the laboratory coordinate system, in which the symmetry axis is inclined to the Z axis at some angle α. The equation for the first correction to the plasma velocity follows from equations of motion (1). In a spherical coordinate system, in which the Z' axis is the symmetry axis of the magnetic field, this equation is

$$mn_0\gamma_0v_0\frac{\partial rV_{\chi,1}}{r\partial r} = \frac{H_0}{4\pi}\left(\frac{\partial rh_{\chi,1}}{r\partial r} - \frac{\partial h_{r,1}}{r\partial\chi}\right),$$

where χ is the polar angle. It is convenient to introduce such the function ψ, and that the components of the poloidal magnetic field are expressed in terms of this function as

$$H_\chi = -\frac{1}{r\sin\chi}\frac{\partial\psi}{\partial r}, \quad H_r = \frac{1}{r\sin\chi}\frac{\partial\psi}{r\partial\chi}. \quad (12)$$

In this case, the magnetic field automatically satisfies the condition of flux conservation $\mathrm{div}\,\mathbf{H} = 0$.

The expansion of ψ in terms of powers of ε is

$$\psi = H_*R_*^2(1 - \cos\chi + \varepsilon f(\mathbf{r}) + \ldots).$$

Since, in view of the frozen-in condition, $\mathbf{v} = v\mathbf{H}/H$, we derive the following equation for the first correction f from Eq. (12) (Bogovalov 1992):

$$f_{rr} + \frac{2}{r}f_r = \left(\frac{R_a}{r}\right)^2\left(f_{rr} + \frac{(1-\eta^2)}{r^2}\frac{\partial^2 f}{\partial^2\eta}\right),$$

where $\eta = \cos\chi$ and $R_a = \sqrt{H_*^2R_*^2/4\pi mn_*\gamma_0v_0^2}$ is the Alfvén radius of the unperturbed flow. The perturbation f can be expanded,

$$f = \sum_m f_m(r)Q_m(\eta)$$

in terms of eigenfunctions Q_m of the differential equation $(1-\eta^2)\partial^2 Q_m/\partial^2\eta = -m(m+1)Q_m$. These functions are $Q_m(\eta) = (1-\eta^2)\partial P_m(\eta)/\partial\eta$, where P_m are Legendre polynomials of the mth order.

For f_m, we derive the equation

$$(x^2-1)\frac{d^2 f_m}{d^2 x} + 2x\frac{d f_m}{dx} + \frac{m(m+1)}{x^2} f_m = 0, \quad (13)$$

where $x = r/R_a$. The general solution of this equation is a linear superposition, $f_m = a_m Z_m(x) + b_m Y_m(x)$, of two independent solutions: one (Z_m) is regular at point $x = 1$, and the other (Y_m) is singular at this point. The condition of flow regularity at point $x = 1$ implies that $b_m = 0$. The regular solution of Eq. (13) is $Z_m(x) = P_m(1/x)$ (Bogovalov 1992). Therefore, the first correction to the spherically-symmetric solution is

$$f = \sum_m a_m P_m(1/x) Q_m(\eta). \quad (14)$$

The numerical coefficients a_m are determined by the boundary conditions on the stellar surface.

To study the effect of magnetic-field nonuniformity on plasma acceleration, it would be reasonable to take only one term from the expansion (14), which corresponds to the simplest form of nonuniformity in the magnetic-field distribution on the stellar surface. It is of particular interest to consider nonuniformity, for which the magnetic-field strength increases at the magnetic poles and decreases at the magnetic equator, as is the case for a magnetic dipole. The term with $m = 2$ corresponds to this distribution. In this case, the correction to the solution is

$$f = \frac{(3/x^2 - 1)}{(3/x_*^2 - 1)}\sin^2\chi\cos\chi.$$

Accordingly, the corrections to the magnetic field are

$$h_{\chi,1} = \frac{6H_* R_*^2}{R_a^2 x^4 (3/x_*^2 - 1)}\sin\chi\cos\chi,$$

$$h_{r,1} = \frac{(3/x^2 - 1)H_* R_*^2}{r^2(3/x_*^2 - 1)}(2\cos^2\chi - \sin^2\chi).$$

We thus see that the perturbation of the radial magnetic field is positive at the magnetic poles (for $\varepsilon > 0$) and negative at the magnetic equator. This solution reveals an interesting feature of supersonic plasma flows. The perturbation of the radial magnetic field decreases with distance as r^{-2}. The distance dependence of the initial magnetic field is the same. This means that the perturbed flow in the limit $r \longrightarrow \infty$ ceases to be spherically symmetric, although it remains radial. The reason is that the plasma is cold and the magnetic forces fall off with distance so rapidly, that the pressure disbalance across the magnetic field lines cannot change the trajectory of each individual plasma particle, and in such a way that the flow becomes spherically isotropic. At large distances, the plasma motion is purely ballistic.

After finding the solution in the coordinate system, in which the symmetry axis of the magnetic field is along the Z' axis coincident with **m**, we may pass to the laboratory coordinate system, where the magnetic-field symmetry axis is inclined to the Z axis at some angle α. Standard formulas for the transformation of an arbitrary vector **A** from one spherical coordinate system to another yield the relations

$$A_r = A'_r,$$

$$A_\theta = \frac{A'_\chi(\cos\alpha\sin\theta - \sin\alpha\cos\theta\cos\varphi) - A'_\varphi\sin\varphi\sin\alpha}{\sin\chi},$$

$$A_\varphi = \frac{A'_\varphi(\cos\alpha\sin\theta - \sin\alpha\cos\theta\cos\varphi) + A'_\chi\sin\varphi\sin\alpha}{\sin\chi}.$$

The equation that relates the coordinates in these two systems is

$$\cos\chi = \sin\alpha\sin\theta\cos\varphi + \cos\alpha\cos\theta,$$

where θ and φ are, respectively, polar and azimuth angles in the laboratory (unprimed) coordinate system. In the primed coordinate system, the Z' axis is along the symmetry axis of the magnetic field.

For clarity, we are concerned below with the limiting case of a flow in the equatorial plane ($\theta = \pi/2$) of an orthogonal rotator ($\alpha = \pi/2$). The relation between the vector components is particularly simple:

$$A_\theta = -A'_\chi\frac{\cos\theta\cos\varphi}{\sqrt{1-\sin^2\theta\cos^2\varphi}},$$
$$A_\varphi = A'_\chi\frac{\sin\varphi}{\sqrt{1-\sin^2\theta\cos^2\varphi}} \quad (15)$$

provided that $A'_\varphi = 0$.

Plasma Acceleration in a Slightly Nonaxisymmetric Magnetic Field

For slow rotation and slight axial asymmetry, a steady flow can be expanded in terms of two small parameters Ω and ε as follows:

$$\mathbf{H}_p = \mathbf{H}_{p,0} + \varepsilon\mathbf{h}_{p,1} + \ldots,$$

$$H_\varphi = \Omega H_{\varphi,1} + \varepsilon h_{\varphi,1} + \ldots,$$

$$\mathbf{v}_p = \mathbf{v}_{p,0} + \varepsilon\mathbf{V}_{p,2} + \ldots,$$

$$v_\varphi = \varepsilon V_{\varphi,3} + \ldots,$$

$$n = n_0 + \varepsilon n_1 + \ldots,$$

$$\gamma = \gamma_0 + \varepsilon\Omega\delta\gamma + \ldots.$$

It follows from Eq. (11) that $\delta\gamma$ satisfies the equation

$$mn_0c^2\Omega\varepsilon v_0\frac{\partial\delta\gamma}{\partial r} = E_\theta j_\theta, \quad (16)$$

where

$$j_\theta = \varepsilon\frac{c}{4\pi}\left(\frac{1}{r\sin\theta}\frac{\partial h_{r,1}}{\partial\varphi} - \frac{\partial}{r\partial r}rh_{\varphi,1}\right)$$

and E_θ is given by expression (8). Let us calculate $\delta\gamma$ in the special case of an orthogonal rotator ($\alpha = \pi/2$) and a flow in the equatorial plane ($\theta = \pi/2$). Transforming the solution Eq. (15) to the laboratory coordinate system yields

$$j_\theta = \frac{c}{4\pi}\frac{6\varepsilon H_* R_*^2\sin\varphi\cos\varphi}{r^3(3/x_*^2 - 1)}. \quad (17)$$

Integrating Eq. (16) using Eq. (17) yields

$$\gamma = \gamma_0 - \gamma_0\frac{\Omega R_*}{c}\frac{v_0}{c}\frac{6\varepsilon\sin\varphi\cos\varphi}{(3 - x_*^2)}.$$

This result shows that, when the magnetic field is axially nonsymmetric, the magnetocentrifugal plasma acceleration is significantly modified for a slowly rotating source. In an axisymmetric magnetic field, the first corrections to the plasma energy begin with the terms proportional to Ω^4, whereas even slight axial asymmetry of the magnetic field makes this dependence considerably stronger. The first corrections become proportional to Ω.

DISCUSSION

Here, we have suggested that axial asymmetry of the magnetic field can significantly modify the magnetocentrifugal plasma acceleration. We managed to prove the validity of this suggestion, at least for a slowly rotating source. The acceleration in a nonaxisymmetric magnetic field actually differs markedly from the acceleration in an axisymmetric magnetic field. It becomes more efficient. In essence, this implies that the propeller effect, which was proposed by Illarionov and Sunyaev (1975) as a possible ejection mechanism of the plasma accreting onto a neutron star, is important for the acceleration. We see that the propeller effect determines not only the ejection, but also the acceleration of plasma. In our model, the plasma is accelerated due to the magnetic-field nonuniformity alone, i.e., due to the propeller effect.

So far, we have been able to study the role of this effect only for a slowly rotating central source. How the plasma will be accelerated in a rapidly rotating object and for a highly nonuniform magnetic field is still an open question. This question can apparently be answered only by three-dimensional numerical simulations of plasma flow in nonaxisymmetric magnetic fields. However, it is clear that if the detected effect will also takes place for rapid rotation, it will primarily be of importance in solving the problem of relativistic wind acceleration in pulsar magnetospheres.

ACKNOWLEDGMENTS

This work was supported in part by the program of the Ministry of Education of the Russian Federation "Universities of Russia: Fundamental Studies" (project no. 990479).

REFERENCES

1. A. I. Akhiezer, I. A. Akhiezer, R. V. Polovin, A. G. Sitenko, and K. N. Stepanov, *Plasma Electrodynamics* (Pergamon, Oxford, 1975), Vol. 1.
2. V. S. Beskin and I. Okamoto, Mon. Not. R. Astron. Soc. **313**, 445 (2000).
3. V. S. Beskin, A. V. Gurevich, and Ya. N. Istomin, Zh. Éksp. Teor. Fiz. **85**, 401 (1983) [Sov. Phys. JETP **58**, 235 (1983)].
4. V. S. Beskin, I. V. Kuznetsova, and R. R. Rafikov, Mon. Not. R. Astron. Soc. **299**, 341 (1998).
5. R. D. Blandford and D. G. Payne, Mon. Not. R. Astron. Soc. **199**, 883 (1982).
6. S. V. Bogovalov, Astron. Astrophys. **327**, 662 (1997).
7. S. V. Bogovalov, Astron. Astrophys. **349**, 1017 (1999).
8. S. V. Bogovalov, Astron. Astrophys. (2000).
9. S. V. Bogovalov, Pis'ma Astron. Zh. **18**, 832 (1992) [Sov. Astron. Lett. **18**, 337 (1992)].
10. S. V. Bogovalov and K. Tsinganos, Mon. Not. R. Astron. Soc. **305**, 211 (1999).
11. I. Contopoulos, D. Kazanas, and C. Fendt, Astrophys. J. **511**, 351 (1999).
12. A. F. Illarionov and R. A. Sunyaev, Astron. Astrophys. **39**, 185 (1975).
13. L. D. Landau and E. M. Lifshitz, *The Classical Theory of Fields* (Nauka, Moscow, 1973; Pergamon, Oxford, 1975).
14. F. C. Michel, Astrophys. J. **158**, 727 (1969).
15. S. F. Nurney and J. Suess, Astrophys. J. **196**, 837 (1975).
16. T. Sakurai, Astron. Astrophys. **152**, 121 (1985).
17. K. Tsinganos and S. V. Bogovalov, Astron. Astrophys. **356**, 989 (2000).

Translated by G. Rudnitskii

Astronomy Letters, Vol. 27, No. 3, 2001, pp. 181–185. Translated from Pis'ma v Astronomicheskiĭ Zhurnal, Vol. 27, No. 3, 2001, pp. 215–219.

Observations of Bright Coronal Points at Wavelengths of 5.2 and 1.76 cm

V. P. Maksimov*, D. V. Prosovetskiĭ, and B. B. Krissinel

Institute for Solar-Terrestrial Physics, Siberian Branch, Russian Academy of Sciences, ul. Lermontova 126, Irkutsk, 664033 Russia

Received March 22, 2000; in final form, August 2, 2000

Abstract—Based on two-dimensional solar images obtained with the Siberian Solar Radio Telescope and the Nobeyama Radio Heliograph and using YOHKOH soft X-ray images, we investigate bright coronal points. The principal microwave emission mechanism of these points is shown to be the thermal bremsstrahlung of an optically thin plasma. The fact that, in several cases, bright coronal points do not coincide at two wavelengths can be explained by imaging peculiarities of the Nobeyama Radio Heliograph rather than by physical factors. *© 2001 MAIK "Nauka/Interperiodica".*

Key words: *Sun*

INTRODUCTION

Since the first detection of bright X-ray points by Van Speybroek *et al.* (1970), numerous studies have been carried out to identify them and to determine their characteristics in various wavelength ranges: XUV (Golub *et al.* 1975, 1976), EUV (Habbal and Withbroe 1981), He I λ10 830 Å (Harvey 1985), microwave emission at 6 cm (Fu *et al.* 1987; Kundu *et al.* 1988), 20 cm (Habbal *et al.* 1986; Kundu *et al.* 1988; Nitta *et al.* 1992), and 1.76 cm (Kundu *et al.* 1994). These studies revealed small-scale features in the emission at various wavelengths with similar sizes, lifetimes, distributions over the disk, and relationships to photospheric magnetic fields. Thus, bright points are vertically extended structures, which is reflected in the current use of a broader term for them—bright coronal points. At the same time, an analysis of simultaneous observations at various wavelengths does not give a close correspondence between bright points. Apart from close coincidences, there are points that are visible at one wavelength but are lacking at another wavelength. It is unclear whether noncoincidences reflect the actual peculiarities of the vertical structure of bright coronal points or they are attributable to the fact that observations are not simultaneous and that these features located above ephemeral active regions, faculae, in areas of the quiet Sun or in coronal holes differ in properties. Elucidating these circumstances is of great importance in understanding the physical nature of bright coronal points. A major method of solving this problem is to perform a comparative analysis of their properties over the widest possible wavelength range.

Here, we discuss the results of our comparative analysis of the microwave emission from bright coronal points by using data from the Siberian Solar Radio Telescope (SSRT) and the Nobeyama Radio Heliograph (NoRH).

OBSERVATIONS

The SSRT (5.2-cm wavelength) is a cross-shaped interferometer of 256 2.5-m antennas spaced at 4.9 m in the east west and north south directions. Basic SSRT parameters and imaging methods are given by Smolkov *et al.* (1986) and Krissinel *et al.* (2000). In the radio maps used here, the spatial resolution was ~21″. The NoRH (1.76-cm wavelength) is a T-shaped interferometer of 84 80-cm antennas with a spatial resolution of 10″ (Nishio *et al.* 1994).

For our analysis, we chose SSRT and NoRH solar radio images on June 1–6, 8–9, 14–17, and 20–26, on July 5, 7, 8, 17, 18, and 20, and on October 13–15, 18, and 20, 1996. We used SSRT observations between 02:00 and 04:00 UT. In this interval, one radio image of the entire Sun was obtained over a period from 24 min to 1 h. The time it took to obtain a NoRH radio image was 1 s, and we chose one map from 02:00 until 03:00 UT for our analysis.

The observing periods we chose were characterized by low solar activity. As a result, the SSRT maps exhibited virtually no traces of side lobes, which allowed the image reconstruction procedure to be avoided. It should be noted that, in this case, the SSRT spatial resolution is comparable to the VLA spatial resolution at 20 cm after image cleaning.

* E-mail address for contacts: maksimov@iszf.irk.ru

1063-7737/01/2703-0181$21.00 © 2001 MAIK "Nauka/Interperiodica"

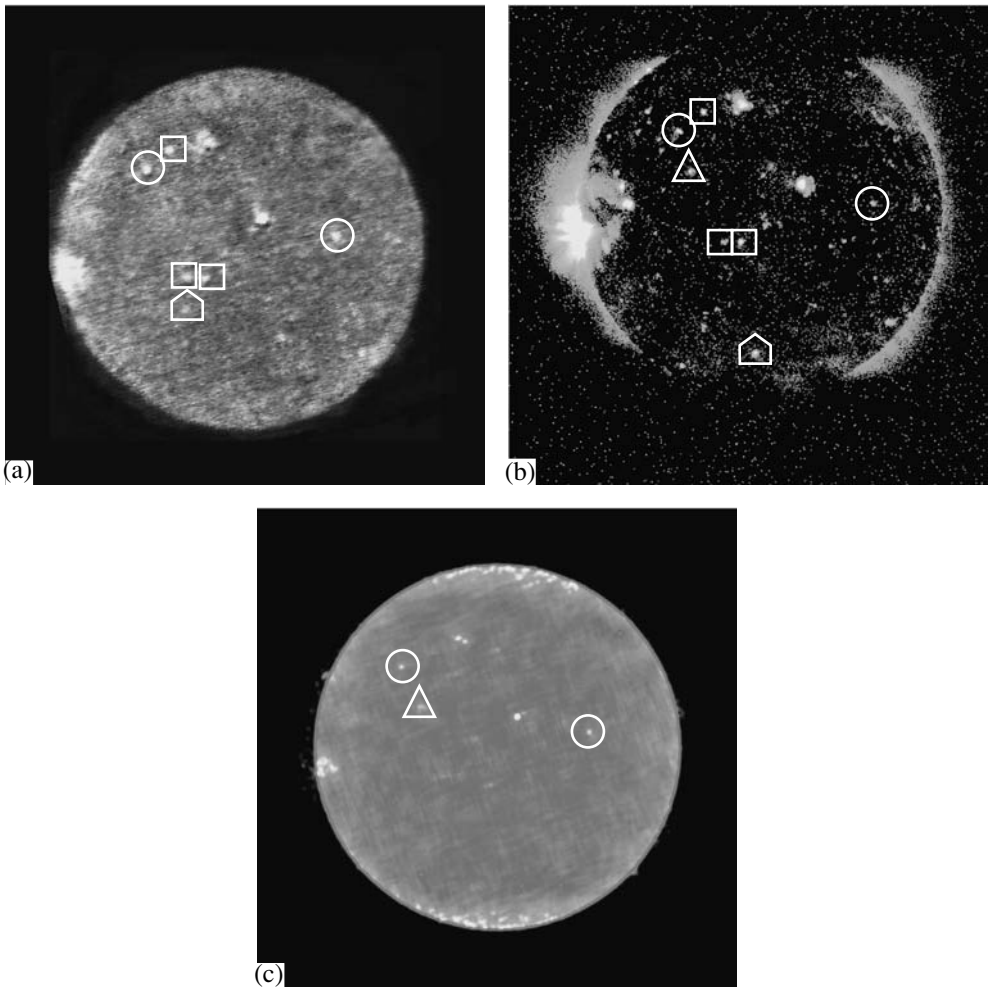

Fig. 1. Microwave [(a) SSRT 02:09 UT and (c) NoRH 02:08 UT] and soft X-ray [(b) YOHKOH 13:35 UT] images of the Sun on June 3, 1996. The bright coronal points existing in all three images (circles), in two images [YOHKOH and SSRT (squares), YOHKOH and NoRH (triangles)], and only in one image (pentagon) are highlighted.

Solar images in the soft X-ray band from YOHKOH, and in the Fe XII λ195 Å line from SOHO EIT taken from the SOHO archive, were used to identify coronal points.

ANALYSIS

Following Golub *et al.* (1989), we selected bright coronal points by visually examining images using the sizes and intensities of isolated structures as the criteria. Based on the structure sizes and intensities, we arbitrarily chose an upper limit of 2 arcmin and established limits on the excess of the quiet-Sun level (from a factor of 1.3 to a factor of 4), respectively. Given the finite lifetimes of coronal points, structures with lifetimes of no less than a day were selected.

Table 1. Coincidences of bright X-ray and microwave points (number of events)

	SXT	SSRT	NoRH
SXT	57	52	13
SSRT	52	68	22
NoRH	13	22	46

As an example, the Fig. 1 shows the microwave (a, c) and soft X-ray (b) solar images on June 3, 1996, in which bright coronal points are highlighted. We see from the figure that there are points visible in all three images, in two images, and only in one image. A total of 68, 46, and 57 bright coronal points were identified in the SSRT, NoRH, and SXT YOHKOH images, respectively. Their mutual coincidences and noncoincidences at three wavelengths are listed in Tables 1 and 2.

Bright coronal points in the SSRT images exhibit no fine structures, and their sizes range from 25″ to 93″ with a mean of 60″. In the NoRH images, the sizes of bright coronal points range from 10″ to 59″, with a mean of 36″. Bright X-ray points in the YOHKOH images have sizes in the range 10″ to 45″. In two cases, bright

coronal points were observed above the limb, which allowed their heights to be determined. The centers of bright coronal points lay at heights of 2800 and 5600 km, as inferred from the NoRH data, and at 9700 and 18 100 km, as inferred from the SSRT data.

Thus, our analysis also revealed noncoincidences of bright coronal points at different wavelengths, as noted in the Introduction. Harvey (1985) and Kundu *et al.* (1988) gave the following reasons for these noncoincidences: nonsimultaneous imaging at various wavelengths, finite lifetimes of bright coronal points, and rapid variations in their intensities and positions (Harvey 1985; Kundu *et al.* 1988). On the other hand, we paid special attention to the possible absence of microwave points above weak X-ray points, because of the lower sensitivity of radio images (Nitta *et al.* 1992). In the events studied, the SSRT data revealed no correlation between the intensity of a bright coronal point and the existence of its microwave counterpart: we noted cases where there were no radio points above very bright X-ray points and where there were radio points above very weak X-ray points.

At the same time, as we see from Table 2, bright points at 1.76 cm poorly correspond to their counterparts both at 5.2 cm and in the soft X-ray band. Therefore, the distribution of brightness temperatures for coronal points should be considered in more detail by using SSRT and NoRH data. If thermal bremsstrahlung of an optically thin plasma is assumed to be responsible for the microwave emission, then the brightness temperature is given by (Kundu *et al.* 1988)

$$T_\mathrm{b} = \frac{0.2 N_e^2 L}{T^{1/2} f^2},$$

where N_e is the electron density, f is the frequency of observations, and L is the path length along the line of sight. In this case, the ratio of brightness temperatures at two wavelengths is equal to the ratio of the squares of these wavelengths: $T_\mathrm{b}(1.76)/T_\mathrm{b}(5.2) = 0.112$. Table 3 lists measured brightness temperatures T_b and ratios of the "true" brightness temperatures T_b' for the coronal points observed with the SSRT and NoRH. The "true" brightness temperature was assumed to be equal to the difference between the measured temperature of a bright coronal point and the brightness temperature of the quiet Sun (16 000 and 10 000 K for wavelengths of 5.2 and 1.76 cm, respectively). For the two points (marked by an asterisk in Table 3) observed at the limb, the "true" brightness temperature was taken to be the measured brightness temperature. The mean ratio of brightness temperatures for the entire set of coronal points, 0.108, is fairly close to its calculated value, 0.112. In this case, the mean ratio of brightness temperatures was 0.115 ± 0.004 for 50% of the points; the ratios of brightness temperatures for the other half of the points differed markedly from 0.112. For seven coronal points from the last group, the measured brightness temperatures at 1.76 cm were less than 12 000 K. Since the NoRH images were obtained by using the CLEAN threshold (3000 K), the brightness-temperature determination in the range 10 000–13 000 K can be assumed to be inaccurate. In order to test this assumption, for 30 bright points visible with the SSRT, but without any counterparts in the NoRH observations, we calculated the brightness temperatures that these points would have at 1.76 cm under the assumption of thermal bremsstrahlung from an optically thin plasma. According to the SSRT data, the brightness temperatures of these points were distributed over the range 28 577–56 900 K with a mean of 40 566 ± 1470 K. The calculated mean brightness temperature of these points at 1.76 cm was 12 751 ± 165 K; i.e., the mean temperature

Table 2. Noncoincidences of bright X-ray and microwave points (number of events)

	SXT	SSRT	NoRH
SXT		5	44
SSRT	16		46
NoRH	33	24	

Table 3. Brightness temperatures of bright coronal points at 1.76 and 5.2 cm

No.	$T_\mathrm{b}(5.2)$, K	$T_\mathrm{b}(1.76)$, K	$T_\mathrm{b}'(1.76)/T_\mathrm{b}'(5.2)$
1	60444	15156	0.116
2	61782	16000	0.131
3	42408	12315	0.088
4	71624	17000	0.126
5	40026	11200	0.050
6	32653	11000	0.060
7	118571	22000	0.117
8	79431	18000	0.126
9	70885	20000	0.182
10	25065	11737	0.192
11	78730	18000	0.128
12	103000	24000	0.161
13*	69271	17600	0.254
14	71769	11594	0.029
15	74000	11800	0.031
16*	106000	12600	0.119
17	56000	13700	0.093
18	52515	11899	0.052
19	50622	11500	0.043
20	44146	12800	0.099
21	65503	12900	0.059
22	34324	12176	0.119

Table 4. Comparative characteristics of bright coronal points at various radio wavelengths

Observations	T_b', K	Size, arcsec	B, G	P_0^2/Fc, $K^2/erg\ cm^4\ s$	Height, km
NoRH 1.76 cm	0.57×10^4	10″–59″		$(0.84–8.5) \times 10^{24}$	$(2.8–5.6) \times 10^3$
SSRT 5.2 cm	2.45×10^4	25″–93″		$(0.41–4.23) \times 10^{24}$	$(1–1.8) \times 10^4$
VLA 6 cm	$(0.5–4) \times 10^4$	5″–16″	40–400	$(0.5–1.1) \times 10^{24}$	$(1.5–2) \times 10^4$
VLA 20 cm	$(0.5–5) \times 10^5$	3″–40″	50–200	2×10^{24}	

difference between coronal points and the quiet Sun at this wavelength was 2751 K, which is below the CLEAN threshold. Thus, we conclude that the absence of counterparts at 1.76 cm for bright coronal points at 5.2 cm may result from a reduction in sensitivity due to the use of the CLEAN procedure when constructing a radio map.

It is of interest to compare our results at 1.76 and 5.2 cm with those obtained from VLA observations of bright coronal points at 6 and 20 cm (Habbal *et al.* 1986; Kundu *et al.* 1988). In order to compare nonsimultaneous observations at these wavelengths, Habbal *et al.* (1986) proposed to use a relationship between the polarization of microwave emission, the magnetic-field strength and direction in the source, the gas pressure, and the heat flux. Assuming free-free emission, they derived an expression that allows the magnetic-field strength in the source to be estimated from measured brightness temperatures of the ordinary and extraordinary emission modes. In our cases, we failed to clearly distinguish the polarized emission component in bright coronal points. This is apparently because the SSRT spatial resolution is not high enough, which may result in a decrease in the brightness temperature of polarization sources with sizes considerably smaller than the beam size and in the addition of the responses from structural elements of a bright coronal point with opposite signs of polarization. Both these factors can significantly reduce the possibility of recording the polarized emission from a bright coronal point. However, the expressions derived by Habbal *et al.* (1986) allow us to determine the wavelength-independent ratio of the square of gas pressure P_0^2 to the heat flux F_c:

$$\frac{P_0^2}{F_c} = \frac{T_b'}{T_{max} - T_b'} \times \frac{(2\pi f)^2}{7.7 \times 10^{-6}},$$

where T_{max} is the coronal temperature. Taking $T_{max} = 10^6$ K for a point in the corona and $T_{max} = 10^7$ K for a point in an arch and substituting the observed mean true brightness temperature $T_b' = 2.45 \times 10^4$ K for the SSRT (the mean for all observed points) and 0.57×10^4 K for the NoRH (the mean for the points whose brightness temperatures were above the CLEAN threshold), we obtained $P_0^2/F_c = (0.41–4.23) \times 10^{24}$ $K^2\ erg^{-1}\ cm^{-4}\ s^{-1}$ and $(0.84–8.5) \times 10^{24}$ $K^2\ erg^{-1}\ cm^{-4}\ s^{-1}$, respectively. As we see from Table 4, the inferred values agree in order of magnitude with those determined for 6 and 20 cm (Habbal *et al.* 1986; Fu *et al.* 1987; Kundu *et al.* 1988) from VLA observations.

CONCLUSION

Our analysis of bright coronal points and comparison with previous results have shown the following:

(1) The most likely emission mechanism of bright coronal points over a wide wavelength range, from 1.76 to 20 cm, is the thermal bremsstrahlung of an optically thin plasma.

(2) The absence of counterparts at 1.76 cm for bright coronal points at 5.2 cm is attributable to a reduction in sensitivity due to the use of the CLEAN procedure to construct a NoRH radio map.

ACKNOWLEDGMENTS

This study was supported by the Ministry of Science and Technology of the Russian Federation, the Siberian Branch of the Russian Academy of Sciences, the Federal Program “Astronomy,” and the INTAS-RFBR (project no. IR 97-1088). We wish to thank the NoRH and YOHKOH/SXT staffs for providing the data used here and the critic for helpful remarks.

REFERENCES

1. Q. Fu, M. R. Kundu, and E. J. Schmahl, Sol. Phys. **108**, 99 (1987).
2. L. Golub, A. S. Krieger, and G. S. Vaiana, Sol. Phys. **42**, 131 (1975).
3. L. Golub, A. S. Krieger, and G. S. Vaiana, Sol. Phys. **49**, 79 (1976).
4. L. Golub, K. L. Harvey, M. Herant, and D. F. Webb, Sol. Phys. **124**, 211 (1989).
5. S. R. Habbal and G. L. Withbroe, Sol. Phys. **69**, 77 (1981).
6. S. R. Habbal, R. S. Ronan, G. L. Withbroe, *et al.*, Astrophys. J. **306**, 740 (1986).
7. K. L. Harvey, Aust. J. Phys. **38**, 875 (1985).

8. B. B. Krissinel', S. M. Kuznetsova, V. P. Maksimov, *et al.*, Izv. Akad. Nauk, Ser. Fiz. **64**, 1862 (2000).
9. M. R. Kundu, E. J. Schmahl, and Q.-J. Fu, Astrophys. J. **325**, 905 (1988).
10. M. R. Kundu, K. Shibasaki, E. Enome, and N. Nitta, in *Proceedings of Kofu Symposium*, Ed. by S. Enome and T. Hirayama, NRO Report, No. 360, 79 (1994).
11. M. Nishio, H. Nakajima, S. Enome, *et al.*, in *Proceedings of Kofu Symposium*, Ed. by S. Enome and T. Hirayama, NRO Report, No. 360, 19 (1994).
12. N. Nitta, T. S. Bastian, M. J. Aschwanden, *et al.*, Publ. Astron. Soc. Jpn. **44**, L167 (1992).
13. G. Ya. Smolkov, A. A. Pistolkors, B. B. Krissinel, *et al.*, Astrophys. Space Sci. **119**, 1 (1986).
14. L. P. van Speybroek, A. S. Krieger, and G. S. Vaiana, Nature **227**, 818 (1970).

Translated by V. Astakhov

Astronomy Letters, Vol. 27, No. 3, 2001, pp. 186–192. Translated from Pis'ma v Astronomicheskiĭ Zhurnal, Vol. 27, No. 3, 2001, pp. 220–226.

Parametric Generation of Acoustic-Gravity Waves in the Solar Atmosphere

M. Yu. Petukhov and Yu. V. Petukhov*

Institute of Applied Physics, Russian Academy of Sciences, ul. Ul'yanova 46, Nizhniĭ Novgorod, 603600 Russia

Received March 22, 2000

Abstract—Based on a plane isothermal solar-atmosphere model, we investigate the parametric generation of acoustic-gravity waves (AGWs) in the approximation of a fixed field for vertically propagating disturbances. Both nonpropagating and propagating AGWs are shown to be generated at the difference frequency via the nonlinear interaction of primary waves in the frequency range "forbidden" for the propagation of AGWs during their linear generation. An acoustic wind has been found to be formed in the solar atmosphere at zero difference frequency; its velocity increases with height in inverse proportion to the decreasing ambient density. We study the nonlinear generation of AGWs at the second harmonic during the interaction of disturbances from the forbidden frequency range. *© 2001 MAIK "Nauka/Interperiodica".*

Key words: *Sun*

INTRODUCTION

Until now, much attention has been given to the study of the generation and propagation of acoustic-gravity waves (AGWs) in the solar atmosphere (Dubov 1978; Vorontsov and Zharkov 1988; Coroniti *et al.* 1995; Sutmann and Ulmschneider 1995a; Musielak *et al.* 1998). One of the reasons for this interest is the development of generation and formation mechanisms for global radial oscillations in the solar atmosphere (Dubov 1978; Vorontsov and Zharkov 1988; Severnyĭ 1988; Garmash *et al.* 1989; Musielak *et al.* 1998). To this end, a plane atmosphere model (Coroniti *et al.* 1995; Sutmann and Ulmschneider 1995a; Musielak *et al.* 1998) is used most commonly. This model allows the pattern of vertical propagation, at heights much smaller than the solar radius, to be properly described.

As it is well known (Lamb 1947; Eckart 1963), the fact that AGW propagation in the linear approximation is possible only at frequencies above the characteristic Lamb frequency can be explained in terms of a plane isothermal atmosphere model, whereas waves below this frequency are nonpropagating (inhomogeneous). The unquestionable importance of the Lamb frequency in analyzing wave processes in the solar atmosphere stimulated the studies of its height dependence (Fleck and Schmitz 1998). These studies aim to establish the factors whose effect lead to an appreciable decrease in Lamb frequency and, thus, to the possible existence of propagating AGWs in a considerably wider range of low frequencies (Dubov 1978; Fleck and Schmitz 1998).

Naturally, when describing vertical AGW propagation in the atmosphere, we cannot restrict ourselves to the use of the linear theory alone (Coroniti *et al.* 1995; Sutmann and Ulmschneider 1995a; Musielak *et al.* 1998; Fleck and Schmitz 1998), because the oscillation velocity (and, consequently, the Mach number) increases in inverse proportion to the square root of the decreasing ambient density (Lamb 1947; Eckart 1963) as the AGWs propagate into the upper atmosphere. This forces us to take into account nonlinear effects, which give rise to shock waves (Romanova 1970, 1971; Finaudi 1970; Kosovichev and Popov 1979; Uralov 1982; Klimishin 1984; Rammacher and Ulmschneider 1992; Fleck and Schmitz 1993; Bodo *et al.* 1994; Sutmann and Ulmschneider 1995b, Cheng 1996).

It should be noted that, when the influence of nonlinear effects on AGW propagation in a plane atmosphere was studied, the main attention was given to analytic (Romanova 1970, 1971; Finaudi 1970; Uralov 1982; Klimishin 1984) and numerical (Kosovichev and Popov 1979; Klimishin 1984) descriptions of the shock formation and evolution. At the same time, the nonlinear generation of propagating AGWs in the "forbidden" (for them) frequency range below the Lamb frequency detected by several authors (Fleck and Schmitz 1993; Bodo *et al.* 1994; Sutmann and Ulmschneider 1995b) during numerical simulations using the basic system of hydrodynamic equations remained without due attention. This is, in particular, because, except for the methods of direct numerical simulations developed by a number of authors (Kosovichev and Popov 1979; Klimishin 1984; Colella and Woodward 1984), the corre-

* E-mail address for contacts: petukhov@hydro.appl.sci–nnov.ru

sponding problems could not be solved in terms of the analytic methods suggested by Romanova (1970, 1971), Finaudi (1970), and Uralova (1982); the latter properly describe the propagation of only relatively short AGWs with frequencies above the Lamb frequency characteristic of an isothermal atmosphere.

That is why our goal is an approximate analytic description of the parametric generation of AGWs at frequencies below the Lamb frequency for vertical AGW propagation in an isothermal atmosphere at frequencies above the Lamb frequency.

FORMULATION OF THE PROBLEM DERIVATION OF AN APPROXIMATE NONLINEAR EQUATION

Consider the vertical propagation of plane AGWs in a plane isothermal atmosphere $z \geq 0$ with the following height (z) dependences of equilibrium pressure $p_0(z)$ and density $\rho_0(z)$:

$$p_0(z) = \frac{\rho_{00} c_0^2}{\gamma}\exp(-z/H), \quad \rho_0(z) = \rho_{00}\exp(-z/H) \tag{1}$$

and with constant adiabatic speed of sound c_0, adiabatic index γ, Lamb frequency ω_L, and scale height H (Lamb 1947; Eckart 1963):

$$c_0^2 = \gamma p_0/\rho_0, \quad \omega_L = \gamma g/2c_0, \quad H = c_0/2\omega_L. \tag{2}$$

We assume that the z axis is directed vertically upward, opposite to the force of gravity, and that the free-fall acceleration g is constant; $\rho_{00} = \rho_0(z = 0)$ is the gas density at the lower atmospheric boundary.

We also assume that, at $z = 0$, the atmosphere borders an absolutely rigid surface, which undergoes steady-state (in time t) oscillations at frequencies ω_1 and ω_2 with the respective amplitudes A_1 and A_2 of vertical oscillation velocity v:

$$v|_{z=0} = A_1\cos\omega_1 t + A_2\cos\omega_2 t \quad (-\infty < t < +\infty). \tag{3}$$

Let us choose frequencies ω_1 and ω_2 in such a way that the difference frequency $\Omega = \omega_2 - \omega_1$ falls within the frequency range "forbidden" for linear AGW propagation:

$$0 < \Omega < \omega_L, \quad \omega_1 > \omega_L. \tag{4}$$

We consider mainly the basic patterns of nonlinear AGW generation at difference frequency Ω for the conditions (1)–(4), under which the primary waves at frequencies ω_1 and ω_2 are propagating.

To obtain an approximate analytic solution of the problem, we use the well known system of gas-dynamical equations (Lamb 1947; Eckart 1963):

$$\begin{cases} \rho(\partial v/\partial t + v\partial v/\partial z) = -\dfrac{\partial p}{\partial z} - \rho g & (5) \\ \dfrac{\partial \rho}{\partial t} + \dfrac{\partial}{\partial z}(\rho v) = 0 & (6) \\ \dfrac{\partial p}{\partial t} + v\dfrac{\partial p}{\partial z} = \dfrac{\gamma p}{\rho}\left(\dfrac{\partial \rho}{\partial t} + v\dfrac{\partial \rho}{\partial z}\right), & (7) \end{cases}$$

which describe the plane motions of a compressible gas in a gravitational field. Here, $p = p_0 + p'$ is the total pressure; $\rho = \rho_0 + \rho'$ is the total density; p' and ρ' are the pressure and density perturbations, respectively, and v is the vertical oscillation velocity.

From the Euler (5) and continuity (6) equations for the isentropic gas motion Eq. (7), we then derive the following nonlinear equation, to within terms of the second order of smallness in Mach number $M = v/c_0$:

$$\frac{\partial^2 v}{\partial t^2} - c_0^2\frac{\partial^2 v}{\partial z^2} + \gamma g\partial v/\partial z = \gamma\rho_0^{-1}\frac{\partial}{\partial z}(p'\partial v/\partial z) - \frac{\rho'}{\rho_0}\frac{\partial^2 v}{\partial t^2} - 2v\frac{\partial^2 v}{\partial z\partial t} - \frac{\partial v}{\partial t}\frac{\partial v}{\partial z}. \tag{8}$$

The pressure and density perturbations on the right-hand side of this equation are linearly related to the oscillation velocity:

$$\partial p'/\partial t = \rho_0(gv - c_0^2\partial v/\partial z), \tag{9}$$

$$\frac{\partial \rho'}{\partial t} = \rho_0\left(\frac{v}{H} - \partial v/\partial z\right). \tag{10}$$

LINEAR PROPAGATION OF ACOUSTIC-GRAVITY WAVES

As in the well-known book by Rudenko and Soluyan (1975), we seek a solution to Eq. (8) by the method of successive approximations, to within the corresponding quantities of the second order of smallness:

$$v = v^{(1)} + v^{(2)}, \quad p' = p^{(1)} + p^{(2)}, \quad \rho' = \rho^{(1)} + \rho^{(2)}, \tag{11}$$

where $v^{(1)}$, $p^{(1)}$, and $\rho^{(1)}$ and $v^{(2)}$, $p^{(2)}$, and $\rho^{(2)}$ are quantities of the first and second order of smallness, respectively.

In the linear approximation, we derive the following equation for oscillation velocity from Eqs. (8) and (11) (Lamb 1947; Eckart 1963):

$$\frac{\partial^2 v^{(1)}}{\partial t^2} - c_0^2\frac{\partial^2 v^{(1)}}{\partial z^2} + \gamma g\frac{\partial v^{(1)}}{\partial z} = 0. \tag{12}$$

Its solutions for upward propagating and nonpropagating waves with frequency ω and initial amplitude A (at $z = 0$) are

$$v^{(1)} = \begin{cases} A\exp\left[\frac{z}{2H} + i\left(\omega t - \sqrt{\frac{\omega^2}{\omega_L^2} - 1}\frac{z}{2H}\right)\right], & \omega > \omega_L \\ A\exp\left[i\omega t + \left(1 - \sqrt{1 - \frac{\omega^2}{\omega_L^2}}\right)\frac{z}{2H}\right], & \omega < \omega_L. \end{cases} \quad (13)$$

Note that by the solution of Eq. (12), we mean the real part $v_R^{(1)} = \mathrm{Re}\{v^{(1)}\}$ of Eq. (13). Therefore, in view of the boundary condition (3) and using formulas (9), (10), and (13), we obtain the following solutions for the corresponding quantities in the linear approximation:

$$v_R^{(1)} = \exp\left(\frac{z}{2H}\right)\sum_{j=1}^{2} A_j \cos\left(\omega_j t - \sqrt{\frac{\omega_j^2}{\omega_L^2} - 1}\frac{z}{2H}\right), \quad (14)$$

$$p_R^{(1)} = \rho_{00} c_0 \exp\left(-\frac{z}{2H}\right) \times \sum_{j=1}^{2} A_j \left\{\sqrt{1 - \frac{\omega_L^2}{\omega_j^2}}\cos\left(\omega_j t - \sqrt{\frac{\omega_j^2}{\omega_L^2} - 1}\frac{z}{2H}\right) + \frac{2-\gamma}{\gamma}\frac{\omega_L}{\omega_j}\sin\left(\omega_j t - \sqrt{\frac{\omega_j^2}{\omega_L^2} - 1}\frac{z}{2H}\right)\right\}, \quad (15)$$

$$\rho_R^{(1)} = \frac{\rho_{00}}{c_0}\exp\left(-\frac{z}{2H}\right) \times \sum_{j=1}^{2} A_j \left\{\sqrt{1 - \frac{\omega_L^2}{\omega_j^2}}\cos\left(\omega_j t - \sqrt{\frac{\omega_j^2}{\omega_L^2} - 1}\frac{z}{2H}\right) + \frac{\omega_L}{\omega_j}\sin\left(\omega_j t - \sqrt{\frac{\omega_j^2}{\omega_L^2} - 1}\frac{z}{2H}\right)\right\}, \quad (16)$$

where $p_R^{(1)} = \mathrm{Re}\{p^{(1)}\}$ and $\rho_R^{(1)} = \mathrm{Re}\{\rho^{(1)}\}$.

As is well known (Lamb 1947; Eckart 1963), it follows from (14)–(16) that, in propagating linear AGWs, (i) the oscillation velocity amplitude increases with height in inverse proportion to the square root of the decreasing ambient density, while the amplitudes of pressure and density perturbations decrease in direct proportion to this quantity and (ii) the phase relations between $v_R^{(1)}$, $p_R^{(1)}$, and $\rho_R^{(1)}$ are different and depend on ω_L/ω_j ($j = 1, 2$).

NONLINEAR GENERATION OF ACOUSTIC-GRAVITY WAVES AT THE DIFFERENCE FREQUENCY

From Eqs. (8) and (11), we derive the following equation for the quantity $v^{(2)}$ of the second order of smallness:

$$\frac{\partial^2 v^{(2)}}{\partial t^2} - c_0^2\frac{\partial^2 v^{(2)}}{\partial z^2} + \gamma g \partial v^{(2)}/\partial z = \frac{\gamma}{\rho_0}\frac{\partial}{\partial z}(p^{(1)}\partial v^{(1)}/\partial z) - \frac{\rho^{(1)}}{\rho_0}\frac{\partial^2 v^{(1)}}{\partial t^2} - 2v^{(1)}\frac{\partial^2 v^{(1)}}{\partial z \partial t} - \frac{\partial v^{(1)}}{\partial t}\frac{\partial v^{(1)}}{\partial z}. \quad (17)$$

Next, we substitute the linear solutions $v_R^{(1)}$ Eq. (14), $p_R^{(1)}$ Eq. (15), and $\rho_R^{(1)}$ Eq. (16) in the right-hand part of Eq. (17) and separate the term responsible for the generation of the difference frequency in the "driving force." For $v^{(2)}$, we then also derive a linear, but inhomogeneous equation:

$$\frac{\partial^2 v^{(2)}}{\partial t^2} - c_0^2\frac{\partial^2 v^{(2)}}{\partial z^2} + \gamma g\frac{\partial v^{(2)}}{\partial z} = \mathrm{Re}\left\{A_{12}\exp\left[\frac{z}{H} + i(\Omega t - \Delta k_{21} z)\right]\right\}, \quad (18)$$

where, for convenience, we introduced the following quantities:

$$A_{12} = \frac{A_1 A_2}{c_0}\left\{\frac{\gamma(\omega_2\nu_2 - \omega_1\nu_1)}{2}(\omega_1\alpha_2 \times \exp[i(\varphi_{12} - \varphi_{21} - \pi/2)] + \omega_2\alpha_1\exp[i(\varphi_{22} - \varphi_{11} - \pi/2)]) + \frac{\omega_1\omega_2}{2}\left(\exp\left[-i\left(\varphi_{21} + \frac{\pi}{2}\right)\right] - \exp\left[i\left(\varphi_{22} - \frac{\pi}{2}\right)\right]\right) - \omega_1^2\left(\exp[i\varphi_{31}] - \frac{\exp[i\varphi_{32}]}{2}\right) - \omega_2^2\left(\exp[-i\varphi_{32}] - \frac{\exp[-i\varphi_{31}]}{2}\right)\right\}, \quad (19)$$

$$\nu_j = \sqrt{1 - \frac{4(\gamma-1)}{\gamma^2}\frac{\omega_L^2}{\omega_j^2}}, \quad \alpha_j = \sqrt{1 - \frac{\omega_L^2}{\omega_j^2}}, \quad (20)$$

$$\varphi_{1j} = -\arctan\left(((2-\gamma)/\gamma)\frac{\omega_L/\omega_j}{\alpha_j}\right),$$

$$\varphi_{2j} = -\arctan\left(\frac{\alpha_j}{\omega_L/\omega_j}\right), \quad (21)$$

$$\varphi_{3j} = -\arctan\left(\frac{\omega_L/\omega_j}{\alpha_j}\right), \quad j = 1, 2,$$

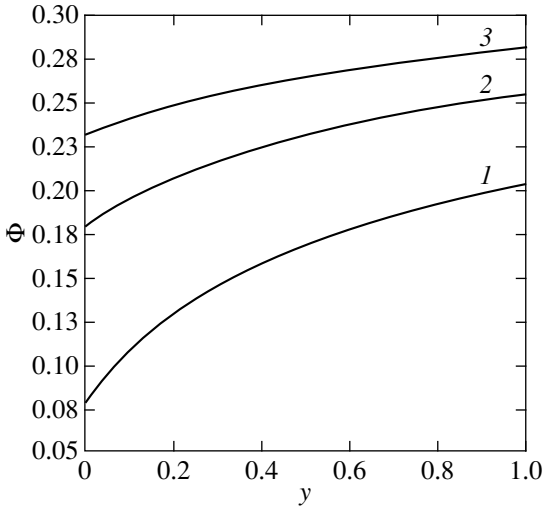

Fig. 1. Normalized quantity $\Phi = \left|\mathrm{Re}\left\{\frac{c_0 B_{12}}{A_1 A_2}\right\}\right|$ versus dimensionless difference frequency $y = \Omega/\omega_L$ at (*1*) $\omega_1 = 1.1\omega_L$, (*2*) $\omega_1 = 1.3\omega_L$, and (*3*) $\omega_1 = 1.5\omega_L$ for $\gamma = 1.4$.

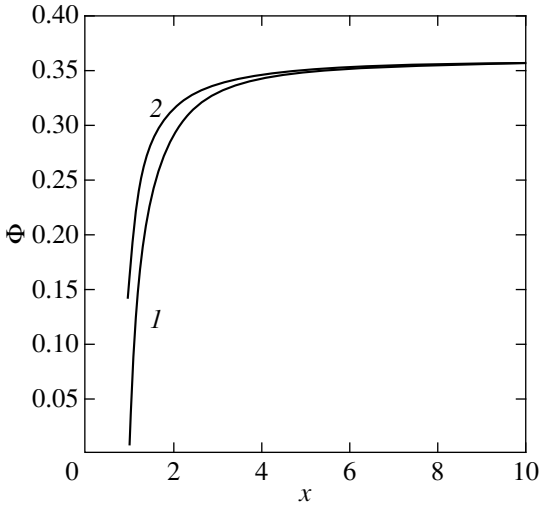

Fig. 2. Normalized quantity $\Phi = \left|\mathrm{Re}\left\{\frac{c_0 B_{12}}{A_1 A_2}\right\}\right|$ versus dimensionless generation frequency $x = \omega_1/\omega_L$ at (*1*) $\Omega = 0.01\omega_L$ and (*2*) $\Omega = \omega_L$ for $\gamma = 1.4$.

$$\Delta k_{21} = \frac{\omega_L}{c_0}\left[\sqrt{\frac{\omega_2^2}{\omega_L^2} - 1} - \sqrt{\frac{\omega_1^2}{\omega_L^2} - 1}\right]. \quad (22)$$

To solve Eq. (18), it is necessary to use the natural boundary condition

$$v^{(2)}\big|_{z=0} = 0, \quad (23)$$

which corresponds to the absence of difference-frequency waves at the $z = 0$ boundary surface, and to chooses only those solutions that at $\Omega > \omega_L$ would definitely correspond to running waves in the z-axis direction. Representing the solution to Eq. (18) as a sum of solutions for the corresponding homogeneous and inhomogeneous equations, we obtain, in view of Eq. (23),

$$v_R^{(2)} = \mathrm{Re}\{v^{(2)}\}, \quad (24)$$

$$v^{(2)} = B_{12}\left\{\exp\left[i(\Omega t - \Delta k_{21} z) + \frac{z}{H}\right]\right. \quad (25)$$
$$\left. - \exp\left[i\Omega t + \left(1 - \sqrt{1 - \frac{\Omega^2}{\omega_L^2}}\right)\frac{z}{2H}\right]\right\},$$

$$B_{12} = A_{12}/c_0^2\left[(\Delta k_{21})^2 + i\frac{\Delta k_{21}}{H} - \frac{\Omega^2}{c_0^2}\right]. \quad (26)$$

The first term in the right-hand part of Eq. (25), which is the solution of the inhomogeneous Eq. (18), corresponds to AGWs propagating in the z-axis direction at frequency $\Omega < \omega_L$, whose oscillation velocity amplitude increases with height in inverse proportion to the decreasing ambient density. At the same time, the corresponding quantity for linear AGWs at frequencies ω_1 and ω_2 Eq. (14) increases with height in inverse proportion to the square root of the decreasing ambient density. The second term in the right-hand part of Eq. (25), which is the solution of the corresponding homogeneous Eq. (18), corresponds to nonpropagating (inhomogeneous) AGWs at the same frequency $\Omega < \omega_L$, whose oscillation velocity amplitude increases with height considerably more slowly than that for propagating waves.

Thus, the solution (25) for $v^{(2)}$ describes the generation of two fundamentally different AGW groups at difference frequency $\Omega < \omega_L$. Since A_{12} Eq. (19) includes eight terms, the first and second groups consist of eight propagating and eight inhomogeneous AGWs. The wave amplitudes and phases are different in each group, while the phase velocities are the same. The latter implies that for parametric generation in an isothermal atmosphere, a fairly complex fringe pattern of the AGW field is produced at a difference frequency $\Omega < \omega_L$.

The numerically calculated Ω and ω_1 dependences (see Figs. 1, 2) of the normalized quantity $\Phi = |\mathrm{Re}\{B_{12}c_0/A_1A_2\}|$, which characterizes the oscillation velocity amplitude at the difference frequency for each of the two AGW groups at $t = 0$ and $z = 0$, lead us to the following conclusions:

First, as might be expected (Rudenko and Soluyan 1975), Φ reduces with decreasing difference frequency Ω. However, in contrast to a homogeneous medium [i.e., for $g = 0$ (Rudenko and Soluyan 1975)], the relative rate of this reduction decreases appreciably with increasing initial generation frequency ω_1 (see Fig. 1) in such a way that even at $\omega_1 \approx 4\omega_L$, Φ takes virtually the same

maximum values over the entire frequency range $0 \le \Omega \le \omega_L$ of interest (see Fig. 2).

Second, the fact that, in contrast to a homogeneous medium (Rudenko and Soluyan 1975), Φ is nonzero at $\Omega = 0$ (see Fig. 1) and $v^{(2)} \neq 0$ for $\Omega = 0$ and $z > 0$ [see Eq. (25)], implies that an acoustic wind emerges in the solar atmosphere whose direction coincides with that of the AGW propagation. The velocity of this acoustic flow increases with height in inverse proportion to the decreasing ambient density.

NONLINEAR GENERATION OF ACOUSTIC-GRAVITY WAVES AT THE SECOND HARMONIC

It is also of interest to study the nonlinear generation of propagating AGWs by disturbances from "forbidden" frequency range (Fleck and Schmitz 1993; Bodo *et al.* 1994), This situation is realized if the sum of frequencies exceeds the Lamb frequency: $\omega_1 + \omega_2 > \omega_L$, with $\omega_1 < \omega_L$ and $\omega_2 < \omega_L$. However, in order to simplify analytic calculations, we consider here the nonlinear generation of the second harmonic 2ω by assuming that the following relations hold in the boundary condition (3): $\omega_1 = \omega_2 = \omega < \omega_L$ and $A_1 = A_2 = A/2$.

We then find from Eqs. (9), (10), and (13) that

$$v_R^{(1)} = A\exp\left[\left(\frac{1}{2H} - \frac{\omega}{c_0}\beta\right)z\right]\cos\omega t, \quad (27)$$

$$p_R^{(1)} = \rho_{00}c_0A((2-\gamma)\omega_L/\gamma\omega + \beta) \times \exp\left[-\left(\frac{1}{2H} + \frac{\omega}{c_0}\beta\right)z\right]\sin\omega t, \quad (28)$$

$$\rho_R^{(1)} = \rho_{00}Ac_0^{-1}(\omega_L/\omega + \beta) \times \exp\left[-\left(\frac{1}{2H} + \frac{\omega}{c_0}\beta\right)z\right]\sin\omega t, \quad (29)$$

where

$$\beta = \sqrt{\frac{\omega_L^2}{\omega^2} - 1}. \quad (30)$$

Using Eqs. (27)–(29), we transform Eq. (17), by analogy with Eq. (18), to the form

$$\frac{\partial^2 v^{(2)}}{\partial t^2} - c_0^2\frac{\partial^2 v^{(2)}}{\partial z^2} + \frac{\gamma g\partial v^{(2)}}{\partial z} = A_{11}\exp\left[\left(\frac{1}{H} - 2\frac{\omega}{c_0}\beta\right)z\right]\sin(2\omega t), \quad (31)$$

where

$$A_{11} = \frac{A^2}{c_0}\omega^2\left\{\gamma\beta\left(\frac{\omega_L}{\omega} - \beta\right)((2-\gamma)\omega_L/\gamma\omega + \beta) + 2\frac{\omega_L}{\omega} - \beta\right\}. \quad (32)$$

The solution of Eq. (31) that satisfies the boundary condition (23) is a sum of the corresponding solutions to the homogeneous and inhomogeneous equations:

$$v_R^{(2)} = B_{11}\left\{V - \exp\left[\left(1 - \sqrt{1 - \frac{\omega^2}{\omega_L^2}}\right)\frac{z}{H}\right]\sin(2\omega t)\right\}, \quad (33)$$

where

$$B_{11} = A_{11}/4\omega\omega_L\left(\frac{\omega_L}{\omega} - \beta\right), \quad (34)$$

$$V = \begin{cases} \exp\left[\left(1 - \sqrt{1 - \dfrac{4\omega^2}{\omega_L^2}}\right)\dfrac{z}{2H}\right]\sin(2\omega t), & 2\omega < \omega_L \\ \exp\left(\dfrac{z}{2H}\right)\sin\left[2\omega t - \sqrt{\dfrac{4\omega^2}{\omega_L^2} - 1}\,\dfrac{z}{2H}\right], & 2\omega > \omega_L. \end{cases} \quad (35)$$

As we see from Eqs. (33)–(35), disturbances from the "forbidden" frequency range can generate propagating AGWs at the second harmonic for $\omega > \omega_L/2$, whose oscillation velocity amplitude will increase with height in inverse proportion to the decreasing ambient frequency, i.e., in the same way as for linear AGWs at the corresponding frequencies $\omega > \omega_L$. The oscillation velocity amplitude for nonpropagating waves at the second harmonic in the frequency range $\sqrt{3}\,\omega_L < 2\omega \le 2\omega_L$ increases with height faster than that for propagating AGWs.

Thus, only at certain frequencies $\sqrt{3}/2\ \omega_L < \omega \le \omega_L$ of boundary-surface ($z = 0$) oscillations will nonpropagating waves contribute to the AGW field at the second harmonic and at considerable heights $z > H$.

Definitive conclusions can be drawn from the plot of normalized quantity $\Psi = c_0|B_{11}|/A^2$ against initial generation frequency ω shown in Fig. 3. In the frequency range $\frac{\omega_L}{2} \le \omega \le \omega_L$, Ψ unambiguously characterizes the frequency ω dependence of the oscillation velocity amplitude for propagating AGWs at the second harmonic, which falls off with increasing ω. At the same time, the abrupt increase in Ψ at $\omega \longrightarrow 0$ (see Fig. 3), whose asymptotic behavior is described by the relation $\Psi \approx \frac{\omega_L}{\omega}$ following from Eq. (34), does not imply a similar monotonic increase in the amplitude of nonpropagating acoustic-gravity oscillations.

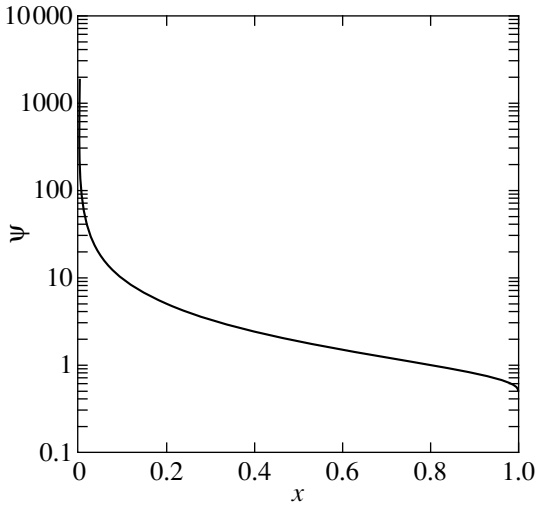

Fig. 3. Normalized quantity $\Psi = c_0|B_{11}|/A^2$ versus dimensionless generation frequency $x = \omega/\omega_L$ for $\gamma = 1.4$.

Indeed, from Eq. (33) with $\omega \longrightarrow 0$, we derive the following approximate expression

$$v_R^{(2)} \approx -\frac{A_1 A_2 z}{2c_0 H}\frac{\omega}{\omega_L}\sin(2\omega t), \qquad (36)$$

from which it follows that the amplitude of acoustic-gravity oscillations tends to zero as $\omega \longrightarrow 0$.

CONCLUSION

Let us formulate our main results and the conclusions that follow from them.

We have investigated the parametric generation of AGWs by using a simple model of a plane isothermal solar atmosphere in the approximation of a fixed field for vertically propagating AGWs with frequencies above the Lamb frequency.

We showed that, in the frequency range of interest, which lies below the Lamb frequency and is therefore "forbidden" for the propagation of AGWs during their linear generation, both nonpropagating (inhomogeneous) and propagating AGWs are generated at the difference frequency through the nonlinear interaction of primary waves.

We established that, at the difference frequency, the oscillation velocity amplitude for propagating AGWs increases with height in inverse proportion to the decreasing ambient density, i.e., appreciably faster than for primary waves, for which the corresponding quantity is known to increase in inverse proportion to the square root of the ambient density.

We found that, at zero difference frequency, an acoustic wave is produced in an isothermal atmosphere, whose direction coincides with the direction of AGW propagation, with its velocity increasing with height in inverse proportion to the decreasing ambient density.

We also analyzed the nonlinear generation of AGWs at the second harmonic during the interaction of disturbances from the "forbidden" frequency range. At certain generation frequencies, nonpropagating acoustic-gravity oscillations were found to mainly contribute to the AGW field at the second harmonic outside the forbidden frequency range at considerable heights.

Thus, our results clearly suggest that nonlinear effects during the nonlinear propagation of impulse AGWs in the solar atmosphere give rise to propagating AGW impulses in the frequency range forbidden for linear AGW propagation and to an acoustic wind. The latter assertion is consistent with calculations of nonlinear AGW propagation in the solar atmosphere for their impulse and tone–impulse generation modes (Rammacher and Ulmschneider 1992; Fleck and Schmitz 1993; Bodo *et al.* 1994; Sutmann and Ulmschneider 1995b). However, the conclusion of Fleck and Schmitz (1993) that the energy transfer by AGWs in the forbidden (for them) frequency range is attributable only to the evolution of the shocks produced in the corresponding perturbations does not follow from this assertion. Indeed, as we showed above [see Eq. (25)], the formation of running AGWs in the forbidden frequency range begins from the very outset of the primary-wave propagation at the corresponding frequencies and is attributable to a manifestation of the parametric wave generation at the difference frequency. This process becomes pronounced at considerable heights, which significantly exceed the scale height of an isothermal atmosphere, where shocks are, naturally, produced (Kosovichev and Popov 1979; Rammacher and Ulmschneider 1992; Fleck and Schmitz 1993; Bodo *et al.* 1994; Sutmann and Ulmschneider 1995b; Cheng 1996). Clearly, the evolution of shock waves in the corresponding disturbances will only emphasize the low-frequency generation, because, during the propagation of shock-wave disturbances, the energy is known (Petukhov and Fridman 1980) to be redistributed in their spectra into the relatively low-frequency range due to an increase in the characteristic wave duration.

REFERENCES

1. G. Bodo, W. Kalkofen, S. Massaglia, and P. Rossi, Astron. Astrophys. **284**, 976 (1994).
2. Q. Y. Cheng, Astron. Astrophys. **313**, 971 (1996).
3. P. Colella and P. R. Woodward, J. Comput. Phys. **54**, 174 (1984).
4. F. V. Coroniti, R. K. Ulrich, and Z. Wang, Astrophys. J. **444**, 879 (1995).
5. É. E. Dubov, Itogi Nauki Tekh., Ser. Astron. **14**, 148 (1978).
6. C. Eckart, *Hydrodynamics of Oceans and Atmospheres* (Pergamon, New York, 1960; Inostrannaya Literatura, Moscow, 1963).
7. F. Finaudi, J. Geophys. Res. **75**, 193 (1970).
8. B. Fleck and F. Schmitz, Astron. Astrophys. **273**, 671 (1993).

9. B. Fleck and F. Schmitz, Astron. Astrophys. **337**, 487 (1998).
10. S. V. Garmash, E. M. Lin'kov, L. N. Petrova, and G. M. Shved, Izv. Akad. Nauk SSSR, Ser. Fiz. Atmos. Okeana **25**, 1290 (1989).
11. I. A. Klimishin, *Shock Waves in Stellar Envelopes* (Nauka, Moscow, 1984).
12. A. G. Kosovichev and Yu. P. Popov, Zh. Vychisl. Mat. Mat. Fiz. **19**, 1253 (1979).
13. H. Lamb, *Hydrodynamics* (Cambridge University Press, Cambridge, 1932; Gostekhizdat, Moscow, 1947).
14. Z. E. Musielak, G. Sutmann, and P. Ulmschneider, Astron. Astrophys. **340**, 556 (1998).
15. Yu. V. Petukhov and E. V. Fridman, Akust. Zh. **26**, 263 (1980) [Sov. Phys. Acoust. **26**, 83 (1980)].
16. W. Rammacher and P. Ulmschneider, Astron. Astrophys. **253**, 586 (1992).
17. N. N. Romanova, Izv. Akad. Nauk SSSR, Fiz. Atmos. Okeana **6**, 134 (1970).
18. N. N. Romanova, Izv. Akad. Nauk SSSR, Fiz. Atmos. Okeana **7**, 1251 (1971).
19. O. V. Rudenko and S. I. Soluyan, *Theoretical Foundations of Nonlinear Acoustics* (Nauka, Moscow, 1975; Consultants Bureau, New York, 1977).
20. A. B. Severnyĭ, *Problems in Solar Physics* (Nauka, Moscow, 1988).
21. G. Sutmann and P. Ulmschneider, Astron. Astrophys. **294**, 232 (1995a).
22. G. Sutmann and P. Ulmschneider, Astron. Astrophys. **294**, 241 (1995b).
23. A. M. Uralov, Izv. Akad. Nauk SSSR, Fiz. Atmos. Okeana **18**, 797 (1982).
24. S. V. Vorontsov and V. N. Zharkov, Itogi Nauki Tekh., Ser. Astron. **38**, 253 (1988).

Translated by A. Dambis

Astronomy Letters, Vol. 27, No. 3, 2001, pp. 193–197. Translated from Pis'ma v Astronomicheskiĭ Zhurnal, Vol. 27, No. 3, 2001, pp. 227–231.

Photometric Observations of Mutual Events in Saturn's System of Regular Satellites in 1995

A. V. Devyatkin* and A. S. Miroshnichenko

Pulkovo Astronomical Observatory, Russian Academy of Sciences, Pulkovskoe shosse 65, St. Petersburg, 196140 Russia

Received September 8, 1999; in final form, July 4, 2000

Abstract—We carried out observations of mutual events in Saturn's system of satellites as part of the PHESAT95 International Program. Three light curves of these events were obtained. We developed a technique of allowance for the influence of the law of light reflection from the surfaces of Saturn's satellites, photometric nonuniformity of their surfaces, the phase effect, and the illumination distribution in the satellite penumbra (given the brightness distribution over the solar disk) on the light curve of an occultation or eclipse of one satellite by another. This technique is used to interpret our observations of these events and to determine the minimum separations between satellites or between a satellite and the shadow center of another satellite and the corresponding timings. *© 2001 MAIK "Nauka/Interperiodica".*

Key words: *Solar system—satellites, planets, occullations, eclipses*

INTRODUCTION

Over the period of Saturn's revolution around the Sun, the Earth crosses the planet's equatorial plane twice. Since Saturn's regular satellites revolve in planes close to its equator, mutual events can be observed: occultations of one satellite by another (O) and eclipses of one satellite by another (E). During observations of these events, the fluxes from the satellites are measured and the time is recorded. The reduction of photometric observations of mutual events involves determining the minimum separation between the satellite centers for occultations or the separations between the center of the eclipsed satellite and the shadow center of the eclipsing satellite, as well as the corresponding time of minimum of the brightness decline. The positional accuracy of determining the relative positions of satellites can reach $0\farcs01$ (Devyatkin and Bobylev 1995). Observations of mutual events are valuable for developing the theory of satellite motion and for studying the dynamical effects in Saturn's system of satellites.

OBSERVATIONS OF MUTUAL EVENTS

We performed our photometric observations of eclipses of satellites in Saturn's system in August 1995 with the 1-m telescope at the Tien Shan Observatory of the Fesenkov Astrophysical Institute (Ministry of Science, Academy of Sciences of Kazakhstan), located near the Great Almaty Lake (altitude 2800 m), using the FP3U photometer-polarimeter of the Pulkovo Astronomical Observatory (Bergner *et al.* 1988) equipped with a photomultiplier with a GaAs photocathode and a detector thermoelectrically cooled to –20°C. The observations were carried out with a $26''$ aperture, with the background at an angular distance of $84''$ subtracted. The brightness of satellites was measured with 15-s exposure times. After each four or five measurements, we visually checked the positions of the objects within the photometer aperture. The measurements were recorded in digital form with an IBM PC AT-286 computer in real time. The accuracy of individual measurements was about 1%.

REDUCTION OF PHOTOMETRIC OBSERVATIONS OF MUTUAL EVENTS

We first reduced our observations by taking into account the following peculiarities of our data: Since all light curves of the events exhibited a temporal trend, we removed the linear trend at all data points, except those at which an event occurred, by least squares and then used the same points to determine the mean flux from the satellites before and after the event. Subsequently, we subtracted the mean flux from all fluxes. Figures 1–3 show the observed total flux from the satellites before, during, and after the events. The flux variations seen in the figures are attributable both to mutual events and to variations in atmospheric transparency. The latter strongly affected the records of the first and third events (Figs. 1, 3). The accuracy of these observations was low, and the signal was at or below the fluctuation level. Nevertheless, we also interpreted these results, although their significance turned out to

* E-mail address for contacts: adev@gao.spb.ru

1063-7737/01/2703-0193$21.00 © 2001 MAIK "Nauka/Interperiodica"

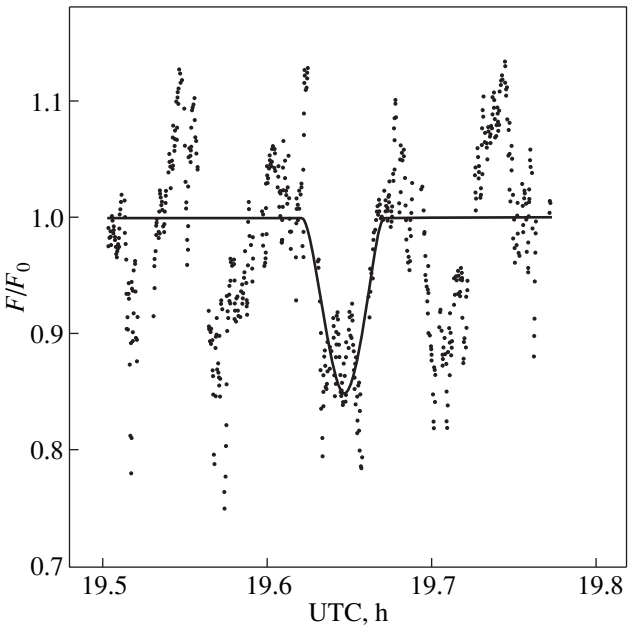

Fig. 1. The light curve of event 2E3 (August 10, 1995; Enceladus eclipses Tethys). The observations are indicated by dots, and the solid line represents the theoretical curve of variations in the total flux from the two satellites.

be very low. The most accurate and reliable results were obtained for event 4O6 (Dione occults Titan).

THE TECHNIQUE OF ALLOWANCE FOR THE PHOTOMETRIC PECULIARITIES OF EVENTS

The satellites for which the data are given in Table 1 belong to the regular group. All of these satellites, except Hyperion, exhibit axial rotation synchronized with their revolution period. Thus, the same side of the satellites always faces Saturn. The photometric data show that some of Saturn's satellites exhibit brightness variations with satellite orbital position (i.e., with orbital phase angle), which is attributable to photometric nonuniformity of the reflecting surface and to synchronous rotation. When the light curves of such events are interpreted, these factors, as well as the law of light reflection from the satellite surface, the phase effect and the illumination distribution in the penumbra must be taken into account. The influence of photometric nonuniformity on positional observations of Jupiter's and Saturn's satellites was considered by Devyatkin and Bobylev (1988, 1991), Devyatkin (1991), and Devyatkin *et al.* (1998). The effects were shown to be significant. Our technique is based on the development of the ideas in the above papers. In our case, we numerically constructed images for each eclipsed or occulted satellite. The following factors were taken into account in the satellite model image:

(1) The law of light reflection from the satellite surface;

(2) Photometric nonuniformity of the reflecting surface;

(3) The phase effect;

(4) The illumination distribution in the penumbra;

(5) The brightness distribution over the solar disk.

The first three factors were taken into account as prescribed in the above papers. The brightness distribution over the disks of Saturn's satellites was computed by using ground-based observations and data from the Voyager spacecraft. The intensity (brightness) distribution over the satellite disk I, relative to the satellite total flux F, was calculated using the formula (Buratti and Veverka 1984; Bonnie and Buratti 1984)

$$\frac{I}{F} = A\frac{\mu_0}{\mu + \mu_0} f(\alpha) + (1 - A)\mu_0,$$

where $f(\alpha) = A + B\alpha + C\alpha^2$ is the phase function of the surface; α is the phase angle; and μ_0 and μ are the cosines of the angles of incidence and reflection, respectively. The parameters used to construct the model, with allowance for photometric nonuniformity of the reflecting surface, are listed in Table 2.

The phase effect, the illumination distribution in the satellite penumbra, and the brightness distribution over the solar disk were taken into account as prescribed by

Table 1. Saturn's system of regular satellites (Arlot and Thuillot 1993) (P is the revolution period, R is the radius, i is the orbital inclination, and V is the visual magnitude at average opposition)

Satellite	P, day	R, km	i	V
Mimas	0.942	196	1°.563	$12^m.9$
Enceladus	1.370	250	0.026	11.7
Tethys	1.888	530	1.098	10.2
Dione	2.737	560	0.014	10.4
Rhea	4.518	765	0.347	9.7
Titan	15.945	2575	0.296	8.3
Hyperion	21.277	150	0.644	14.2
Iapetus	79.331	730	14.72	11.1

Table 2. Photometric data for Saturn's satellites (Buratti and Veverka 1984) (k is the ratio of the surface albedo of one hemisphere to the surface albedo of the other hemisphere, and θ is the orbital phase angle at which the hemisphere with a larger albedo faces the observer)

Satellite	A	B	C	$f(0)$	k	θ, deg
Mimas	0.7	−0.86	0.19	1.1	1.0	–
Enceladus	0.4	−0.51	−0.17	2.4	1.2	270
Tethys	0.7	−0.95	0.20	1.45	1.1	90
Dione	1.0	−1.24	0.50	1.0	1.8	90
Rhea	0.95	1.33	0.54	1.1	1.2	90
Titan	–	–	–	–	1.0	–
Hyperion	–	–	–	–	1.0	–
Iapetus	–	–	–	–	6.9	90

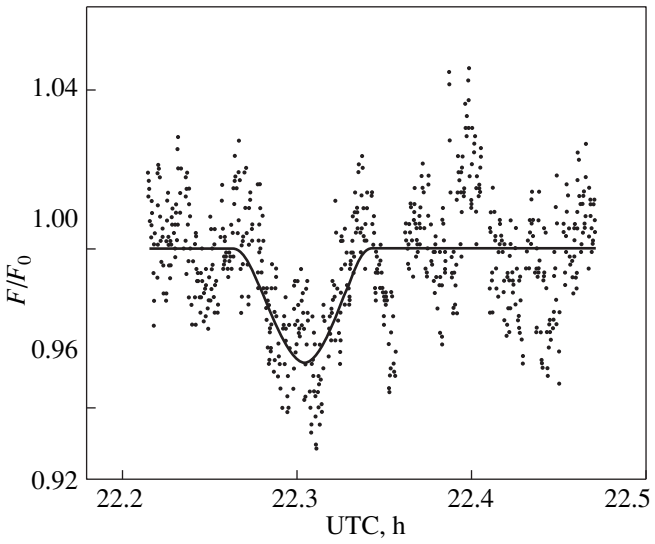

Fig. 2. The light curve of event 4O6 (August 13, 1995; Dione occults Titan). The notation is the same as in Fig. 1.

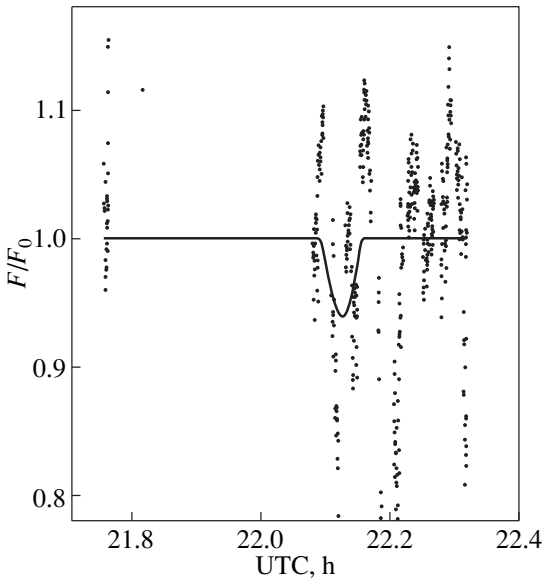

Fig. 3. The light curve of event 2E3 (August 25, 1995; Enceladus eclipses Tethys). The notation is the same as in Fig. 1.

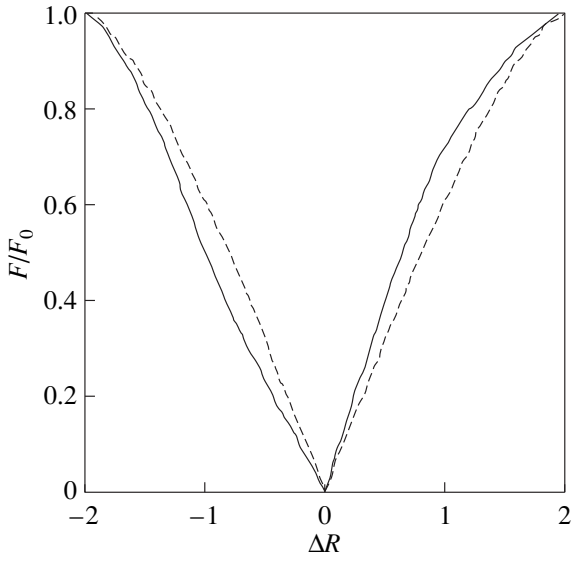

Fig. 4. The effect of photometric nonuniformity of Dione's reflecting surface on the occultation light curve without (dashed line) and with (solid line) allowance for photometric nonuniformity.

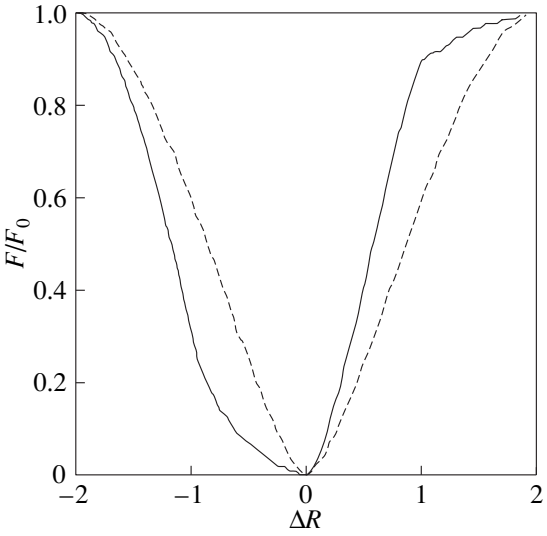

Fig. 5. Same as Fig. 4 for Iapetus.

Devyatkin *et al.* (1998). Having computed the brightness distribution over the disk of the occulted or eclipsed satellite, with allowance for all photometric factors, and the illumination distribution in the "umbra + penumbra" region (for eclipses), we simulated the occultation or eclipse (the passage of the disk of one satellite across the disk of another satellite or the passage of the shadow across the satellite disk) and determined the ratio of the flux from the occulted or eclipsed satellite to the total flux from the satellite. These computations were performed in the same way as those for Jupiter's Galilean satellites (Devyatkin *et al.* 1998).

Figures 4 and 5 present the model curves for the central occultations of Dione and Iapetus by model satellites with the same radius as that of the occulted satellite. In our model, which takes into account photometric nonuniformity of the reflecting surface, we assumed the albedo of one hemisphere of the satellite to be a factor of k larger than that of the other hemisphere (see Table 2). Figures 4 and 5 show an occultation when both the brighter and darker hemispheres of the satellite (with equal areas) are observed. Clearly, when interpreting the observations, an error up to 0.2 and 0.4 in the separation between the satellite centers of the radius

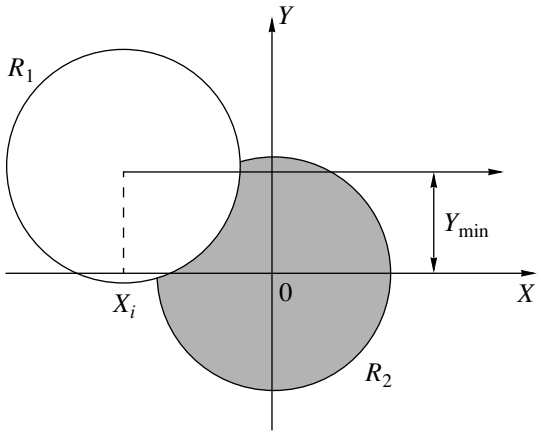

Fig. 6. Geometric elements of the model event in Saturn's system of satellites.

for occultations of Dione and Iapetus, respectively, is possible.

INTERPRETING THE PHOTOMETRIC OBSERVATIONS

Using the technique developed by Devyatkin *et al.* (1998), we computed model occultation and eclipse light curves for various minimum separations between the components of the events [satellite minus satellite, satellite minus (umbra + penumbra)] (see Fig. 6, where R_1 is the occulting satellite or the satellite shadow and R_2 is the occulted or eclipsed satellite). From these light curves, we deduced the flux ratio $E_i(Y_j^{\min})/E_0$, where X_i is the separation between the satellite centers (or the separation between the satellite and shadow centers), E_0 is the total flux from the satellites before or after the event, and E_i is the total flux from the satellites during the event at the separation X_i between the components of the event. Subsequently, we fitted the model curves to the observed curve and determined the sums of the squares of the deviations of the observed values from the model values; as a result, we chose the model curve with a minimum of the sum. The position of the minimum of the model curve (relative to the observed curve) was used to determine the time of the observed brightness minimum for the occulted or eclipsed satellite. The minimum separation corresponding to the minimum of the light curve was a parameter for computing the model curve.

Figures 1–3 show the observed light curves for Saturn's satellites and the computed model curves for these events. The model curves were chosen by using the criterion of a minimum of the squares of the residuals. In all cases, the satellites were observed as a whole, and we did not determine their individual brightnesses. To determine the brightness decline in the occulted satellites relative to the brightness of the unocculted satellite, we used the ephemeris values of the satellite magnitudes.

Table 3 gives the results of our observations, their comparison with the ephemeris values, and other relevant data. As we see from the Table 3, the results for event 2E3 (Enceladus eclipses Tethys) have a low accuracy and are most likely a demonstration of the difficulties of such observations with photometers. It is preferable to observe such events with panoramic detectors, for example, with CCD arrays. In that case, both the background and the satellite brightness can be recorded, and transparency variations can be checked using other objects within the frame.

Table 3. Comparison of the ephemeris (Arlot and Thuillot 1993; Emel'yanov 1996) with our observations ($t_{\min}$ is the time of minimum brightness, Δm is the maximum total decline in brightness of the two satellites, and ΔR is the minimum separation between the satellite centers for occultations or between the satellite and shadow centers for eclipses)

Date of event	Type of event	Source of data	$t_{\min}$, UTC	Δm	ΔR, km
Aug. 10, 1995	2E3	Arlot and Thuillot (1993)	$19^h39^m13^s$	0.050^m	
	Enceladus eclipses Tethys	Emel'yanov (1996)	19 39 22	0.112	
		Observations	19 38 48	0.178	366
			±16	±0.037	±53
Aug. 13, 1995	4O6	Arlot and Thuillot (1993)	$22^h17^m38^s$	0.042^m	
	Dione occults Titan	Emel'yanov (1996)	22 18 20	0.046	
		Observations	22 18 12	0.031	2060
			±2	±0.002	±21
Aug. 25, 1995	2E3	Arlot and Thuillot (1993)	$22^h09^m36^s$	0.029^m	
	Enceladus eclipses Tethys	Emel'yanov (1996)	22 09 46	0.030	
		Observations	22 07 37	0.070	562
			±73	±0.052	±74

CONCLUSION

We have carried out photometric observations of mutual events in Saturn's system of regular satellites with the 1-m telescope at the Tien Shan Observatory of the Fesenkov Astrophysical Institute (Ministry of Science, Academy of Sciences of Kazakhstan). Two eclipse light curves and one occultation curve were obtained. We interpreted the observations by using a specially developed technique of allowance for the influence of the law of light reflection from the surfaces of Saturn's satellites, photometric nonuniformity of their surfaces, and the phase effect on the light curves of occultations or eclipses of one satellite by another. We determined the minimum separations between the satellites or between one satellite and the shadow center of another satellite, and the timings of the events. The interpretation of the occultation of Titan by Dione on August 13, 1995, proved to be most reliable.

REFERENCES

1. J. E. Arlot and W. Thuillot, Icarus **105**, 427 (1993).
2. Yu. K. Bergner, S. L. Bondarenko, and A. S. Miroshnichenko, Izv. Gl. Astron. Obs. Akad. Nauk SSSR **205**, 142 (1988).
3. J. Bonnie and B. Buratti, Icarus **59**, 392 (1984).
4. B. Buratti and J. Veverka, Icarus **58**, 254 (1984).
5. A. V. Devyatkin, Author's Abstract of Candidate's Dissertation (Gl. Astron. Obs. Akad. Nauk SSSR, Leningrad, 1991).
6. A. V. Devyatkin and V. V. Bobylev, Astron. Tsirk., No. 1533, 23 (1988).
7. A. V. Devyatkin and V. V. Bobylev, Izv. Gl. Astron. Obs. Akad. Nauk SSSR **207**, 67 (1991).
8. A. V. Devyatkin and V. V. Bobylev, Izv. Gl. Astron. Obs. Akad. Nauk SSSR **209**, 88 (1995).
9. A. V. Devyatkin, A. N. Gritsuk, and A. G. Svidunovich, Izv. Gl. Astron. Obs. Akad. Nauk **213**, 108 (1998).
10. N. V. Emel'yanov, Pis'ma Astron. Zh. **22**, 153 (1996) [Astron. Lett. **22**, 135 (1996)].

Translated by N. Samus'

Astronomy Letters, Vol. 27, No. 3, 2001, pp. 198–205. Translated from Pis'ma v Astronomicheskiĭ Zhurnal, Vol. 27, No. 3, 2001, pp. 232–240.

Stability of Periodic Solutions for Hill's Averaged Problem with Allowance for Planetary Oblateness

M. A. Vashkov'yak* and N. M. Teslenko

Keldysh Institute of Applied Mathematics, Russian Academy of Sciences, Miusskaya pl. 4, Moscow, 125047 Russia

Received April 12, 2000

Abstract—We analyze the stability of periodic solutions for Hill's double-averaged problem by taking into account a central planet's oblateness. They are generated by steady-state solutions that are stable in the linear approximation. By numerically calculating the monodromy matrix of variational equations, we plot its trace against the integral of the problem—an averaged perturbing function, for two model systems, [(Sun + Moon)–Earth–satellite] and (Sun–Uranus–satellite). We roughly estimate the ranges of values for the parameters of satellite orbits corresponding to periodic solutions of the evolutionary system that are stable in the linear approximation. © *2001 MAIK "Nauka/Interperiodica".*

Key words: *Hill's averaged problem, stability, satellite orbits*

1. INTRODUCTION: STATEMENT OF THE PROBLEM

Here, we investigate the stability of periodic solutions for Hill's averaged problem with allowance for the oblateness of a central planet. The families of these periodic solutions are generated by steady-state solutions, which are stable in the linear approximation.

The evolutionary system of differential equations for elements was derived by independently averaging the perturbing function of the problem over the mean longitudes of perturbing bodies and a satellite of an oblate planet. For completeness, we provide it here in the standard notation of Keplerian elements for a satellite orbit: semimajor axis a, eccentricity e, inclination i, argument of the pericenter latitude ω, and longitude of the ascending node Ω. The angular variables are associated with the orbital plane of a coplanar system of N distant perturbing points (inclined at angle ε to the planet's equatorial plane) and with the line of intersection of these planes.

The evolutionary system

$$\frac{de}{d\tau} = 10e(1-e^2)^{1/2}\sin^2 i\sin 2\omega,$$

$$\frac{di}{d\tau} = -10e^2(1-e^2)^{-1/2}\sin i\cos i\sin 2\omega$$

$$-8\gamma\sin\varepsilon(1-e^2)^{-2}\sin\Omega(\cos\varepsilon\cos i-\sin\varepsilon\sin i\cos\Omega),$$

$$\frac{d\omega}{d\tau} = 4\gamma(1-e^2)^{-2}(5\cos^2 i-1)+2(1-e^2)^{-1/2}$$

$$\times[5\cos^2 i-1+e^2+5(\sin^2 i-e^2)\cos 2\omega]$$

$$+4\gamma\sin\varepsilon(1-e^2)^{-2}$$

$$\times\left\{2\cos\varepsilon(5\cos^2 i-4)\cos i\cos\Omega/\sin i\right. \quad (1)$$

$$\left.+\frac{1}{2}\sin\varepsilon[3(1-5\cos^2 i)+(3-5\cos^2 i)\cos 2\Omega]\right\},$$

$$\frac{d\Omega}{d\tau} = \cos i[-8\gamma(1-e^2)^{-2}$$

$$+2(1-e^2)^{-1/2}(5e^2\cos 2\omega-3e^2-2)]$$

$$-8\gamma\sin\varepsilon(1-e^2)^{-2}\left[\cos\varepsilon\cos 2i\cos\Omega/\sin i\right.$$

$$\left.-\frac{1}{2}\sin\varepsilon\cos i(3+\cos 2\Omega)\right]$$

has the first integral—an averaged perturbing function, which does not explicitly depend on τ:

$$W(e,i,\omega,\Omega) = 2(e^2-\sin^2 i)+e^2\sin^2 i(5\cos 2\omega-3)$$

$$+2\gamma(1-e^2)^{-3/2}[1/3+\cos 2i-\sin 2\varepsilon\sin 2i\cos\Omega$$

$$-2\sin^2\varepsilon(\sin^2 i\sin^2\Omega+\cos 2i)].$$

* E-mail address for contacts: vashkov@spp.keldysh.ru

1063-7737/01/2703-0198$21.00 © 2001 MAIK "Nauka/Interperiodica"

In Eqs. (1), γ is a constant parameter, and τ is a normalized independent variable that monotonically varies with physical time t. They are given by

$$\gamma = -\frac{\mu a_0^2 c_{20}}{a^5 \sum_{j=1}^{N} \mu_j a_j^{-3}}, \quad \tau = \beta \mu^{1/2} a^{-3/2} t, \quad \beta = -\frac{3 c_{20} a_0^2}{16 \gamma a^2},$$

where μ and a are, respectively, the product of the gravitational constant by the central planet's mass and the semimajor axis of the satellite orbit, which is constant in the averaged problem under consideration; the same parameters with subscript j refer to the jth perturbing point; a_0 is the planet's mean equatorial radius, and c_{20} is the coefficient of the second zonal harmonic of its gravitational field.

System (1) has steady-state solutions (Lidov and Yarskaya 1974; Kudielka 1994), for which

$$(\cos i = \cos\Omega = 0 \text{ or } \sin\Omega = 0) \text{ and } \sin 2\omega = 0.$$

Previously (Vashkov'yak 1999b; Vashkov'yak and Teslenko 2000), we constructed the families of symmetric and asymmetric periodic solutions generated by the above equilibrium states for the specific parameters ε, γ, and N. Here, our goal is to analyze the stability of the periodic solutions we found.

The T-periodic solution of the evolutionary system (1), specified by functions $\tilde{e}(\tau)$, $\tilde{i}(\tau)$, $\tilde{\omega}(\tau)$, and $\tilde{\Omega}(\tau)$ such that

$$\begin{aligned} \tilde{e}(\tau + T) &= \tilde{e}(\tau), \quad \tilde{i}(\tau + T) = \tilde{i}(\tau), \\ \tilde{\omega}(\tau + T) &= \tilde{\omega}(\tau), \quad \tilde{\Omega}(\tau + T) = \tilde{\Omega}(\tau) \end{aligned} \tag{2}$$

is assumed to be known. Linearizing system (1), with respect to the small deviations from the periodic solution (2)

$$\begin{aligned} z_1 &= e - \tilde{e}(\tau), \quad z_2 = i - \tilde{i}(\tau), \\ z_3 &= \omega - \tilde{\omega}(\tau), \quad z_4 = \Omega - \tilde{\Omega}(\tau), \end{aligned}$$

yields a system of linear differential equations with T-periodic coefficients relative to τ:

$$\frac{d\mathbf{z}}{d\tau} = \mathbf{A}(\tau)\mathbf{z}, \tag{3}$$

where $\mathbf{z} = \mathbf{col}(z_1, z_2, z_3, z_4)$, $\mathbf{A}(\tau + T) = \mathbf{A}(\tau) = \|a_{jk}(\tilde{e}(\tau), \tilde{i}(\tau), \tilde{\omega}(\tau), \tilde{\Omega}(\tau))\|$, $j, k = 1, 2, 3, 4$.

Below, we give formulas for the elements of matrix $\mathbf{A}$, in which a tilde was omitted to save space:

$$a_{11} = 10(1-2e^2)(1-e^2)^{-1/2}\sin^2 i \sin 2\omega,$$

$$a_{12} = 10e(1-e^2)^{1/2}\sin 2i \sin 2\omega,$$

$$a_{13} = 20e(1-e^2)^{1/2}\sin^2 i \cos 2\omega, \quad a_{14} = 0,$$

$$a_{21} = -5e(2-e^2)(1-e^2)^{-3/2}\sin 2i \sin 2\omega$$
$$- 32\gamma e \sin\varepsilon(1-e^2)^{-3}\sin\Omega(\cos\varepsilon\cos i - \sin\varepsilon\sin i\cos\Omega),$$

$$a_{22} = -10e^2(1-e^2)^{-1/2}\cos 2i \sin 2\omega$$
$$+ 8\gamma\sin\varepsilon(1-e^2)^{-2}\sin\Omega(\cos\varepsilon\sin i + \sin\varepsilon\cos i\cos\Omega).$$

$$a_{23} = -10e^2(1-e^2)^{-1/2}\sin 2i \cos 2\omega,$$

$$a_{24} = -8\gamma\sin\varepsilon(1-e^2)^{-2}(\cos\varepsilon\cos i\cos\Omega - \sin\varepsilon\sin i\cos 2\Omega),$$

$$a_{31} = 16\gamma e(1-e^2)^{-3}\left\{5\cos^2 i - 1 + \sin 2\varepsilon(5\cos^2 i - 4)\cos i\cos\Omega/\sin i + \frac{1}{2}\sin^2\varepsilon[3(1-5\cos^2 i) + (3-5\cos^2 i)\cos 2\Omega]\right\}$$
$$+ 2e(1-e^2)^{-3/2}[1 - e^2 + 5\cos^2 i - 5(1 - e^2 + \cos^2 i)\cos 2\omega],$$

$$a_{32} = 20\gamma(1-e^2)^{-2}\sin 2i\left[\frac{1}{2}\sin^2\varepsilon(3 + \cos 2\Omega) - 1\right]$$
$$- 20(1-e^2)^{-1/2}\sin 2i\sin^2\omega + 4\gamma(1-e^2)^{-2} \times \sin 2\varepsilon\cos\Omega(4 - 15\cos^2 i + 10\cos^4 i)/\sin^2 i, \tag{4}$$

$$a_{33} = 20(1-e^2)^{-1/2}(e^2 - \sin^2 i)\sin 2\omega,$$

$$a_{34} = -8\gamma(1-e^2)^{-2}\sin\Omega \times \left[\frac{1}{2}\sin 2\varepsilon(5\cos^2 i - 4)\cos i/\sin i + \sin^2\varepsilon(3 - 5\cos^2 i)\cos\Omega\right],$$

$$a_{41} = -16\gamma e(1-e^2)^{-3}[2\cos i + \sin 2\varepsilon\cos 2i\cos\Omega/\sin i - \sin^2\varepsilon\cos i(3 + \cos 2\Omega)]$$
$$+ 2e(1-e^2)^{-3/2}\cos i[(5\cos 2\omega - 3)(2 - e^2) - 2],$$

$$a_{42} = 4\gamma(1-e^2)^{-2}\{\sin i[2 - \sin^2\varepsilon(3 + \cos 2\Omega)] + \sin 2\varepsilon\cos i(3 - 2\cos^2 i)\cos\Omega/\sin^2 i\}$$
$$+ 2(1-e^2)^{-1/2}\sin i(2 + 3e^2 - 5e^2\cos 2\omega),$$

$$a_{43} = -20e^2(1-e^2)^{-1/2}\cos i \sin 2\omega,$$

$$a_{44} = -8\gamma\sin\varepsilon(1-e^2)^{-2}(\sin\varepsilon\cos i\sin 2\Omega - \cos\varepsilon\cos 2i\sin\Omega/\sin i).$$

The stability of the zero solution for the system of Eqs. (3) written in matrix form,

$$\frac{d\mathbf{Z}}{d\tau} = \mathbf{A}(\tau)\mathbf{Z}, \quad (5)$$

is known from the Lyapunov-Floquet theory to be determined by eigenvalues ρ of the fundamental matrix at time $\tau = T$, which satisfies system (5) at $\mathbf{Z}(0) = \mathbf{E}$ ($\mathbf{E}$ is a unit matrix of the fourth order), i.e., the monodromy matrix

$$\mathbf{M} = \mathbf{Z}(T). \quad (6)$$

The characteristic equation for ρ is

$$\det\|\mathbf{M} - \rho\mathbf{E}\| = 0. \quad (7)$$

Note that the evolutionary system (1) and the variational Eqs. (3) and (5) can be reduced to canonical form by passing from Keplerian elements to, for example, Delone-type elements

$$G = (1-e^2)^{1/2}, \quad g = \omega, \quad H = G\cos i, \quad h = \Omega.$$

The function W in the new variables is the Hamiltonian, which does not explicitly depend on time either. It can be shown that in the new (canonical) variables

$$\mathbf{y} = \mathbf{col}(G-\tilde{G}, H-\tilde{H}, g-\tilde{g}, h-\tilde{h})$$

the variational equations

$$\frac{d\mathbf{y}}{d\tau} = \mathbf{C}(\tau)\mathbf{y}$$

can be derived by using the nondegenerate linear T-periodic transformation

$$\mathbf{y} = \mathbf{B}(\tau)\mathbf{z}, \quad \mathbf{B}(\tau+T) = \mathbf{B}(\tau) = \|b_{jk}(\tau)\|,$$

where $\det\mathbf{B} = \tilde{e}\sin\tilde{i} \neq 0$, $b_{11} = \dfrac{\partial G}{\partial\tilde{e}} = -\tilde{e}(1-\tilde{e}^2)^{-1/2}$, $b_{12} = b_{13} = b_{14} = 0$, $b_{21} = \dfrac{\partial H}{\partial\tilde{e}} = b_{11}\cos\tilde{i}$, $b_{22} = \dfrac{\partial H}{\partial\tilde{i}} = -(1-\tilde{e}^2)^{1/2}\sin\tilde{i}$, $b_{23} = b_{24} = 0$, $b_{31} = b_{32} = b_{34} = 0$, $b_{33} = 1$, $b_{41} = b_{42} = b_{43} = 0$, and $b_{44} = 1$.

Matrix $\mathbf{C}$ is given by

$$\mathbf{C}(\tau) = \left[\mathbf{B}(\tau)\mathbf{A}(\tau) + \frac{d\mathbf{B}(\tau)}{d\tau}\right]\mathbf{B}^{-1}(\tau),$$

$$\mathbf{C}(\tau+T) = \mathbf{C}(\tau)$$

[it is well known that matrix $\mathbf{B}(\tau)$ can be theoretically chosen in such a way that matrix $\mathbf{C}$ is constant; this is the Lyapunov theorem on reducibility].

It is important to note that the characteristic Eq. (7) is invariant for the above transformation [see, e.g., the monograph by Malkin (1966)]. It has the well-known peculiar properties typical of the characteristic equation for a Hamiltonian system. According to these properties, in the fourth-degree equation

$$\rho^4 + a_3\rho^3 + a_2\rho^2 + a_1\rho + a_0 = 0,$$
$$a_0 = \det\mathbf{M} = 1, \quad a_1 = a_3 = -\mathrm{Tr}\mathbf{M}, \quad (8)$$

it has the reciprocal (complex conjugate) roots $\rho_1 = 1/\rho_2$ and $\rho_3 = 1/\rho_4$, with $\rho_1 = \rho_2 = 1$, because system (1) is self-similar and because the first integral exists [see, e.g., the monograph by Wintner 1967). The trace of matrix $\mathbf{M}$ (the sum of its diagonal elements) is denoted by $\mathrm{Tr}\mathbf{M}$.

Using the above properties, as well as the relations for multipliers $\rho_j = \exp(\alpha_j T)$ and characteristic indices

$$\alpha_j = \frac{1}{T}\ln\rho_j = \frac{1}{T}\{\ln|\rho_j| + \sqrt{-1}(\arg\rho_j + 2k\pi)\}, \quad (9)$$
$$(j = 1, 2, 3, 4;\ k \text{ is an integer})$$

yields the stability condition for the zero solution of the system of variational Eqs. (5)

$$|\rho_j| = 1 \quad (j = 1, 2, 3, 4) \text{ or } 0 < \mathrm{Tr}\mathbf{M} < 4.$$

The relations given below are used to check the validity of calculations:

$$\det\mathbf{M} = 1, \quad a_2 = 2(\mathrm{Tr}\mathbf{M} - 1),$$

where a_2 is the sum of the principal second-order minors of matrix $\mathbf{M}$.

Thus, investigating the stability of periodic solutions for the problem under consideration reduces to numerical integration of the evolutionary system (1) together with the system of variational Eqs. (5). The initial data for the integration of system (1) can be obtained by independently solving the corresponding boundary-value problems, which ensure that the periodicity conditions for the solution are satisfied; the unit matrix $\mathbf{E}$ is initial for the integration of system (5).

2. ASYMMETRIC PERIODIC SOLUTIONS

We analyze the stability of asymmetric periodic solutions for two-model systems, SU [Sun–Uranus–satellite] and SE [(Sun + Moon)–Earth–satellite], with various parameters N, ε, and γ of the problem and various semimajor axes of satellite orbits. These periodic solutions are generated by steady-state solutions that are stable in the linear approximation

$$(W = W^*;\ \cos i = \cos\Omega = 0;\ \omega = 0, \pi).$$

The dependence of extreme values for the eccentricity of a satellite orbit on integral W serves as a convenient and descriptive characteristic of the family of periodic solutions in our problem, while the dependence of $\mathrm{Tr}\mathbf{M}$ on W characterizes the stability of these solutions. The boundaries of the linear-stability region in four-dimensional phase space of the problem can be approximately determined from the shape of the pro-

jections onto the (ω, *e*) and (Ω, *i*) planes of a periodic solution with a maximum oscillation amplitude, for which the linear stability is still retained.

We chose the values of γ for SU and SE given below from the condition that the two natural periods of small oscillations of a linearized system with constant coefficients were equal, so all four multipliers ρ_j are equal to unity at the equilibrium point.

2.1. SU System

$$N = 1, \quad \varepsilon = 97^\circ.9, \quad \gamma = 1.6557356,$$
$$a = 1\,074\,819 \text{ km}.$$

In Fig. 1, the characteristics of the families found previously (Vashkov'yak and Teslenko 2000) are indicated in the (*W*, *e*) plane by dashed lines. The solutions of these families are unstable even near the equilibrium positions (*W**, *e**), which corresponds to the "hard" loss of stability. The terminology used here is similar to that used by Treshchev (1992). The pair of multipliers $\rho_3 = \rho_4 = 1$ splits into two real values, one of which is smaller than unity and the other is larger than unity. This results in instability, because one of the characteristic indices $\alpha_4 = \ln\rho_4/T$ becomes positive. The multipliers ρ_3 and ρ_4 in the complex plane and their motion as *W* varies are indicated in Figs. 3, 4, and 7 by open circles (recall that, in this case, $\rho_1 = \rho_2 = 1$ are indicated by filled circles).

The solid lines in Fig. 1 smoothly extending the curved dashed lines correspond to new periodic solutions, which proved to be stable in the linear approximation for $W^* \le W < W_1$. This is reflected in Fig. 2, where Tr**M** is plotted against *W*. The value $W = W_1$ corresponds to the bifurcation of solutions. The loss of stability for $W = W_1$ is "soft." The pair of multipliers $\rho_3 = \rho_4 = 1$ for $W > W^*$, which initially splits in two while moving along a unit circumference, reach the points with arguments $\arg\rho_{3,4} \approx \pm 33^\circ$ ($W = W_3$). Then, they return to the original value, and then split into two real values, $\rho_3 < 1$ and $\rho_4 > 1$ (Fig. 4). For $W > W_1$, the periodic solutions are unstable, while the entire family ends with circular orbits confined to the Laplace plane ($W = W_2$, Fig. 1). The instability of such orbits follows from our previous results (Vashkov'yak 1974).

For $W \approx W_1$ (but $W < W_1$), the periodic solution that is stable in the linear approximation is close to the boundary solution. Its projections onto the (ω, *e*) and (Ω, *i*) planes are roughly elliptical in shape. Note that, in the time equal to the evolution period $T \approx 58\,500$ years, the phase point makes one turn in the (Ω, *i*) plane and two turns in the (ω, *e*) plane.

Note. Solutions of this type are not revealed by equations linearized in the vicinity of the equilibrium position. They are also peculiar in that the trajectories in the (ω, *e*) plane do not enclose the stationary point for $W > W^*$. The existence of such solutions follows from an analysis of the corresponding nonlinear problem (Vashkov'yak 1999a). Note the inaccuracy in formula (40) from the above paper. The formula must be of the form $\omega_{12} = -\omega_{34} = \nu$, because $\omega_{34} < 0$. Therefore, the expression for Z_3 and Z_4 in formula (42) must be

$$Z_3 = r_{34}\cos(\nu\tau + \varphi_{34}), \quad Z_4 = -r_{34}\sin(\nu\tau + \varphi_{34}).$$

It follows from an analysis of the solution with $W = W_1$ that, for a given model system and for the assumed semimajor axis, the region of linear stability

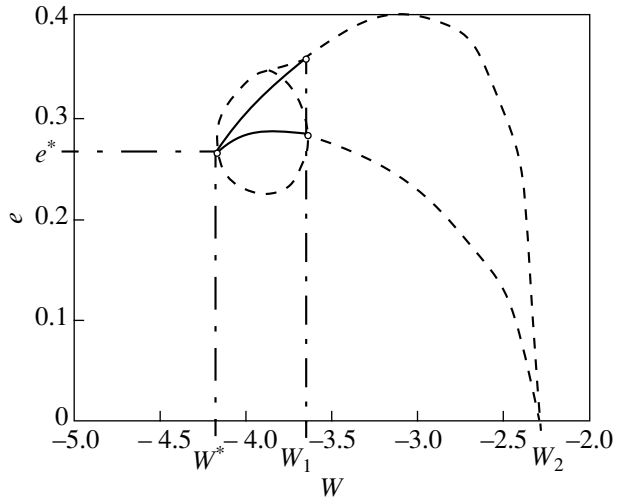

Fig. 1. Characteristics of the families of asymmetric periodic orbits in the *W, e* plane (SU system).

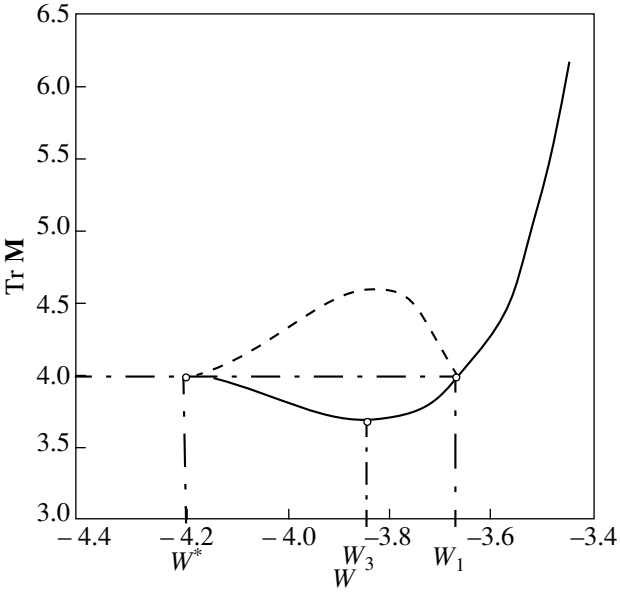

Fig. 2. Trace of the monodromy matrix versus integral of the problem (SU system, asymmetric solutions).

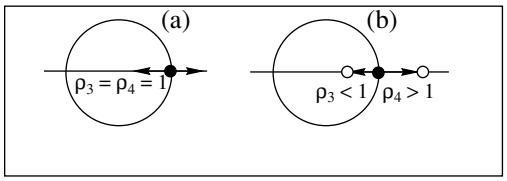

Fig. 3. Motion of the multipliers relative to a unit circumference for the "hard" loss of stability (SU system): (a) $W = W^*$, Tr**M** = 4; (b) $W > W^*$, Tr**M** > 4.

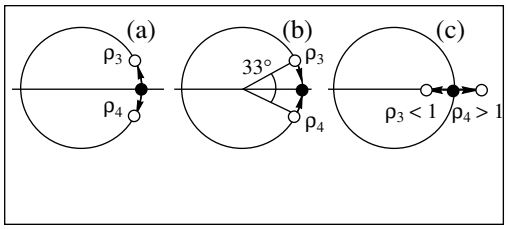

Fig. 4. Motion of the multiplicators relative to a unit circumference for the "soft" loss of stability (SU system): (a) $W \geq W^*$, Tr**M** ≤ 4; (b) $W = W_3 < W_1$, Tr**M** = 3.68; and (c) $W > W_1$, Tr**M** > 4.

of asymmetric periodic solutions can be described by approximate relations

$$0.28 < e < 0.35, \quad 55° < i < 125°, \quad -5.^\circ 5 < \omega < 5.^\circ 5,$$
$$74° < \Omega < 106°, \quad -4.18 \approx W^* \leq W < W_1 \approx -3.65.$$

In order to qualitatively check our calculations, we calculated the evolution of nearly periodic orbits for $W = W_1 - 0.02$ and $W = W_1 + 0.02$. The initial data for periodic solutions were varied by 10^{-3}. Our calculations show that the solution for $W_1 - 0.02$ in the interval $200T$ essentially matches the unvaried (periodic) solution, while for $W_1 + 0.02$, the difference reaches 90° in ω even at $\tau \approx 30T$.

2.2. SE *System*

$$N = 2, \quad \varepsilon = 23.^\circ 44, \quad \gamma = 1.9380817,$$
$$a = 37\,267 \text{ km}.$$

Our calculations allow the sizes of the linear-stability region to be estimated by using the following approximate relations:

$$0.058 < e < 0.168, \quad 82.^\circ 5 < i < 97.^\circ 5, \quad -5° < \omega < 5°,$$
$$70° < \Omega < 110°, \quad -4.58 \approx W^* \leq W < W_1 \approx -4.55.$$

Figures 5–7 are similar to Figs. 1–3, respectively. The loss of stability for $W = W_1$ is "soft." For $W^* < W < W_1$, the pair of values $\rho_3 = \rho_4 = 1$ splits in two while remaining on a unit circumference (Fig. 7). It merges into the pair $\rho_3 = \rho_4 = -1$ for $W = W_1$ and splits into two real values, $-1 < \rho_3 < 0$ and $\rho_4 < -1$, for $W > W_1$. This results in instability, because $|\rho_4| > 1$.

Just as for the SU system, the family of periodic solutions ends at the point ($e = 0$, $W = W_2$) that corresponds to unstable circular orbits confined to the Laplace plane. Check calculations in the interval $\tau \gg T$ were performed both for $W = W_1 - 0.002$ (the solution is stable in the linear approximation) and for $W = W_1 + 0.002$ [the solution is unstable, while $|\omega(\tau)|$ reaches 90° even at $\tau \approx 20T$].

Solutions of this type are peculiar in that the phase point makes one turn in the time equal to the evolution

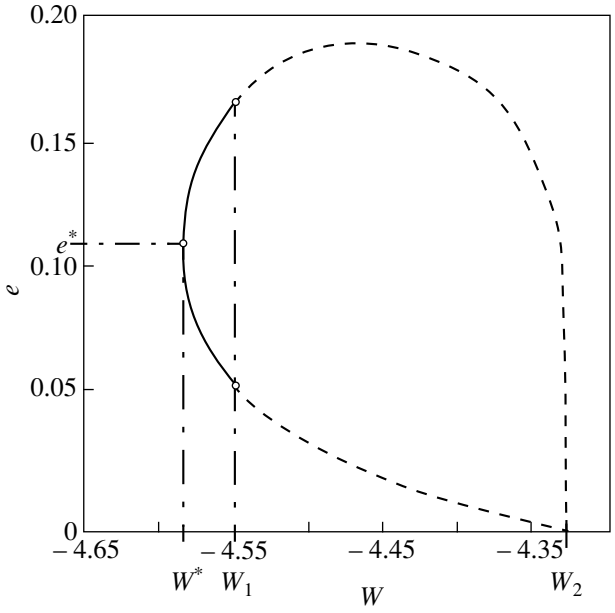

Fig. 5. Characteristics of the families of asymmetric periodic orbits in the *W, e* plane (SE system).

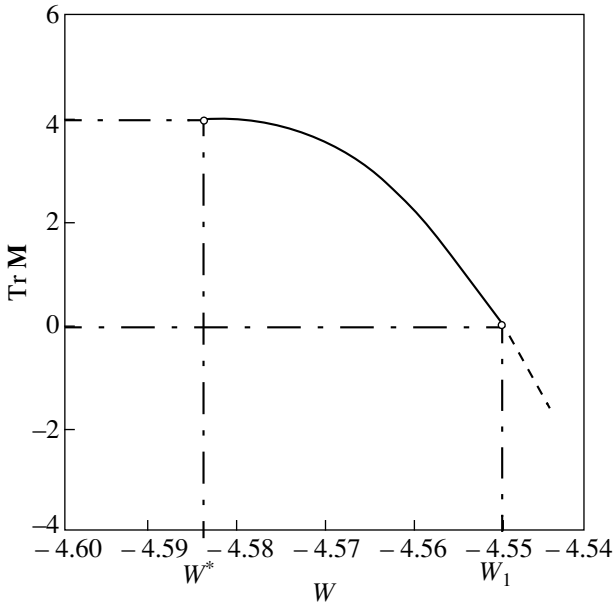

Fig. 6. Trace of the monodromy matrix versus integral of the problem (SE system, asymmetric solutions).

period ($T \approx 243$ years) both in the (ω, e) plane and in the (Ω, i) plane. They were previously obtained (Vashkov'yak and Teslenko 2000) for γ that differed only slightly from that adopted in this section.

3. SYMMETRIC PERIODIC SOLUTIONS

Symmetric periodic solutions are generated by steady-state solutions that are stable in the linear approximation,

$$(W = W^*;\ \Omega = 0;\ \omega = \pm\pi/2).$$

The calculation of monodromy matrix **M** can be simplified by using the well-known property of the evolutionary system (1), according to which the transformation

$$\bar{\tau} = -\tau, \quad \bar{e} = e, \quad \bar{i} = i, \quad \bar{\omega} = -\omega, \quad \bar{\Omega} = -\Omega$$

leaves it invariant. Using this symmetry reduces the calculation of **M** to finding matrix $\mathbf{Z}(T/2)$, with

$$\mathbf{M} = \mathbf{D}\mathbf{Z}^{-1}(T/2)\mathbf{D}\mathbf{Z}(T/2),$$
$$\text{where } \mathbf{D} = \mathbf{diag}(1, 1, -1, -1).$$

The symmetric periodic solutions of the problem under consideration (as well as their generating steady-state solutions) are peculiar in that they exist only at a sufficiently large inclination ε. Below, we therefore consider only the SU model system, but with different (compared to subsection 2.1) parameters γ and a:

$$N = 1,\ \varepsilon = 97^\circ.9,\ \gamma = 0.998989,\ a = 1\,189\,108 \text{ km}.$$

This value of γ was chosen from the 3 : 2 commensurability condition for the two natural periods of small oscillations of a linearized system. Previously (Vashkov'yak 1999b), we constructed three families of periodic solutions I, II, and III with periods $T_1^* \approx 50\,000$ yrs, $T_2^* = 2T_1^*/3 \approx 33\,300$ yrs, and $T_3^* = 2T_1^* = 3T_2^* \approx 100\,000$ yrs, respectively, for the above parameters. In this section, we give the derived dependences of Tr**M** on W, which allow a judgment to be made on the stability of solutions from each of these three families.

The initial points A of these dependences in Figs. 8–10 are determined by $W = W^*$, Tr**M** = 0, 1, 4, and $\rho_1 = \rho_2 = 1$, while the multipliers ρ_3 and ρ_4 (corresponding to periods T_1^*, T_2^*, and T_3^*) are given by the following formulas, in which i is the imaginary unit:

$$\rho_{3,4} = \exp(\pm 2\pi i T_1^*/T_2^*) = \exp(\pm\pi i) = -1,$$

$$\rho_{3,4} = \exp(\pm 2\pi i T_2^*/T_1^*) = \exp(\pm 2\pi i/3) = -\frac{1}{2} \pm \sqrt{3}\frac{i}{2},$$

$$\rho_{3,4} = \exp(\pm 2\pi i T_3^*/T_1^*) = \exp(\pm 2\pi i T_3^*/T_2^*) = \exp(\pm 2\pi i) = 1.$$

The arrows in Figs. 8–10 indicate the direction of motion along the family characteristics from equilibrium position A; their dashed and solid segments correspond to unstable and stable (in the linear approximation) solutions, respectively. In order not to overload this paper with additional figures, we do not show the pattern of motion of the multipliers relative to a unit circumference in the complex plane for these families, as in the case of asymmetric solutions, but give only its verbal description.

3.1. Family I

The stability characteristic of this family (Fig. 8) has a flat initial segment *1*, in which $0 \le \mathrm{Tr}\mathbf{M} \le 0.145$. The loss of stability is "soft." For $W_1 \le W \le W^*$, the multipliers ρ_3 and ρ_4, while splitting, move in opposite directions along a unit circumference from the point $\rho_3 = \rho_4 = -1$; their arguments reach $\theta_3 = 158^\circ$ and $\theta_4 = 202^\circ$, which corresponds to the maximum value of Tr**M** =

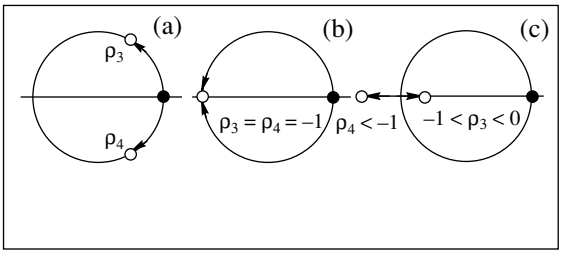

Fig. 7. Motion of the multipliers relative to a unit circumference for the "soft" loss of stability (SE system): (a) $W^* < W < W_1$, $0 < \mathrm{Tr}\mathbf{M} < 4$; (b) $W = W_1$, $\mathrm{Tr}\mathbf{M} = 0$; and (c) $W > W_1$, $\mathrm{Tr}\mathbf{M} < 0$.

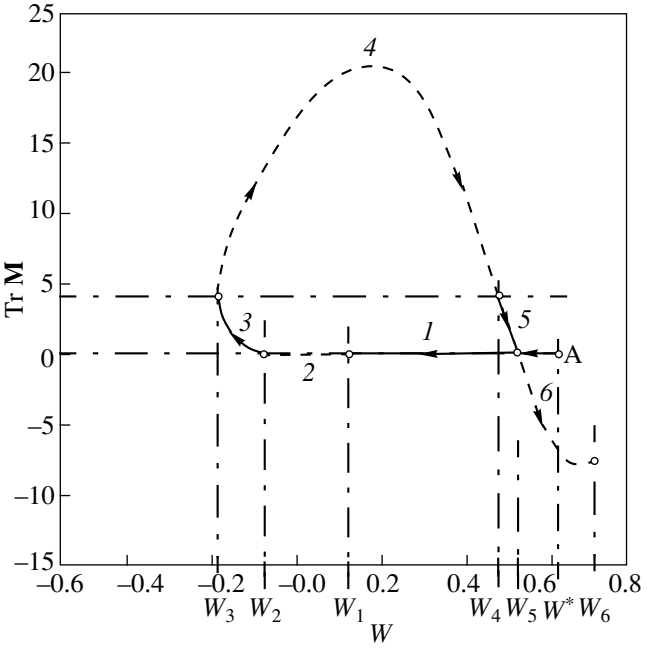

Fig. 8. Trace of the monodromy matrix versus integral of the problem (SU system, symmetric solutions, family I).

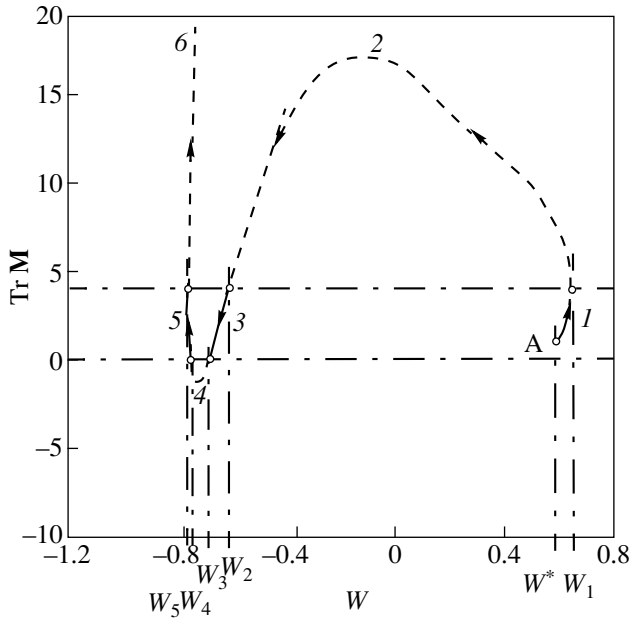

Fig. 9. Trace of the monodromy matrix versus integral of the problem (SU system, symmetric solutions, family II).

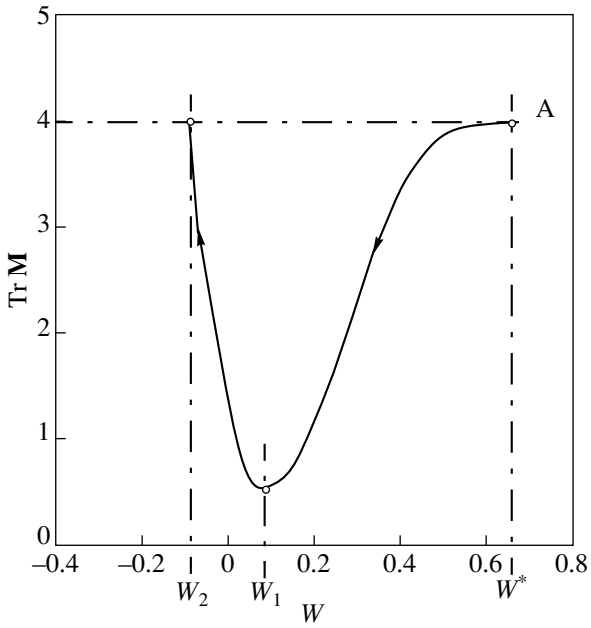

Fig. 10. Trace of the monodromy matrix versus integral of the problem (SU system, symmetric solutions, family III).

0.145. Subsequently, they both return to the original point. The values of θ_3 and θ_4 can be determined from

$$2\cos\theta_{3,4} = \mathrm{Tr}\mathbf{M} - 2,$$

which holds only for $\rho_1 = \rho_2 = 1$ (of course, this formula is also valid for the previously considered asymmetric periodic solutions that are stable in the linear approximation).

For $W_2 < W < W_1$ (segment *2*), the solutions are unstable ($\mathrm{Tr}\mathbf{M} < 0$), while the multipliers ρ_3 and ρ_4 split into two real values, $-1 < \rho_3 < 0$ and $\rho_4 < -1$, which subsequently return to the point $\rho_3 = \rho_4 = -1$ at $W = W_2$.

For $W_3 < W < W_2$ (segment *3*), these multipliers run along a unit circumference to the point $\rho_3 = \rho_4 = 1$ and merge with the stationary multipliers ρ_1 and ρ_2 at $W = W_3$. The solutions are stable in the linear approximation.

The next segment *4* ($W_3 < W < W_4$, $\mathrm{Tr}\mathbf{M} > 4$) corresponds to unstable solutions, when the multipliers ρ_3 and ρ_4 diverge along the real axis and then return to the point $\rho_3 = \rho_4 = 1$ at $W = W_4$.

For $W_4 < W < W_5$ (segment *5*), the solutions are stable in the linear approximation, while the multipliers ρ_3 and ρ_4 traverse the path back along a unit circumference and merge at the point $\rho_3 = \rho_4 = -1$ for $W = W_5$.

Subsequently, they again diverge along the real axis. For $W_5 < W < W_6$ (segment *6*), the solutions are unstable, while the family itself ends with a circular orbit confined to the Lapace plane ($W = W_6$).

The ranges of extreme values for the elements of stable (in the linear approximation) orbits are given in Table 1. We see from this table that these ranges are broadest in segment *1*, smaller in segment *3*, and very narrow in segment *5*.

3.2. Family II

The stability characteristic of this family (Fig. 9) has a solid initial segment *1*, in which $1 \le \mathrm{Tr}\mathbf{M} \le 4$. The loss of stability is "soft." For $W^* \le W \le W_1$, the multipliers ρ_3 and ρ_4 move along a unit circumference from the points with arguments $\theta_{3,4} = \pm 120°$ to the point $\rho_3 = \rho_4 = 1$ ($\mathrm{Tr}\mathbf{M} = 4$, $W = W_1$). Subsequently, they split into two real values ($0 < \rho_3 < 1$, $\rho_4 > 1$). We see from Fig. 9 that, as they move along the characteristic, instability and linear-stability segments are encountered. For $W_2 < W < W_1$ and $\mathrm{Tr}\mathbf{M} > 4$, the solutions are unstable (segment *2*).

After reaching the point $\rho_3 = \rho_4 = 1$ ($W = W_2$, $\mathrm{Tr}\mathbf{M} = 4$), these multipliers, while splitting, move along a unit circumference to the point $\rho_3 = \rho_4 = -1$ ($W = W_3$, $\mathrm{Tr}\mathbf{M} = 0$), and the solutions in the corresponding segment *3* are stable in the linear approximation.

Table 1. Extreme values of the elements for family I orbits

Segment no.	e_{min}	e_{max}	i_{min}, deg	i_{max}, deg	ω_{min}, deg	ω_{max}, deg	Ω_{min}, deg	Ω_{max}, deg
1	0.343–0.383	0.343–0.455	41–71	71–100	85–90	90–95	–20÷0	0–20
3	0.325–0.385	0.535–0.600	30–34	106–110	74–79	100–106	–28÷–25	25–28
5	0.055–0.600	0.515–0.530	47–49	92–94	≈65	≈115	–15÷–13	13–15

Table 2. Extreme values of the elements for family II orbits

Segment no.	e_{min}	e_{max}	i_{min}, deg	i_{max}, deg	ω_{min}, deg	ω_{max}, deg	Ω_{min}, deg	Ω_{max}, deg
1	0.130–0.343	0.343–0.460	≈71	71–74	73–90	90–107	−2.4÷0	0–2.4
3	0.19–0.22	0.72–0.73	20–22	124–126	≈60	≈120	−30÷−36	36–38
5	0.28–0.29	0.75–0.76	≈18	≈126	≈56	≈124	≈−40	≈40

Table 3. Extreme values of the elements for family III orbits

e_{min}	e_{max}	i_{min}, deg	i_{max}, deg	ω_{min}, deg	ω_{max}, deg	Ω_{min}, deg	Ω_{max}, deg
0.343–0.370	0.343–0.545	34–71	71–106	78–90	90–102	−25–0	0–25

Subsequently, the multipliers ρ_3 and ρ_4, having met, split into two real values ($-1 < \rho_3 < 0$, $\rho_4 < -1$), diverge along the real axis, and then again merge at the point $\rho_3 = \rho_4 = -1$ ($W = W_4$, $\mathrm{Tr}\mathbf{M} = 0$). Segment *4* corresponds to unstable solutions.

In segment *5*, the multipliers ρ_3 and ρ_4 traverse a unit circumference in the opposite direction (from the point $\rho_3 = \rho_4 = -1$ to the point $\rho_3 = \rho_4 = 1$) in a narrow range $W_5 \le W \le W_4$, and the solutions are stable in the linear approximation.

Finally, for $W > W_5$ and $\mathrm{Tr}\mathbf{M} > 4$, all the solutions of family II are unstable, and the multipliers split into two real values ($0 < \rho_3 < 1$, $\rho_4 > 1$). This family ends with highly elongated elliptic orbits, when $e_{min} \longrightarrow 1$, $e_{max} \longrightarrow 1$, and the evolution period $T \longrightarrow 0$.

The ranges of elements for the orbits that are stable in the linear approximation are given in Table 2.

3.3. Family III

The stability characteristic of this family consists of one solid segment, $W_2 \le W \le W^*$ (Fig. 10). The multipliers ρ_3 and ρ_4, while splitting, first move along a unit circumference from the point $\rho_3 = \rho_4 = 1$. For $\mathrm{Tr}\mathbf{M} \approx 0.5$ and $W = W_1$, they reach the points with arguments $\theta_{3,4} \approx \pm 138°$ and then return to the original point for $W = W_2$ and $\mathrm{Tr}\mathbf{M} = 4$. Family III of periodic solutions is peculiar in that it "ends" with a solution of family I for $W = W_2$ (see the point $W = W_2$, $\mathrm{Tr}\mathbf{M} = 0$ in Fig. 8). The ranges of elements for the orbits corresponding to this family are given in Table 3.

4. CONCLUSION

This article completes our series of papers on the steady-state and periodic solutions for Hill's averaged problem with allowance for planetary oblateness. The orbits, whose elements are either invariable or vary with the same period under the combined effect of secular perturbations from planetary oblateness and from a distant attracting point, correspond to these solutions. Such steady-state and periodically evolving satellite orbits in circumplanetary regions, where the effects of the above two factors are approximately the same, can be unstable and stable (at least in the linear approximation). Our estimates of the linear-stability regions for periodic solutions, both symmetric (Tables 1–3) and asymmetric (Subsections 2.1, 2.2), show that the ranges of extreme values for the elements of periodically evolving orbits that are stable in the linear approximation are relatively narrow. The orbits of the natural satellites around the giant planets discovered to date "avoid" the peculiar regions of approximately equal influence, and their evolution is mainly determined either by planetary oblateness (for close satellites) or by solar attraction (for distant satellites). This circumstance, in particular, for Uranus's system of satellites, can apparently be associated with a small "margin of linear stability" of the steady-state and periodically evolving orbits constructed in terms of Hill's averaged problem with allowance for planetary oblateness. It is therefore of interest to consider model problems that take into account additional perturbing factors, which can qualitatively change the pattern of evolution. Such factors can primarily include the inclination of the ecliptic, the orbital ellipticity of a perturbing point, and the parallactic terms of the force function of its attraction.

ACKNOWLEDGMENTS

This work was supported by the Council of Grants of the President of Russia and the State Support for Leading Scientific Schools (grant no. 00-15-96036).

REFERENCES

1. V. Kudielka, Celest. Mech. Dyn. Astron. **60**, 455 (1994).
2. M. L. Lidov and M. V. Yarskaya, Kosm. Issled. **12**, 155 (1974).
3. I. G. Malkin, *Theory of the Stability of Motion* (Nauka, Moscow, 1966).
4. D. V. Treshchev, Prikl. Mat. Mekh. **56**, 587 (1992).
5. M. A. Vashkov'yak, Kosm. Issled. **12**, 834 (1974).
6. M. A. Vashkov'yak, Pis'ma Astron. Zh. **25**, 631 (1999a) [Astron. Lett. **25**, 544 (1999)].
7. M. A. Vashkov'yak, Pis'ma Astron. Zh. **25**, 792 (1999b) [Astron. Lett. **25**, 688 (1999)].
8. M. A. Vashkov'yak and N. M. Teslenko, Pis'ma Astron. Zh. **26**, 394 (2000) [Astron. Lett. **26**, 331 (2000)].
9. A. Wintner, *Analytical Foundations of Celestial Mechanics* (Princeton Univ. Press, Princeton, 1941; Nauka, Moscow, 1967).

Translated by V. Astakhov